

2015-01-01

Modeling and Preliminary Characterization of Passive, Wireless Temperature Sensors for Harsh Environment Applications Based on Periodic Structures

Diego Ivan Delfin Manriquez

University of Texas at El Paso, ddelfin2@miners.utep.edu

Follow this and additional works at: https://digitalcommons.utep.edu/open_etd



Part of the [Electromagnetics and Photonics Commons](#), and the [Mechanical Engineering Commons](#)

Recommended Citation

Delfin Manriquez, Diego Ivan, "Modeling and Preliminary Characterization of Passive, Wireless Temperature Sensors for Harsh Environment Applications Based on Periodic Structures" (2015). *Open Access Theses & Dissertations*. 1029.
https://digitalcommons.utep.edu/open_etd/1029

This is brought to you for free and open access by DigitalCommons@UTEP. It has been accepted for inclusion in Open Access Theses & Dissertations by an authorized administrator of DigitalCommons@UTEP. For more information, please contact lweber@utep.edu.

MODELING AND PRELIMINARY CHARACTERIZATION OF PASSIVE,
WIRELESS TEMPERATURE SENSORS FOR HARSH ENVIRONMENT
APPLICATIONS BASED ON PERIODIC STRUCTURES

DIEGO I. DELFIN MANRIQUEZ

Department of Mechanical Engineering

APPROVED:

Yirong Lin, Ph.D., Chair

Raymond C. Rumpf, Ph.D., Co-chair

Calvin M. Stewart, Ph.D.

Charles Ambler, Ph.D.
Dean of the Graduate School

Copyright ©

by

Diego I. Delfin Manriquez

2015

Dedication

To my parents, Orlando y Alma; my brothers, Orlando Jr., Mauricio and Luis, and my girlfriend Alia.

Para mis padres, Orlando y Alma; mis hermanos, Orlando Jr., Mauricio y Luis, y mi novia Alia.

MODELING AND PRELIMINARY CHARACTERIZATION OF PASSIVE,
WIRELESS TEMPERATURE SENSORS FOR HARSH ENVIRONMENT
APPLICATIONS BASED ON PERIODIC STRUCTURES

by

DIEGO I. DELFIN MANRIQUEZ, B.S.M.E.

THESIS

Presented to the Faculty of the Graduate School of

The University of Texas at El Paso

in Partial Fulfillment

of the Requirements

for the Degree of

MASTER OF SCIENCE

Department of Mechanical Engineering

THE UNIVERSITY OF TEXAS AT EL PASO

December 2015

Acknowledgements

First and foremost, I would like to thank Dr. Yirong Lin for all of his constant motivation and support, advice, patience, and teaching in research and other aspects of my professional development. I really appreciate the opportunity to conduct research under your supervision and participate in such interesting and challenging projects. Specially, I would like to thank you for trusting me with this research project. I would also like to thank Dr. Raymond Rumpf for helping us develop this research project and giving us very helpful advice on its critical stages. I am grateful that your door was always open and you never hesitated to offer us help. I would also like to thank Dr. Calvin Stewart for serving as a committee member in my thesis defense.

I would like to express my sincerest gratitude to the Department of Energy for funding the initial stages of this project, also to The University of Texas at El Paso and the Department of Mechanical Engineering for allowing us to use their facilities to conduct this research. I would also like to thank all of my lab-mates in Dr. Lin's group. I would like to give special thanks to Hasanul Karim, Luis Chavez, and Jose Romero for their continuous encouragement and support, as well as for all of their effort and contributions to this project. Additionally, I would like to thank my co-workers and friends Luis Varela, Alejandra Cabral, Luz Bugarin, Sergio Guerrero, Ricardo Martinez, Gerardo Rodriguez, Armando Delgado and Alan Esparza for their advice and support. Moreover, I would like to thank Jose Avila and Carlos Rodriguez from the EM Laboratory for all of their help with the testing stages of this project.

Last but not least, I want to specially thank my family, with special mention to my parents, brothers, my relatives Teresita and Martin, and my cousins Andres, Jose, Sergio, Luisa, Marisol, and my girlfriend, Alia, who have always been there for me during this process and have helped succeed through their love and care. The work presented in this thesis is due in great part to your patience, advice and strength, providing me with the most robust pillars to stand on and go on with my graduate studies.

Abstract

Wireless temperature sensing has attained significant attention in recent years due to the increasing need to develop reliable and affordable sensing solutions for energy conversion systems and other harsh environment applications. The development of next generation sensors for energy production processing parameters, such as temperature and pressure, can result in better performance of the system. Particularly, continuous temperature monitoring in energy conversion systems can result in enhancements such as better system integrity, less pollution and higher thermal efficiencies. However, the conditions experienced in these system components hinder the performance of current solutions due to the presence of semi-conductor materials and welded joints. Additionally, the use of wired systems can result in complex wiring networks, increasing the cost of installation, maintenance and sensor replacement. Therefore, next generation sensing solutions must be developed to overcome current challenges in systems where adverse conditions are present. This research project proposes two novel passive, wireless temperature sensor designs based on concepts of guided mode resonance filters (GMRF) and metamaterials. For the GMRF, a tri-layer structure using a metallic encasing and a circular aperture grating layer was developed to have a resonance frequency of 10 GHz. While for the metamaterial-based sensor a continuation of previous work was presented by utilizing a dielectric substrate and an array of commercially available metallic washers divided in two layers. For both designs, High Frequency Structure Simulator (HFSS) from ANSYS® was employed to assess the feasibility of the sensor as well as to optimize the geometry and guide the fabrication process. A systematic approach consisting of evaluating the unit cell, then assessing the number of periods needed, and finally characterizing the response of the final sensor was followed for each case. After the modeling process was completed, the optimal configuration for the GMRF sensor was found to be the with an alumina slab with a thickness of 1.524 mm, two titanium screens with a thickness of 0.508, the use of metallic side reflectors and a side length of 49.525 mm. For the metamaterial, the process aforementioned resulted in a sensor design

composed of a BTO/BN ceramic substrate and copper washers with 3.5 mm in OD and 1.6 mm in ID; the sensor side length was of 101.7 mm and design thickness was chosen to be 3.175 mm. The performed simulations resulted in several peaks in a 6 – 18 GHz frequency range for both the reflection and transmission spectra. The limitation of the periodicity had a detrimental effect on the response of the sensor; however, a final sensor design was achieved with visible response in both the reflection and transmission regions. Fabrication was carried over using water-jet cutting and traditional machining methods for the GMR sensor, while a traditional powder compression method was employed for the metamaterial sensor. For the former, titanium screens were used, while aluminum and steel plates were employed on the second one. Commercially available alumina ceramic was employed for both fabrication methods. As for the metamaterial sensor, the fabrication was done by utilizing a mixture of 70% boron nitride/30% barium titanate with an added 7.5% wt. PVA for structural rigidity. Final dimensions of 50.8 mm in side length and a thickness of 3.175 mm were achieved. Samples fabricated showed good structural integrity and manageability. Preliminary free space measurements were performed using a Programmable Network Analyzer (PNA) and a set of X-band horn antennas and Gaussian beam antennas to characterize the response of both the GMR and the metamaterial sensors, respectively. No visible peak was observed for the GMR sensor in the frequency region. The lack of response might be attributed to fabrication errors. For the metamaterial sensor, a strong response at 14.47 GHz mark with an intensity of -33.05 dB was observed. The response found could be employed for temperature measurements. Finally, suggestions for future work are given to overcome the challenges present in current sensor designs and fabrication processes.

Table of Contents

Acknowledgements	v
Abstract	vi
Table of Contents	viii
List of Tables	x
List of Figures	xi
Chapter 1: Introduction	1
Chapter 2: Background and Literature Review	2
2.1 Introduction	2
2.2 Introduction to frequency selective surfaces	2
2.3 Diffraction gratings	6
2.4 Slab waveguides	8
2.5 Guided mode resonance filters	10
2.6 Introduction to metamaterials	13
2.7 Recent development of guided mode resonance filters	20
2.8 Recent development of metamaterials	22
2.9 Wireless temperature sensors	24
2.10 Conclusion	26
Chapter 3: Finite Element Modeling and Simulation	28
3.1 Introduction	28
3.2 Guided mode resonance filter sensor	28
3.2.1 Concept and design	28
3.2.2 Unit cell simulation and geometry optimization	31
3.2.3 Effect of the radius of the circular aperture	36
3.2.4 Temperature influence on the response of the sensor	38
3.2.5 1-D periodicity simulations	40
3.2.6 Full sensor simulation	46
3.3 Metamaterial-based sensor	48
3.3.1 Concept and design	48

3.3.2 Dielectric material evaluation and selection	50
3.3.3 Unit cell simulation	51
3.3.4 1-D periodicity simulations.....	53
3.3.5 Finite block simulation	55
3.3.6 4-block simulation	57
3.4 Conclusion	59
Chapter 4: Fabrication.....	61
4.1 Introduction	61
4.2 Guided mode resonance sensor	61
4.2.1 Water jet cutting based samples	61
4.2.2 Traditional machining based samples	63
4.3 Metamaterial sensor fabrication.....	65
4.3.1 Binder synthesis	65
4.3.2 Traditional powder compression method.....	66
4.4 Conclusion	68
Chapter 5: Testing and Results	69
5.1 Introduction	69
5.2 Free space measurements of guided mode resonance filter sensor.....	69
5.3 Free space measurements of metamaterial sensor	73
5.4 Conclusion	75
Chapter 6: Conclusions and Future Work.....	77
6.1 Conclusions	77
6.2 Recommendations for future work	79
6.2.1 Guided mode resonance filter sensor	79
6.2.2 Metamaterial sensor	80
References	81
Appendix A: GMRF finite sensor simulation with cladding layer separation.....	88
Vita.....	90

List of Tables

Table 3.1. Temperature dependent dielectric constant of 99.5% alumina at 10 GHz [99]	39
--------------------------------------------------------------------------------------------	----

List of Figures

Figure 2.1. Frequency selective surface geometries utilizing (A) positive (slot array) and (B) negative (dipole array) space for the metal structure	3
Figure 2.2. Typical radome structure for antenna protection (Courtesy of Deh-Ron LTD.).....	4
Figure 2.3. Example of Cassegrain antenna with a periodic dipole structure on the reflector (Courtesy of Wikimedia Commons)	5
Figure 2.4. F-117 stealth fighter, FSSs are used on the surface to make it undetectable to radars (Courtesy of Wikipedia)	6
Figure 2.5. (A) Trimetric view of simple diffraction grating, (B) Side view portraying spatial modulation of refractive index	7
Figure 2.6. Schematic of (A) a hollow tube waveguide and (B) slab-waveguide with different dielectric materials	9
Figure 2.7. (A) Depiction of an incident wave illuminating a diffraction gratings and the resulting reflecting and transmitting discrete modes, (B) Wave guiding of a supported diffracted mode ..	11
Figure 2.8. Examples of meta-atoms developed in literature thus far [40 – 42].....	15
Figure 2.9. Examples of developed metamaterials structures, (A) Structure with capacitively loaded rings for MRI [43] (B) Split ring resonator structure for negative refractive index applications [44].....	15
Figure 2.10. Representation of refractive indices for right-handed and left-handed materials ...	19
Figure 2.11. (A) 2D ray tracing around a material using a cloaking device, (B) 3-D representation of same phenomenon [52].....	20
Figure 2.12. Ekmkeci et al. proposed unit cell for multi-functional sensors [97]	26
Figure 3.1. (A) Side view of the proposed sensor, (B) Top view displaying the metallic grating	29
Figure 3.2. Representation of initial unit cell model	32
Figure 3.3. Example of unit cell scaling (4.48 mm → 9.934 mm).....	33
Figure 3.4. Comparison of the resonance frequency provided by side lengths utilized	33
Figure 3.5. Summary of the dimensions of the GMRF sensor unit cell	35
Figure 3.6. Trimetric view of the final model for the sensor's unit cell	35
Figure 3.7. Reflection results for optimized unit cell simulation	36
Figure 3.8. Reflection results for a varying circular aperture radius	37
Figure 3.9. Relative permittivity values for 99.5% alumina at different frequencies [99]	38
Figure 3.10. Temperature variation results for GMRF sensor.....	40
Figure 3.11. Developed models for (A) 5, (B) 10 and (C) 15 periods.....	42
Figure 3.12. Reflection spectra comparison between the 5, 10 and 15 period models.....	43
Figure 3.13. 1-D periodicity simulation with reflectors on finite ends.....	44
Figure 3.14. Reflection spectra for 1-D periodicity with reflectors.....	45
Figure 3.15. GMRF sensor model for finite simulation, additional boxes around main air-box represent the PML boundary conditions	46
Figure 3.16. Reflection response of finite GMRF sensor, showing the traceable resonance peak around the 10.2 GHz mark.....	48
Figure 3.17. (A) Model of proposed sensor and (B) equivalent circuit model	49
Figure 3.18. Unit cell of metamaterial sensor	52
Figure 3.19. (A) Reflection and (B) transmission results for the evaluated metamaterial sensor	53
Figure 3.20. 1-D model of the metamaterial temperature sensor	54

Figure 3.21. (A) Reflection and (B) transmission results for 1-D periodicity model of metamaterial sensor	55
Figure 3.22. Model for sensor block employing 25 pairs of CRRs	56
Figure 3.23. (A) Reflection and (B) transmission response of finite block sensor.....	57
Figure 3.24. Model of 4-block metamaterial sensor showing the PML boundary conditions.....	58
Figure 3.25. (A) Reflection and (B) transmission spectra of the designed 4-block metamaterial sensor	59
Figure 4.1. Fabricated samples, from left to right: first and second ones are bonded with alumina paste and third one is bonded using Superglue	62
Figure 4.2. Water jet cutting based samples bonded with (A) alumina paste and (B) Superglue	63
Figure 4.3. Sample fabricated through traditional machining methods displaying (A) different components and (B) assembled sensor	65
Figure 4.4. Experimental procedure for PVA binder synthesis	66
Figure 4.5. Schematic for metamaterial sensor fabrication	67
Figure 4.6. (A) Top view and (B) side view of an array of 2x2 metamaterial samples.....	67
Figure 5.1. Close-up of free space measurements for (A) aluminum and (B) steel samples; additionally the (C) and (D) images represent the side view and front view of the testing setup	70
Figure 5.2. Reflection results for the aluminum (red) and steel (blue) GMRF sensors; (A) and (B) represent test 1 and (C) and (D) display test 2.....	71
Figure 5.3. Close-up view on the top layer separation of the (A) aluminum and (B) steel samples	72
Figure 5.4. Free space testing setup consisting of Gaussian beam antennas and Styrofoam container for transmission measurements of metamaterial sensors.....	73
Figure 5.5. Transmission response for 4-block arrangement in the using Gaussian beam antennas	75
Figure A.1. (A) Trimetric view of finite sensor model with air-gap, (B) side view portraying the air-gap	88
Figure A.2. Reflection spectra of finite model with the included air gap.....	89

Chapter 1: Introduction

Continuous advancement in energy conversion systems such as gas turbines, coal based power plants and, in recent years, alternatives such as oxy-fuel combustion and co-fired power plants has sparked an increasing interest in the development of sensing technologies for processing parameters. Among these parameters, continuous temperature monitoring is of utter importance in order to achieve better combustion profiles, resulting in higher thermal efficiencies and a decrease in pollutant agents released to the atmosphere. Additionally, precise temperature control is necessary for successful feedback control in order to achieve system optimizations and to ensure the structural integrity of the components of thermodynamic systems [1]. However, these systems commonly operate in the presence of adverse conditions, such as high temperature, high pressure, corrosive atmospheres and electromagnetic interference [2, 3]. These conditions have rendered current solutions unreliable due to the presence of semi-conductor materials, energy storage devices and welded joints in their configurations [4-6]. Furthermore, the use of wired connections for contemporary solutions leads to higher costs of implementation and maintenance and increased system complexity, which promotes the operating failure of present temperature sensors. This has emphasized the need for robust passive, wireless temperature sensing solutions that maintain reliable operation and accurate temperature readings while operating in harsh environment applications. Among the possible technologies, periodic structures composed of a ceramic substrate coupled with metallic geometries, such as guided mode resonance filters (GMRFs) and metamaterials, have attained significant attention in recent years due to their unique properties and potential for sensing solutions. This research aims to develop passive, wireless temperature sensors based on metamaterials and GMR filters capable of providing consistent operation in harsh environment applications.

Chapter 2: Background and Literature Review

2.1 Introduction

This chapter discusses the definition and background of the technologies that enable this research project as well as the recent developments of relevant areas. An extensive introduction to frequency selective surfaces and guided mode resonance filters is given. For the frequency selective surface section, a definition, general overview of the working mechanism and current and possible applications are discussed. After that, the individual components of guided mode resonance filters are discussed for informational purposes. Moreover, a description and an overview of the working mechanism of guided mode resonance filters are given. Metamaterials, the second alternative for the development of passive, wireless temperature sensors is also discussed in this chapter. A definition for this type of devices will be given as well as an overview of the historical development and the working mechanism. Finally, the last three subsections focus on recent development of guided mode resonance filters, metamaterials and wireless temperature sensors, respectively.

2.2 Introduction to frequency selective surfaces

Frequency selective surfaces (FSSs), also known as dichroic structures, consist of single or multilayered periodic geometrical arrays of elements capable of filtering specific frequencies from incident electromagnetic waves [7]. FSSs have seen extensive research and development as spatial filters due to their design-derived selection and allowance of selected frequency bands, resulting in innovations in areas such as stealth technologies, optics and communications. Traditionally, a frequency selective surface is composed of the coupling of a metal screen/plate with a periodic pattern to a dielectric material. Additionally, the periodicity can be comprised in either the positive or negative space, such as apertures or patches, respectively, as observed in Figure 2.1 (A) and (B).

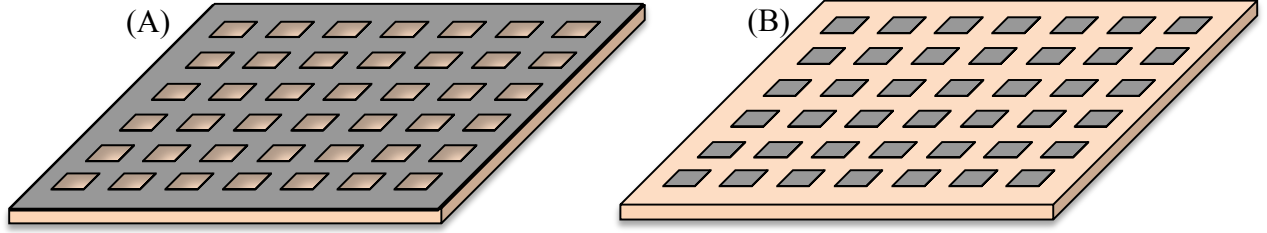


Figure 2.1. Frequency selective surface geometries utilizing (A) positive (slot array) and (B) negative (dipole array) space for the metal structure

The response occurs upon the interaction of the incident electromagnetic wave with the periodic array. A resonant frequency is observed when the effective length is a multiple of the resonance length $\lambda/2$ [8]. This resonance behavior occurs when an incident plane wave interacts with the FSS. In the dipole array, an electric current is induced by exciting the individual elements and an electric field is radiated back, while for the slot array, a magnetic field is initiated by the appearance of magnetic currents [9]. These radiating fields interfere with the incoming wave creating the resonance behavior of the structure [9]. However, being a periodic structure, the number of periods of the repeating unit cell plays a role in the performance of FSSs; ideally, an infinite number of periods would be required for a 100% efficiency. Moreover, the incidence angle of the incoming plane-wave plays a role in the response of the FSS, allowing for the resonance to exist only in specific view angles and resulting on different performance when illuminated from different perspectives. As mentioned before, the main application of FSSs is to serve as a filter for specific frequency bands, allowing for desired frequencies to transmit or reflect while inhibiting the rest from such behavior. This can separate the data carrying frequency of the system from surrounding noise and undesirable interference that could hinder the quality of the signals. This has direct application on antenna design and communications. Furthermore, this has been applied to stealth technologies, preventing incoming spatial waves from returning to the receiver, hiding an object from radar systems. For the former, FSSs can be applied to radome structures. A radome protects an antenna from its physical environment, such as environmental and aerodynamic conditions [10]. For proper functioning, a radome should be transparent to the transmitting and received electromagnetic

waves to prevent performance degradation of the enclosed antenna [11]. An example of a radome can be observed in Figure 2.2.



Figure 2.2. Typical radome structure for antenna protection (Courtesy of Deh-Ron LTD.)

FSSs can also be designed to enhance antenna systems. Reflectors and subreflectors can be designed using frequency selective surfaces serving as wavelength filters for the feed or receiver antenna. Applying FSSs to these antenna components can reduce interference in communication systems since these surfaces can behave as a reflector or a transparent material depending on the incoming frequency [12]. Hence, preventing undesired frequencies from being transmitted or received by the system. For instance, this type of behavior can be beneficial for Cassegrain antennas, where the feeder sends the electromagnetic wave onto a secondary reflector, which sends it to the main reflector in order to form the desired beam. This antenna design is portrayed in Figure 2.3.



Figure 2.3. Example of Cassegrain antenna with a periodic dipole structure on the reflector (Courtesy of Wikimedia Commons)

In stealth technologies, FSSs can also be applied to structures such as aircraft fuselage with the main objective of making them invisible to radar detection systems. Radars rely on sending radio waves through space and capturing the reflected spectrum from nearby objects present on the electromagnetic radiation travelling path. Their effectiveness is based on how much of the reflected electromagnetic energy is received by the radar [13]. The inclusion of FSSs on the outermost surface of the desired structure can absorb the wave illuminating it at a desired frequency and thus, preventing from returning to the source, making the objective effectively undetectable.



Figure 2.4. F-117 stealth fighter, FSSs are used on the surface to make it undetectable to radars (Courtesy of Wikipedia)

As previously stated, frequency selective surfaces can be designed to be composed of a single layer of material or a multilayered structure. For the latter, several combinations of metal-dielectric or pure dielectric structures can be engineered to satisfy application requirements. However, when a tri-layered structure consisting of metal-dielectric-metal or all-dielectric structures with different refractive indices is built, a guided mode resonance filter (GMRF) is achieved. The physical phenomenon present in this type of device is possible due to the electromagnetic coupling of a diffraction grating (top layer) and a slab waveguide, which is composed by the combination of the three layers aforementioned. A description of the individual elements of a guided mode resonance filter as well as the comprehensive introduction to guided mode resonance filters is presented in the following sections.

2.3 Diffraction gratings

A diffraction grating consists of a group of transmitting or reflecting elements separated by a distance similar to the working wavelength [14]. Diffraction gratings can consist of a dielectric substrate with periodic structures in the form of apertures or extrusions, yielding a

spatial modulation, allowing it to interact uniquely with an illuminating light beam. The spatial modulation allows for the separation of polychromatic light into discrete modes. The modulation of space aforementioned can be of the dielectric permittivity, hence altering the grating's refractive index, or conductivity of the material [15]. Diffraction gratings caused an important impact in the area of spectroscopy and effectively affected several disciplines such as astrophysics, quantum physics, chemistry and telecommunications, among others. An example of a diffraction grating is presented in Figure 2.5.

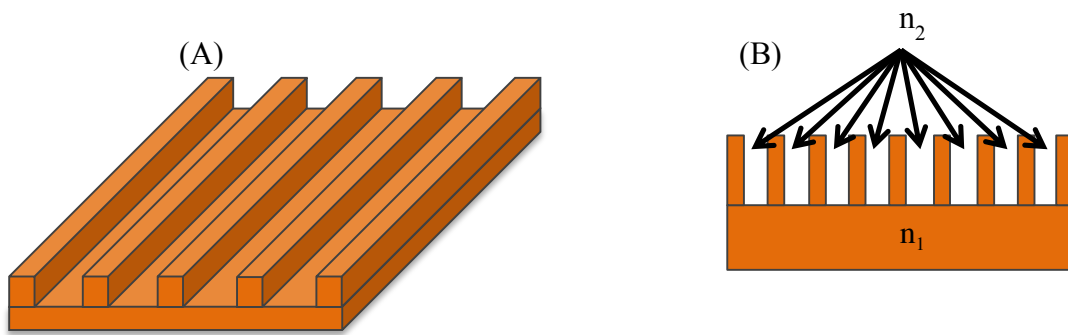


Figure 2.5. (A) Trimetric view of simple diffraction grating, (B) Side view portraying spatial modulation of refractive index

Light diffraction occurs when a wave encounters an obstacle or a slit with a size comparable to its wavelength. The presence of the obstacle will affect the spreading behavior of the wave around the obstacle or through the slit. These phenomena can occur in nature by imposing an adequate object in the traveling path of the wave front. The first consideration of a naturally occurring diffraction grating is credited to James Gregory [16]. In 1673, Gregory utilized a feather to obstruct a small light opening and observed several ovals differently colored, while the center one remaining white [16]. Furthermore, the first record of the use and measured results of a man-made diffraction grating is attributed to Rittenhouse in 1786. Rittenhouse devised an object consisting of a square of parallel hairs each threaded to fine screws half an inch away, which, when placed parallel to a window slit in a dark room, resulted in the separation of light into individual rays of varying brightness [17]. The development of diffraction gratings continued in the upcoming years, leaded by Joseph van Fraunhofer. Fraunhofer developed a

ruling engine, investigated the properties of diffraction gratings in depth and derive the governing equations while developing gratings with an element separation of 12 mm [18]. The scientific applications of diffraction gratings surged when Lord Rayleigh theoretically demonstrated their superiority to prisms in high-resolution spectroscopy considering that high tolerances are achieved [18]. Finally, the modern era of this optical device emerges with Rowland, which in 1882, built a superior ruler engine and was able to fabricate diffraction gratings with up to 29,000 lines per inch [19]. With the historical development aforementioned, gratings allowed for continuous development in optical instrumentation, specially benefiting the area of spectroscopy and, subsequently, its applications.

The light separation and filtering properties of diffraction gratings have allowed them to attain significant popularity in a wide range of applications. Among these applications, the inclusion of gratings is notable in spectrometers, monochromators and spectrographs; where these instruments employ gratings to divide the light spectrum based on the wavelength [20]. The use of gratings in spectroscopy has allowed for test different scales such as blood sample analysis, industrial quality control, atomic research and star composition characterization [20]. In a similar manner, gratings are used in laser technologies and in filtering applications. For instance, in fiber optics, gratings have been used as band rejecting filters [21]. Moreover, in laser technologies; they have been used for laser profile shapers [22]. A description is provided next for the second component of guided mode resonance filters, the slab waveguide.

2.4 Slab waveguides

A waveguide, in simple and traditional terms, consists of a hollow metal tube capable of transporting electromagnetic energy from one place to another without significant attenuation of the wave [23]. In the interior of the tube, air or a dielectric material with minimal loss is placed in order for the electromagnetic radiation to travel through it [23]. This tube is typically of circular or rectangular cross-section. Aside from metal-bound wave guiding devices, all-dielectric waveguides have surged as alternatives for applications where the use or effectiveness

of metallic materials might be limited. For instance, all-dielectric waveguides need to be used in the optical frequency range, due to the significant absorption losses in metal components [24]. Both metallic and all-dielectric waveguides rely on total internal reflections to transport electromagnetic radiation; however, this phenomenon is achieved differently for each case. In the former, this is achieved by the reflectance of the metal; in the latter, it derives from the refractive index of the material and the critical angle of incidence of the incoming wave. Figure 2.6 displays examples of both metallic and all-dielectric waveguide structures.

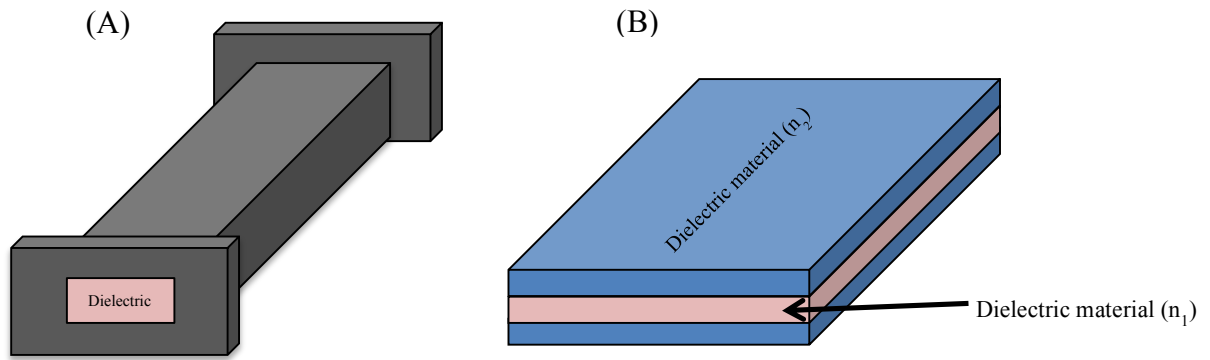


Figure 2.6. Schematic of (A) a hollow tube waveguide and (B) slab-waveguide with different dielectric materials

The development of waveguides began with the mathematical proof of wave propagation of electromagnetic energy in hollow square and circular cross sections in 1897 by Lord Rayleigh [25]. In 1902, Weber suggested that the velocity of the wave in these hollow tubes is less than that of light in the medium; he proposed that the wave travels as a plane wave bouncing off the walls of the conductor in a zigzag pattern [26]. After this, the study of waveguides reignited in 1936, when two researchers, Southworth and Barrow, independently published papers on the waveguide and the cylindrical waveguide, respectively [27]. After these events, waveguide development continued with the invention of the planar transmission strip [28] and the microstrip lines [29]. Based on this development, waveguides have been applied in different areas such as RF engineering, integrated circuits and energy transport in radars and antennas.

In radar and antenna applications, waveguides are used to transport the electromagnetic radiation from the source to the antenna. Particularly, waveguides have aided in the development of devices such as integrated front lines for radar antenna subsystems working on the millimeter wave spectra [30]. Additionally in laser technologies, waveguide lasers utilize this optical device to guide the traveling radiation in order to deviate from the free space propagation laws [31]. Finally, microstrips can be used to form antennas, couplers and similar devices in microwave frequencies. The guiding properties of waveguides have made them one of the most popular devices in electronics and an integral part of the working mechanism of guided mode resonance filters, for which an overview is provided in the next section.

2.5 Guided mode resonance filters

A guided mode resonance filter (GMRF) is a multilayered optical device that is obtained when the aforementioned geometrical array, otherwise known as diffraction grating, is brought to close proximity and, hence, electromagnetically coupled to a slab waveguide [32]. The coupling allows for the exchange of energy between the incident wave and the discrete modes developed from the diffracted wave. GMRF take advantage of the physical phenomena occurring from the interaction between the illuminating electromagnetic radiation and both the diffraction grating and slab waveguide. Due to their filtering properties, GMRFs applications overlap with those of frequency selective surfaces mentioned at the beginning of this chapter. Particularly, the use of guided mode resonance filters can result in better line narrowing of lasers, sensing devices with high precision and better thin film structures if 100% narrowband reflectivity is achieved [33].

The interaction of incoming electromagnetic waves of selected wavelengths and a GMRF can be described by focusing on the effect of its individual elements. When an incident plane wave illuminates the diffraction grating part of a GMRF, the grating will decompose the wave into discrete modes in both the transmission and reflection spectra due to its spatial modulation; a phase shift will accompany this discretization. This is possible due to the presence of Wood's

anomalies. The two types of Wood's anomalies are the Rayleigh type, also known as the classical Wood's anomaly, which is the appearance of a spectral mode propagating along the surface and the less common resonance type [33]. The resonance type Wood's anomaly refers to the existence of possible guided modes that could be supported if a waveguide grating was present sans modulation [33]. Subsequently, based on the resonance type anomaly and the presence of a coupled waveguide, the supported modes will propagate through the waveguide while the rest become evanescent fields. A resonance phenomenon occurs when phase is matched between the diffracted modes and the waveguide modes [34]. Due to the leaky structure of the device [35], the supported mode will escape the waveguide from the same spaces from which it entered, re-diffracted and with a specific phase, destructively interfering with the incoming wave and creating a resonance behavior [36]. This resonant behavior is limited to specific wavelengths and orientation of the incident plane wave [36]. The graphical description of the working mechanism of guided mode resonance filters is shown in Figure 2.7(A) and 2.7(B).

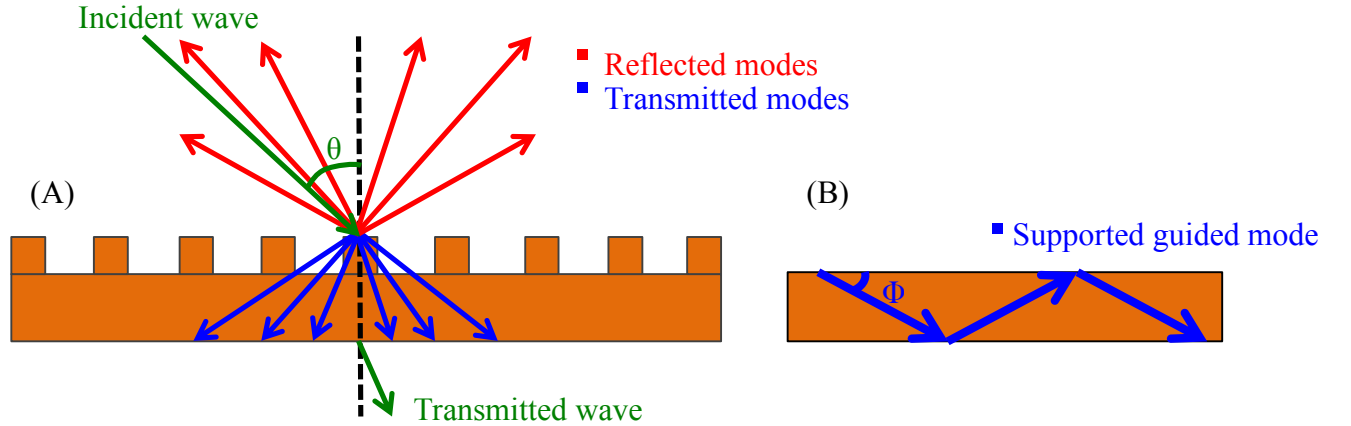


Figure 2.7. (A) Depiction of an incident wave illuminating a diffraction gratings and the resulting reflecting and transmitting discrete modes, (B) Wave guiding of a supported diffracted mode

The phase shift in the diffracted modes aforementioned is due to the addition of the phenomena of classical diffraction and the Fresnel phase shift, which are present where there

exists a shift in phase due to the refractive index difference from the modulated space to the waveguide region [36].

Mathematically, the guided mode resonance phenomenon can be explained using the grating equation and the propagating modes inside of the waveguide. However, Maxwell's equations are employed in order to find the amplitude of the diffracted modes, while the grating equation is used to find their directions [37]. The grating equation is as follows [9].

$$\sqrt{\epsilon_{avg}} \sin \theta_m = \sqrt{\epsilon_{inc}} \sin \theta_{inc} - m \frac{\lambda_0}{\Lambda} \quad (2.1)$$

Where ϵ_{avg} represents the average dielectric constant considered for the direction of the calculated modes, θ_m is the angle of the m^{th} mode, ϵ_{inc} is the surrounding dielectric constant of the medium, θ_{inc} represents the angle of incidence of the incoming wave, λ_0 is the free space wavelength of the incoming wave, m is mode being calculated and Λ is the grating period of the filter. As observed in the grating equation, the angles of the subsequent spatial harmonics are dependent on the used materials and the contrast in refractive index in the modulation, as well as the incidence angle of plane wave, its frequency and the grating period of the GMRF. Focusing on the second phenomenon involved, the discrete modes will be supported by the waveguide if its index of refraction is greater than neighboring medium and less than that of the dielectric material serving as the waveguide, as illustrated by Equation 2.2 [9].

$$\sqrt{\epsilon_{inc}} \leq \left| \frac{\beta_m}{k_0} \right| \leq \sqrt{\epsilon_{avg}} \quad (2.2)$$

Where the constant of propagation is represented by β_m and k_0 is the free space wave number. In order for the mode to be supported, the phase of the diffracted mode must match the phase of the waveguide as follows

$$\left| \frac{\beta_m}{k_0} \right| = \sqrt{\varepsilon_{avg}} \sin \theta_m \quad (2.3)$$

If this condition is satisfied, the guided mode will be supported and begin to propagate inside of the slab waveguide. Due to the leaky nature of the structure, the wave guided mode will eventually escape the structure interfering with the incoming wave and producing a resonance response. Finally, these equations can be combined to evaluate the resonance behavior in terms of the incident angle, as follows

$$\sqrt{\varepsilon_{inc}} \leq \left| \sqrt{\varepsilon_{inc}} \sin \theta_{inc} - m \frac{\lambda_0}{\Lambda} \right| \leq \sqrt{\varepsilon_{avg}} \quad (2.4)$$

From Equation 2.4, it can be observed that the resonance frequency of the device is also dependent on the incidence angle of the incoming plane wave. Overall, the resonance frequencies of guided mode resonance filters have shown particularly high sensitivity to the angle of incidence [38]. Moreover, GMRFs share the period sensitivity with frequency selective surfaces in the sense that a greater amount of periods results in better performance of the device. These limitations can hinder the performance of GMRFs in particular applications where the incoming wave is not perfectly aligned with the designed incidence angle to the grating surface or in frequencies where the periodicity of the device can result in extremely large devices for reasonable performance, such as the lower end of the radiofrequency spectrum.

2.6 Introduction to metamaterials

The interaction of light with regular materials is influenced by different parameters such as the particle size of matter and the wavelength of the travelling electromagnetic radiation. This can be observed in the interaction of visible light with naturally occurring materials, such as dielectric ceramics, where the atomic arrangement (building blocks) of the illuminated material

is significantly smaller than the wavelength of the passing electromagnetic wave. Due to this, the wave will “see” the material as a homogeneous structure, despite of its crystal structure, due to the size difference aforementioned, and a common material-wave interaction will take place. However, in recent years, there has been an increasing interest in the development of new types of materials known as metamaterials. Metamaterials are engineered materials that show properties that are not conventionally found in naturally occurring materials [39]. Metamaterials are composed of individual, identical elements arranged periodically in a lattice, analogous to crystal structures [40]. Ideally, the inhomogeneity introduced by the periodic elements in the structure will be discarded by the working wavelength, due to the size difference, resulting in a “homogenous” material; however, the combination of the factors aforementioned yields extraordinary properties. These properties can result in characteristics such as negative refractive index, reverse Doppler effect, backwards propagation, and reversed Vavilov-Cerenkov radiation [41]. Particularly, in electromagnetic metamaterials, these properties are related to the permittivity (ϵ) and permeability (μ) of the composite material achieved through the arrangements aforementioned. These properties have allowed for metamaterials to be implemented in a broad range of applications such as antennas, cloaking devices, sensors, lenses and energy harvesting and are among the most promising technologies for light manipulation applications. However, the concept currently extends to other areas such as mechanical and thermal concepts and applications. Examples of metamaterials’ unit cell designs or “meta-atoms” can be observed in Figure 2.8, while fully developed metamaterials structures are portrayed in Figure 2.9.

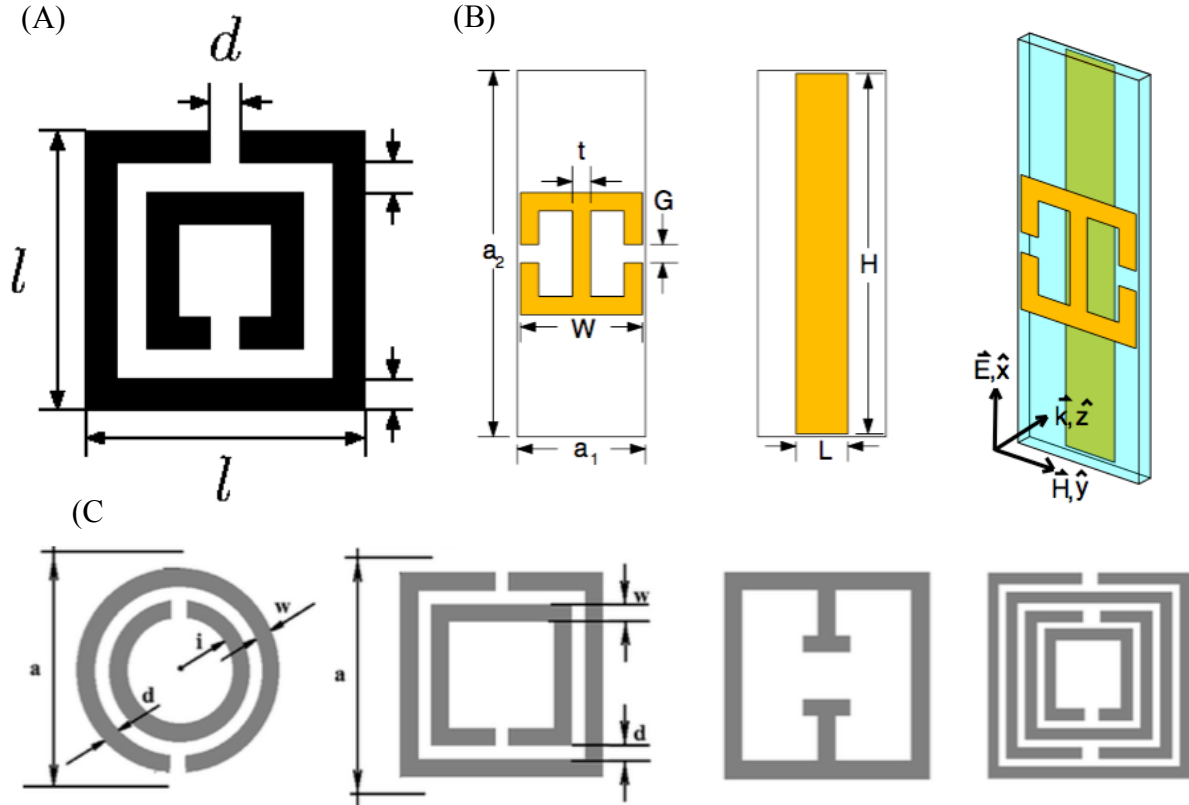


Figure 2.8. Examples of meta-atoms developed in literature thus far [40 – 42]

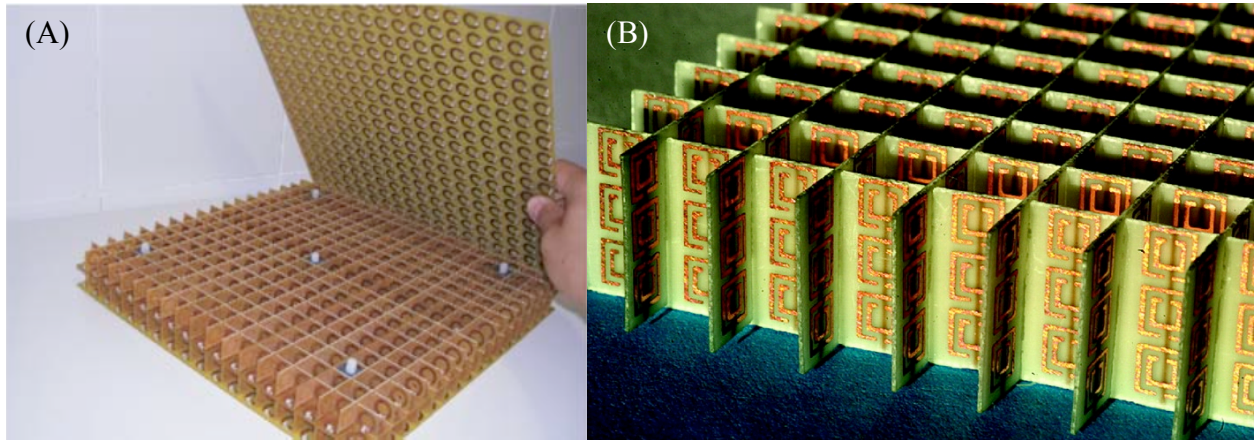


Figure 2.9. Examples of developed metamaterials structures, (A) Structure with capacitively loaded rings for MRI [43] (B) Split ring resonator structure for negative refractive index applications [44]

The concept of metamaterials was envisioned in 1967 by Victor Veselago, who proposed and developed the framework for materials that had simultaneously negative values of dielectric permittivity and magnetic permeability and their interaction with electromagnetic waves [45].

Veselago explored analytically this type of materials and named them “left-handed materials” due to the vector triplet formed between the electric field (**E**), magnetic field (**H**), and propagation (**k**) vectors [45]. Based on Veselago’s study, the interest for this newly developed concept resurged in recent decades, opening up new areas of development for optical devices. In 1996, Pendry et al. proposed a structure composed of thin (1 μm in radius) metallic wires arranged in a cubic lattice capable of achieving a negative effective permittivity below the plasma frequency [46]. Furthermore, in 1999, Pendry et al. suggested several magnetic tunable microstructures, such as arrays of metallic cylinders, swiss rolls, and split rings capable of reaching negative effective permeability values [47]. After that, in 2000, Smith et al. demonstrated an artificial material formed of split rings and thin wires with effective negative values of both permittivity and permeability [48]. Shelby et al. experimentally demonstrated a metamaterial composed of split ring resonators displaying a negative index of refraction in the X-band frequency region in 2001 [49]. Shelby’s achievement marks the first experimental confirmation of a metamaterials device and its unique properties.

As mentioned before, the extraordinary properties of metamaterials are derived from their structure, relation between the wavelength and the size of the periodic element and its resulting relative homogeneity. As a consequence of their design, metamaterials have simultaneous negative values for their effective dielectric permittivity (ϵ_{eff}) and permeability (μ_{eff}). Dielectric permittivity (ϵ) and permeability (μ) are bulk material properties that describe a material’s interaction with electric and magnetic fields, respectively. Therefore, these properties dictate the propagation of electromagnetic radiation through matter [45]. A propagating electromagnetic wave through an isotropic material can be described with the following equation:

$$k^2 = \frac{\omega^2}{c^2} n^2 \quad (2.5)$$

Where k represents the wave propagation vector, ω is the angular frequency of the wave; c is the speed of light and n is the refractive index associated with the material. The refractive index

determines how a wave propagates inside a medium and it's dependent on the dielectric permittivity and permeability; it can also be denominated as a ratio between the speed of light in vacuum and its speed inside of the material under consideration, as observed in Equation 2.6.

$$n = \sqrt{\epsilon\mu} \text{ or } n = \frac{c}{v} \quad (2.6)$$

Where v is the wave velocity inside of the material. Moreover, when an electromagnetic wave travels through a boundary between two different isotropic materials, due to a change in the material properties, the incidence and refractive angles will be different. This is portrayed in Snell's law, as observed in Equation 2.7.

$$\frac{\sin\theta_1}{\sin\theta_2} = \frac{n_2}{n_1} \rightarrow \frac{\sin\theta_2}{\sin\theta_1} = \frac{\sqrt{\epsilon_1\mu_1}}{\sqrt{\epsilon_2\mu_2}} \quad (2.7)$$

Where θ is the angle associated with the traveling wave, n is the refractive index and the subscripts 1 and 2 are associated with the different media involved in the traveling of the wave.

The presence of negative values on the electromagnetic properties of materials has been documented before occurring in isolation. Negative values of dielectric permittivity have been found in metals such as silver near optical frequencies as well as negative permeability being present in ferromagnetic and antiferromagnetic materials with resonant behaviors [50]. However, the existence of simultaneous negative properties results in a reevaluation of the governing equations for electromagnetic behavior. The implications of having these properties can be detailed by observing Maxwell's equations with the analysis derived by Veselago, which will be discussed in a concise manner next [45].

Maxwell's equations and their constitutive relations represent instances where the dielectric permittivity and permeability appear independently and their effect can be studied in the same manner.

$$\nabla \times E = -\frac{1}{c} \frac{\partial B}{\partial t} \quad (2.8)$$

$$\nabla \times H = \frac{1}{c} \frac{\partial D}{\partial t}$$

Where:

$$B = \mu H \text{ and } E = \varepsilon E \quad (2.9)$$

When plane, monochromatic light is under consideration, where the proportionality $e^{j(kz - \omega t)}$ is applied, Ampere's and Faraday's law can be reduced to

$$\begin{aligned} k \times E &= \frac{\omega}{c} \mu H \\ k \times H &= -\frac{\omega}{c} \varepsilon E \end{aligned} \quad (2.10)$$

Where k represents the wave vector, E and H stand for the electric and magnetic fields, respectively; the respective right-hand and left-hand vectors can be observed from Equation 2.10 when evaluating for positive and negative values of dielectric permittivity and permeability, respectively. Further evaluation results in addition of a determinant value " p ", which can be found in Veselago's study [45]. This determinant represents the right-hand or left-hand behavior of a material and can be applied to Snell's law, effectively explaining the possibility of negative refractive index, as observed in the Equation 2.11.

$$\frac{\sin \theta_2}{\sin \theta_1} = \frac{p_1 \sqrt{\varepsilon_1 \mu_1}}{p_2 \sqrt{\varepsilon_2 \mu_2}} \quad (2.11)$$

Where p represents the determinant and can take values of +1 or -1 for right-hand or left-hand materials, respectively. Finally, in left-handed materials, the energy flux will travel in opposite

direction as the propagation, as detailed by Equation 2.12. An example of the aforementioned phenomenon is portrayed in Figure 2.10.

$$S = \frac{c}{4\pi} [EH] \quad (2.12)$$

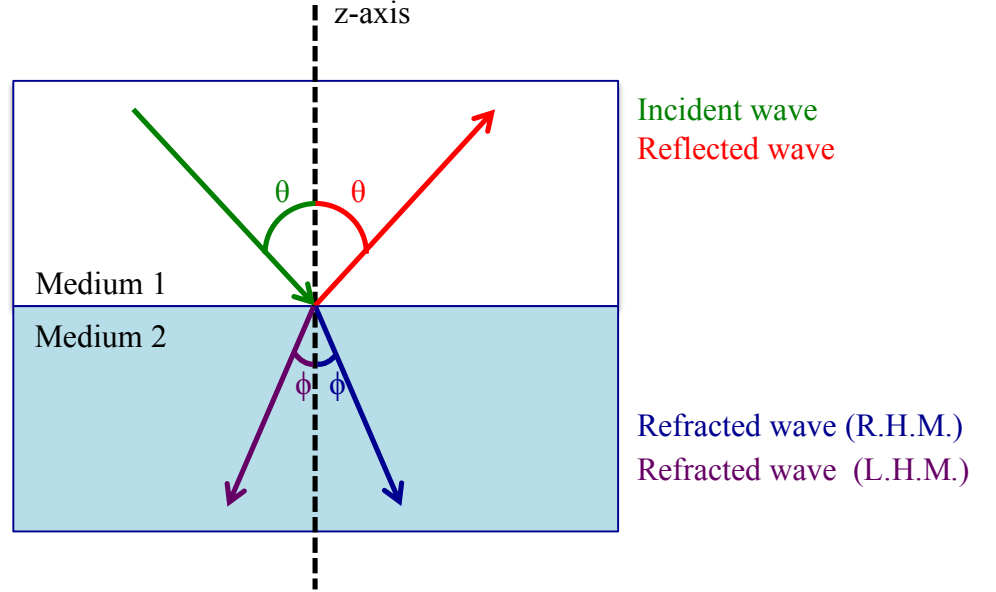


Figure 2.10. Representation of refractive indices for right-handed and left-handed materials

The presence of these extraordinary properties has opened new development opportunities in the fields of optics and photonics. Metamaterials could allow for the development of perfect lenses by utilizing a slab with a negative index of refraction, as devised by Pendry [51]. Furthermore, cloaking devices can be developed by employing metamaterial structures; this could be achieved by manipulating the electric and magnetic fields and the Poynting vector to avoid objects and flow around the object resembling a fluid [52]. There have been devices reported to cloak in the microwave and optical frequencies [53, 54]. The working mechanism of the cloaking device can be observed in Figure 2.11. Moreover, metamaterials have shown potential in power harvesting applications [55]. Finally, although the applications of metamaterials extend beyond those described here, this type of optical devices can be employed to develop wireless sensing systems [56]. However, metamaterials also present characteristics

that could hinder their performance. The most prominent limitations in several applications are frequency dispersion and narrow usable bandwidth [50]. The first refers to metamaterial properties being a function of frequency, while the second represents a problem when compared to naturally occurring materials [50].

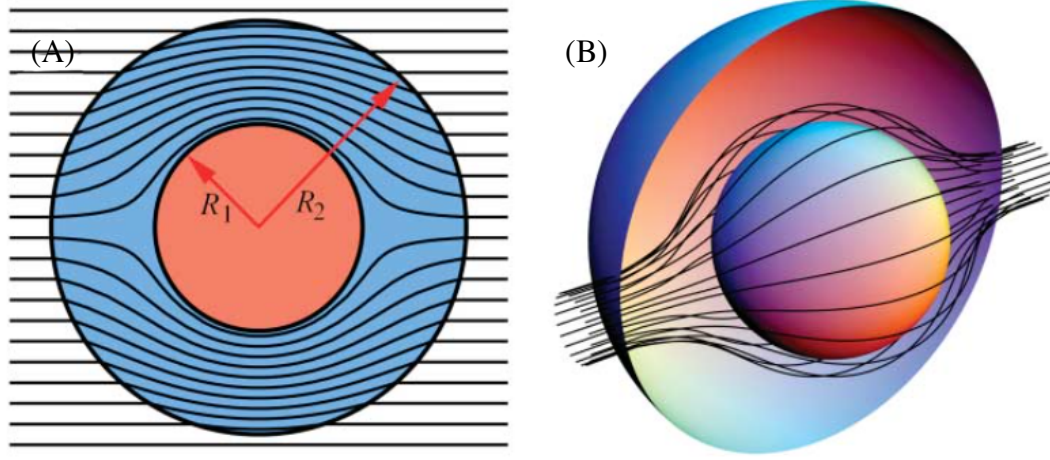


Figure 2.11. (A) 2D ray tracing around a material using a cloaking device, (B) 3-D representation of same phenomenon [52]

2.7 Recent development of guided mode resonance filters

Although, guided mode resonance filters have been under constant development for centuries, the last couple of decades have allowed for significant progress in GMRFs and their applications. The theoretical development, analysis and design of grating surfaces and GMRFs has seen significant progress in recent years due to the application of different electromagnetic and numerical models. Moharam et al. analyzed diffraction from planar gratings surrounded by different media and presented the first reported calculations for slanted diffraction gratings [57]. Wang et al. studied the propagating and evanescent fields of GMRFs by employing rigorous coupled-wave theory and predicted the resonance locations using eigen value equations [58]. Furthermore, Magnusson et al. described in detail a theoretical characterization of the working principle of dielectric guided mode resonance filters as well as the polarization driven by the transverse electric (TE) and transverse magnetic (TM) modes and suggested potential

applications [32]. Subsequently, Wang detailed the physics of GMRFs using rigorous coupled wave and classical slab waveguide theories demonstrating that modulation of the grating amplitude affects the linewidths of the resonances [59]. The use of a Floquet boundary condition, a type of boundary condition employed for simulating infinitely repeating structures and one of the most commonly used in contemporary commercial software, was implemented to the Finite Difference Time-Domain (FDTD) to simulate frequency selective surfaces by Harms et al. [60]. Another study was reported that involved the use of FDTD to study the energy confinement and the employment of reflectors in the waveguide region [61]. These and other theoretical analyses have allowed for the design and development of several GMRF-based devices and technologies, which will be discussed next.

In terms of device development, GMRFs have been receiving increasing attention due to their broad range of applications. Several design approaches have been explored resulting in successful proposed and fabricated filters, as discussed next. Wang et al. reported improvement in the performance of guided mode resonance filters when employing multi-layered homogeneous materials with the layer containing a spatial modulation, resulting in low sideband reflectance [62]. Additionally, Tibuleac et al. characterized the performance of different multi-layered designs for GMRFs near optical frequencies concluding that the narrow linewidths can be achieved with minimal layers [63]. Moreover, Rosenblantt et al. fabricated GMRFs using passive dielectric and semiconductor materials achieving robust structures for optical switches, modulators and filters [64]. Moreover, a GMRF with the capability of tuning spectral reflectance was demonstrated with a varying azimuthal angle from 0° to 90° [65]. The angle of incidence can serve as an advantage or challenge when designing this type of optical device due to its sensitivity to the incidence direction of light. For instance, Sang et al. have developed a filter composed of a surface with anti-reflective properties at oblique incidence of light [66]. Additionally, the number of periods has an important role in a performance of the device. As mentioned before, as the number of periods is increased, the performance of the GMRF will become closer to its ideal value. Barton et al. designed and characterized an all-dielectric GMRF

capable of operating with seven periods by creating an artificially infinite medium through the addition of reflectors [31]. Furthermore, Barton, et al. designed and developed an alternative for metallic filters in high power applications by devising an all-dielectric frequency selective surface employing the phenomenon of guided mode resonance capable of operating at 1.7 GW/m² of power employing only 8 periods in the microwave regime [67]. GMRFs have also been developed to serve as feedback mechanism for design-derived spectra for fiber lasers [68]. Aside from all-dielectric FSSs, devices with metallic gratings or cladding have also been reported [69]. Finally, pertinent to the project presented is the development of sensing devices based on this technology. GMRFs have seen development in the area of biosensing. Kaja et al. developed a guided mode resonance filter capable of measuring the bioassay of protein biomarkers for ovarian cancer detection [70]. Additionally, Jia et al. studied the sensitivity of GMRFs biosensors when studying different initial peak-wavelengths [71]. Although highlights of the development of GMRFs were presented in the previous paragraphs, literature regarding wireless sensing and the use of metal-dielectric-metal structures was scarce and it can be concluded that these optical devices still have room to explore different configurations and potential applications.

2.8 Recent development of metamaterials

Metamaterials have attained growing interest due to their unprecedented properties and their potential applications. Even when metamaterials have been in development for only two decades, significant progress in theoretical and experimental development has been achieved. Moreover, several applications in different areas ranging from cloaking to sensing have been demonstrated and will be detailed in this section. Theoretical understanding of metamaterials has evolved since Veselago's proposal. Calculations of the effective dielectric permittivity and permeability have been developed in the past for left handed metamaterials [72, 73]. Additionally, different theoretical models have been developed for the analysis and design of metamaterial structures. Simovsky et al. detailed a theory for the homogenization of electric and

magnetic dipoles in a lattice and demonstrated the extraction of material parameters from scattering matrix [74]. Moreover, a branch of theoretical development has surged based on equivalent circuit models for metamaterial structures. Equivalent circuit models (ECMs) consist of analyzing the role of each component of the structure and detailing in a circuit diagram as an inductor, capacitor or resistor. Biloti et al. devised a quasi-static equivalent circuit models for different magnetic structures such as multiple split ring resonators (MSRRs) and spiral resonators [75]. Moreover, an equivalent circuit model for split ring resonators (SRRs) and complementary split ring resonators was developed and tested by Baena et al. [76]. Aside from equivalent circuit models, models based on microwave circuit theory have been developed that result in advantages over other solutions [77]. The main difference is the ability to obtain the subsequent resonances besides the fundamental resonant frequency [77]. Finally, the possibility of using metamaterials for invisibility [78] and infrared [79] applications have been explored.

Split ring resonator (SRR) geometries and complex designs derived from this structure have also been extensively explored for metamaterial applications. Studies have been performed comparing different SRR structures for optimal design and applications [80, 81]. Karim et al. performed a study of particular interest for wireless metamaterial temperature sensor development in which several resonator structures were compared in simulations and the closed ring resonator (CRR) resulted in enhanced sensitivity and response over other options found in literature [82]. Aside from the studies of metamaterial structures on the element-wise scale, there have been advancements in the application of such structures at different frequency ranges. Cloaking devices have been designed and demonstrated through numerical methods/simulations for optical frequencies by employing thin wires and a dielectric substrate [53]. In the microwave frequencies, a cloaking device was achieved by employing SRRs [54]. Aside from cloaking, a novel application for metamaterials involves its use on the performance of mathematical operations through thin slabs and meta-screens [83]. Moreover, a lens with an extremely wide angle of incidence of 180° was designed and demonstrated [84]. Finally, returning to the sensor applications, Ekmekci et al. proposed metamaterial structures to serve as pressure, gas and

temperature sensors using broadside-coupled SRRs and V-shaped SRRs [56]. Additionally, Ekmekci described in detail several structures for multi-band applications in microwave and terahertz region based on several SRR structures and their potential sensor applications [85]. Karim also detailed the development of metamaterial structures based on CRR structures combining commercially available powder dielectric ceramics and commercial washers for wireless temperature sensors for harsh environments [86]. An example of bio-sensing is presented by Kabashin et al., who demonstrated a plasmonic metamaterial for label-free sensing [87]. Overall, metamaterials have shown potential to transform several electromagnetic applications with their unique properties and many promising technologies could be developed in the future with this type of optical device as its foundation.

2.9 Wireless temperature sensors

As mentioned in the previous chapter, the development of next generation temperature sensors has been in high demand in recent years due to the current design characteristics needed and the limitations of current solutions. As temperature remains one of the main parameters to be monitored in different components across a system or working environments, the necessity for the development of next generation sensors has remained a priority for all involved parties. Temperature sensors with novel capabilities have been documented in literature in recent decades. One of the most prominent technologies for sensor development is based on Surface Acoustic Wave (SAW) devices. A hybrid SAW sensor capable of measuring temperature and pressure up to 130°C was developed by Schimetta et al. with sensitivities of ± 15 kPa and $\pm 10^\circ\text{C}$ [88]. Moreover, Ballandras et al. reported a sensor for temperature measurements of immersive applications [89]. SAW progress was also achieved by Hornsteiner et al. through the utilization of lithium niobate (LiNbO_3), quartz and langasite ($\text{La}_3\text{Ga}_5\text{SiO}_{14}$) for temperature sensing devices achieving a maximum operating temperature of 1060°C for the third material option [90]. Opasjurnskit et al. developed a temperature sensor using complementary oxide semiconductor materials and performing the interrogation with an RFID backscattering technique [91]. Another

sensor based on RFID tags was developed by Girbau et al. by utilizing sensor tags without a chip, which is was used for a temperature range from 30 – 130°C [92].

Aside from SAW sensor development, alternatives have been explored in an effort to achieve several alternatives and cover specific applications. Resonant LC circuits have been researched for temperature sensing alternatives. For instance, Wang et al. reported the development of a wireless temperature sensor using an inductor-capacitor (LC) resonant element based on a telemetry scheme for rotating components capable of working on temperatures up to 235°C [1]. Ong et al. devised a platform composed of a resonant, TiO₂ coated, LC circuit capable of sensing humidity, temperature, complex permittivity and pressure [93]. Their sensor achieved a sensitivity of 6.4 kHz/°C. Thai et al. developed a wireless temperature sensor based on SRRs and micro-cantilevers operating at 31 GHz and a sensitivity of 150 MHz/°C [94]. A sensor based on single-crystal sapphire disks and zirconia prism was also developed for high temperature and corrosive atmospheres [95]. This sensor is capable of sensing up to 1600°C with an emphasis on accuracy and resolution. Moreover, Cheng et al. demonstrated a novel passive wireless sensing mechanism capable of sensing up to 1050°C based on a slot patch antenna with a sensitivity of 0.58 MHz/°C [96]. Their integrated design allowed for the patch to serve as both the sensing device and radiating source. As detailed in the previous section, metamaterials have been proposed for temperature sensing applications. Ekmkeci et al. designed a multipurpose sensor based on a multi-layer dielectric coupled with double-sided split ring resonators (DSRRs) capable of operating in the microwave frequency range [97]. This sensor is able to determine the variation of different parameters such as humidity, temperature and pressure through the effect of these environmental conditions on the middle-layer dielectric and, hence, its effect on the resonant frequency of the device. This device can be observed in Figure 2.12.

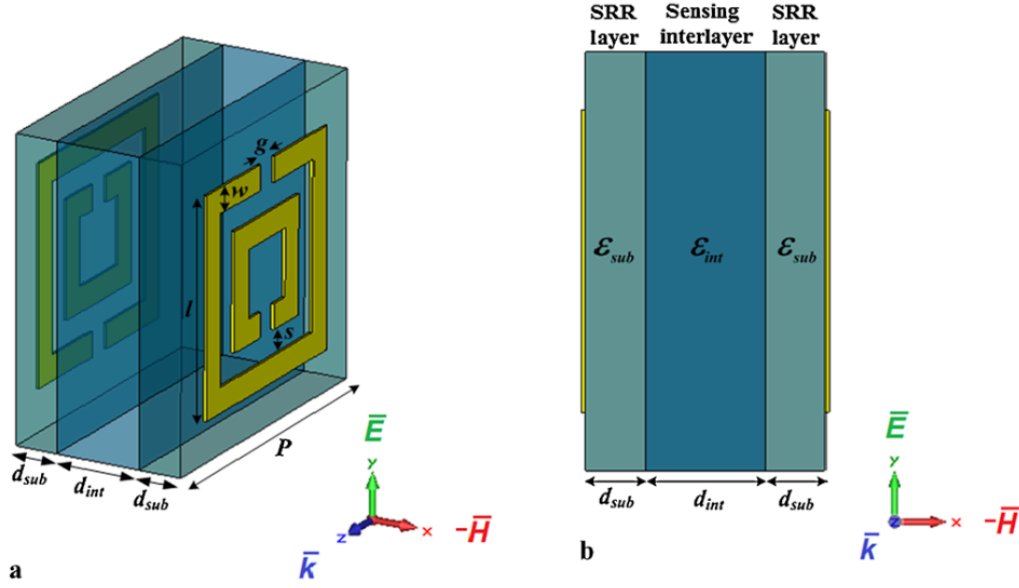


Figure 2.12. Ekmkeci et al. proposed unit cell for multi-functional sensors [97]

Although wireless temperature sensing has seen promising development in recent years, there still exists room for alternatives and improvements. Several sensing solutions employ materials that could see their properties negatively impacted with temperature variation. Moreover, an emphasis has been made in recent years to develop temperature and other type of sensing devices capable of operating at harsh environments. For instance, in aeronautic vehicles, the temperatures could range from cryogenic temperatures to a maximum of 1500°C [98]. Therefore, further development of sensing solutions needs to be achieved employing materials capable of withstanding these adverse conditions. Metamaterials and guided mode resonance filters have the potential to enable a new dimension of wireless sensor development allowing for several combinations and structures for different applications.

2.10 Conclusion

In this chapter, an extensive description of the technologies employed in this research project has been given. The definition of frequency filters in the form of FSSs and GMRFs and their working mechanism were explored. Additionally, the components of GMRFs were detailed in an effort to broaden the understanding of such devices. Metamaterials were also discussed in

detail encompassing their historical development and working mechanism. Relevant recent development in these technologies was discussed as well as in the area of wireless temperature sensors. Overall, while an overwhelming amount of research has been performed in the areas aforementioned, there still exist challenges and limitations that need to be addresses in order to attain reliable sensing devices based on these emerging technologies.

Chapter 3: Finite Element Modeling and Simulation

3.1 Introduction

The design and modeling of the proposed wireless temperature sensors constitutes one of the main pillars of this research project due to the effect of different parameters such as unit cell dimensions, geometry of the periodic structures, material selection and number of periods in the structure, which affect the overall response of the sensor. For the GMRF sensor, the material selection and a basic analytical approach, considering the targeted response, were performed to allow for the fundamental unit of the sensor to be designed. After that, ANSYS High Frequency Structure Simulator (HFSS) 15.0 was employed to characterize the response of the sensor, optimize the design of the unit cell in order to achieve the desired result and determine the number of periods needed in the finite array. A 3-D structure of the sensor's unit cell was developed in HFSS in order to approximate the response of the sensor given the calculated dimensions; after geometry optimization, the whole sensor was simulated to characterize its response. On the other hand, for the metamaterial-based sensor, a similar approach was taken based on previous work developed by Karim et al. A closed ring resonator (CRR) structure was simulated following identical steps: unit cell simulation, 1-D periodicity and full sensor array. The reflection response is presented for the GMRF, while both the reflection and transmission responses are shown for the metamaterial sensor. This chapter discusses the steps involved in the modeling and simulation of the GMRF and metamaterial wireless temperature sensors, as well as the effect of certain parameters on the sensor response and geometry comparison measures performed in order to achieve the best performance for the intended harsh environment applications.

3.2 Guided mode resonance filter sensor

3.2.1 Concept and design

The proposed guided mode resonance sensor consists of two metallic screens bonded to a dielectric ceramic slab on opposite ends to create a sandwich structure, as seen in Figure 3.1 (A).

On one of the metallic screens, a periodically repeated geometry is designed in order to allow the wave-sensor interaction to occur, as observed in Figure 3.1 (B). Since affordability is one of the main concerns in sensor development nowadays, a circular hole was selected as the periodic element due to its simplicity in design and ease of machinability. In principle, when a plane wave illuminates the grating surface, the repeated element will generate diffracted harmonic modes that will be reflected, coupled into the slab waveguide or become evanescent fields. In this sensor component, if a supported mode is found among the diffracted modes, it will be guided inside of the slab waveguide. Finally, due to the presence of the repeated element, the guided mode will leak outside of the structure and interfere with the incoming field, causing a resonance behavior. The key to the proposed sensor lies on the variation of the dielectric constant inside of the ceramic functioning as the traveling medium of the wave. This variation will allow for different modes to be supported inside of the waveguide, resulting in a shift in the resonance frequency of the device. It is hypothesized that in the design frequency used and for the intended use-case, the use of a metallic grating/cladding allows for better confinement of the guided fields, making the device less sensitive to external detrimental elements, such as ash or combustion byproducts accumulated on the surface of the device. The implementation of such design feature would allow for a more robust sensor in harsh environment applications such as combustion chambers.

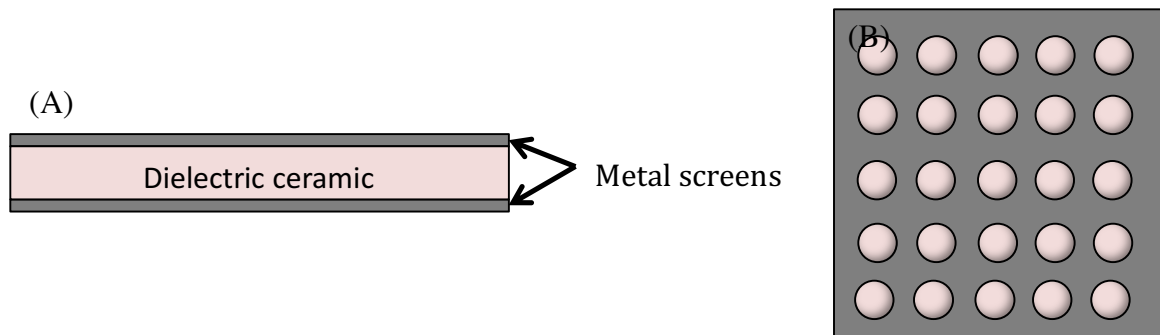


Figure 3.1. (A) Side view of the proposed sensor, (B) Top view displaying the metallic grating

The materials for the sensor unit were selected based on several factors such as properties, application, commercial availability and available information. As mentioned before, one of the main limitations for current passive wireless temperature sensors is the operating temperature of the components in energy conversion systems. For this reason, the initial materials selected were aluminum oxide (Al_2O_3 , alumina) as the dielectric ceramic and titanium as the metallic screens. The former was selected due to its temperature dependent and relatively low dielectric constant, orbiting around values of 9 for different configurations [99] and a melting point of $2,072^\circ\text{C}$. The latter was selected due to its high melting point of 1668°C . These material properties make them attractive prospects for component fabrication in harsh environment applications. The geometry of the sensor was defined based on the chosen response of 10 GHz in order to work in the X-band region. Based on the selected response and accounting for the selected materials, the unit cell dimensions were approximated using the following equation for the side length

$$l_{side} = \frac{C_0}{2f\sqrt{\epsilon_r}} \quad (3.1)$$

where C_0 represents the speed of light in vacuum, f is the targeted resonant frequency and ϵ_r is the relative permittivity of the dielectric ceramic. Additionally, the thickness baseline for the ceramic was determined by using Equation 3.2.

$$t_{dielectric} = \frac{l_{side}}{2} \quad (3.2)$$

After the calculations were performed for a working resonant frequency of 10 GHz and accounting for the material properties, the initial dimensions for the side length and dielectric thickness of the unit cell were 4.48 mm and 2.24 mm, respectively. An initial model was created

in HFSS with the specifications aforementioned. The evolution of GMRF sensor design will be explained in the upcoming sections.

3.2.2 Unit cell simulation and geometry optimization

In order to characterize the response of the sensor, the first step in the iterative design was to perform the simulation of an infinitely periodic array of the designed unit cell. A 3-D model of the initial unit cell was developed in HFSS following the dimensions calculated in the previous section. For all of the unit cell simulations, the following model configuration, boundary conditions and excitations were employed except when stated otherwise. The sensor's unit cell was modeled in the software by utilizing materials provided in the database. For the metallic screens, titanium was selected as the material and a thickness of 0.508 mm was employed. Additionally, 96% alumina with a dielectric constant of 9.4 was employed for the waveguide slab. An air box for the wave propagation was implemented on the model with an overall size of around half the design resonant frequency's wavelength to extend above and below the sensor model. This resulted in an overall height of 29 mm for the model. For the circular hole, a constant dimension of 3.34 mm was employed. In order to achieve an infinitely periodic array of unit cells, periodic boundary conditions (PBCs) in the form of Master/Slave conditions were employed in the x-z and y-z planes, where z is the vertical axis. Finally, Floquet port excitation was employed at the ends of the air box, on the x-y planes in order to comply with the PBCs. A representation of the model can be seen in Figure 3.2.

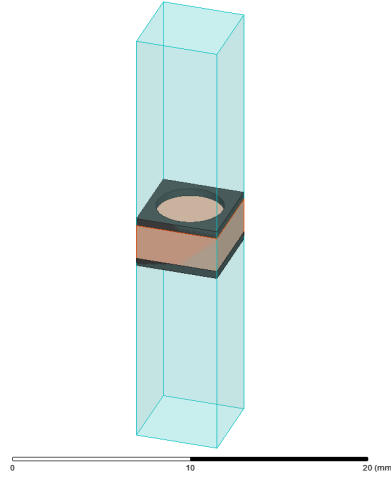


Figure 3.2. Representation of initial unit cell model

The first simulations were performed to locate the resonant modes of the device and to optimize the sensor unit cell to have a design resonant frequency of 10 GHz, as the initial calculations only provide a rough estimation. To achieve this, a simulation ranging from 0.1 to 25 GHz was performed using an interpolation method and a step size of 0.01. The initial results return a resonant frequency of 17.01 GHz and intensity of -6.35 dB. Due to the scalability properties of Maxwell's equations, sensor dimensions can be scaled up or down by the ratio of the actual and desired resonant frequencies. After performing these calculations, the sensor was scaled by a ratio of 1.701 in the x and y dimensions, maintaining the z direction constant due to the thickness of the materials; this resulted in the new side length dimension to be 8.223 mm. A simulation was then performed maintaining the parameters constant for consistency. An improved resonant frequency of 12.08 GHz resulted, which is visible in the X-band region; however, due the application of the device, temperature sensitivity can shift the resonance outside of the X-band window, making it untraceable by interrogating devices in this frequency range. Therefore, the sensor design was scaled once more by a factor of 1.208, resulting in the side length to be 9.934 mm. This resulted in a response of 10.11 GHz and intensity of -8.78 GHz. The evolution of the unit cell can be observed in Figure 3.3, while a comparison of the results can be observed in Figure 3.4.

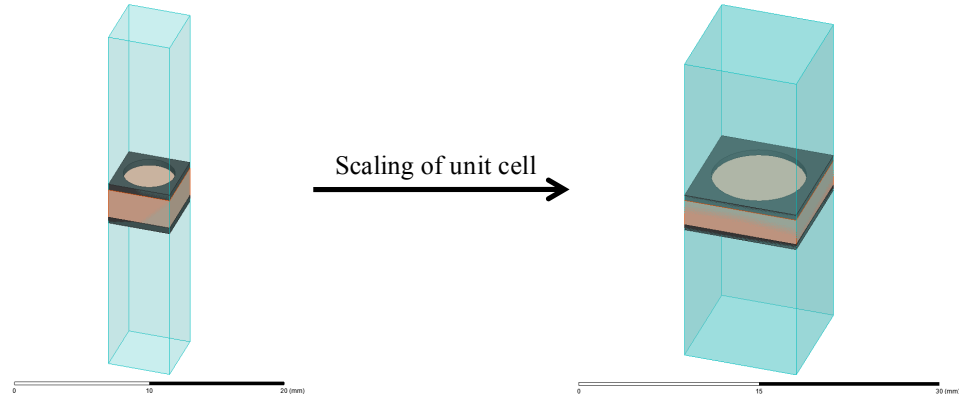


Figure 3.3. Example of unit cell scaling (4.48 mm \rightarrow 9.934 mm)

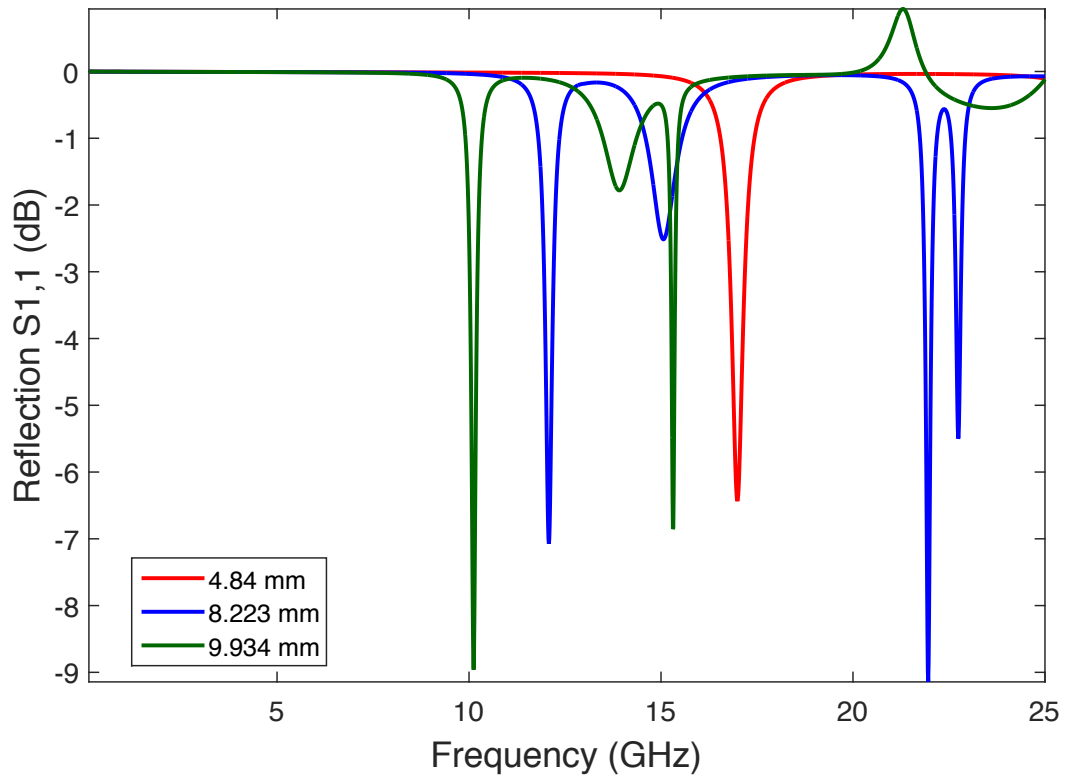


Figure 3.4. Comparison of the resonance frequency provided by side lengths utilized

As observed in Figure 3.4, the resonance frequency shifted with the scaling of the unit cell. At a side length of 4.84 mm, the fundamental mode of the resonance frequency can be observed at the 17.01 GHz mark. The resonance frequency reduced according to the increase of the side length dimensions. It can be observed that the scalability of the sensor results in an

iterative process, since both the achieved scaling operations resulting in a gradual change of the resonance frequency even though the calculations were performed utilizing the 10 GHz value. For the 8.228 mm and the 9.934 mm side lengths, resonance frequencies of 12.08 GHz and 10.11 GHz, respectively were found. Additionally, it can be observed that as the fundamental mode approached 10 GHz, the subsequent modes start to appear on the frequency window. These modes are subsequent harmonic oscillations that are supported by the slab waveguide and hence interfere with the incoming wave after leaking out of the structure. They could also be employed for temperature sensing if they become visible on the window. However, for simplicity, only the fundamental mode is targeted in these simulations.

After that, the unit cell design needed to match the dimensions of widely available materials with an aim of maintaining consistency in the simulation, fabrication and testing stages of the project. For the metallic screens, the dimensions of the titanium screen remained constant due to the availability of commercially available materials for fabrication. However, the alumina slab thickness needed to be modified in order to accommodate for the dimensions of high-purity alumina slabs physically available for building the devices. The thickness of the unit cell had to be reduced to 1.504 mm in order to match the dimensions of the devices that could be built with the materials found. The final dimensions for the unit cell of the sensor consist of a radius of 3.34 mm and thickness values of 0.508 mm and 1.504 mm for the titanium screens and the alumina slab, respectively. The side length of the sensor was changed from 9.934 to 9.705 as it yielded better results. The final dimensions are illustrated in Figure 3.5.

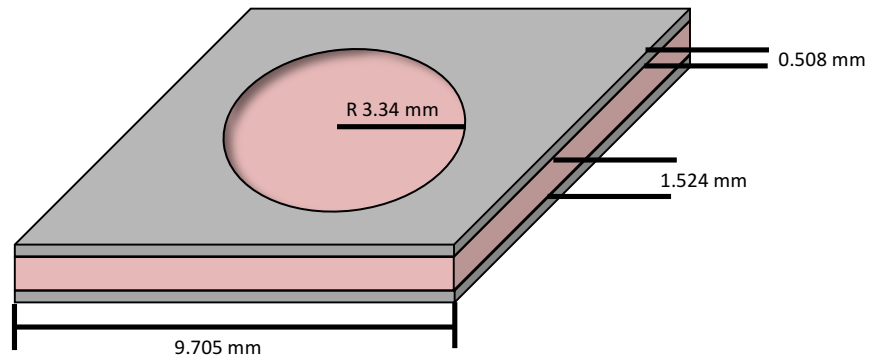


Figure 3.5. Summary of the dimensions of the GMR sensor unit cell

In this stage, simulation accuracy was emphasized since the resonant frequencies have already been located. In order to achieve a more accurate characterization, the solution method was changed from interpolation to discrete, the frequency window was narrowed to 8 – 12 GHz, closely resembling the x-band region, and the step size was reduced to 0.005. The final model of the unit cell can be observed in Figure 3.6.

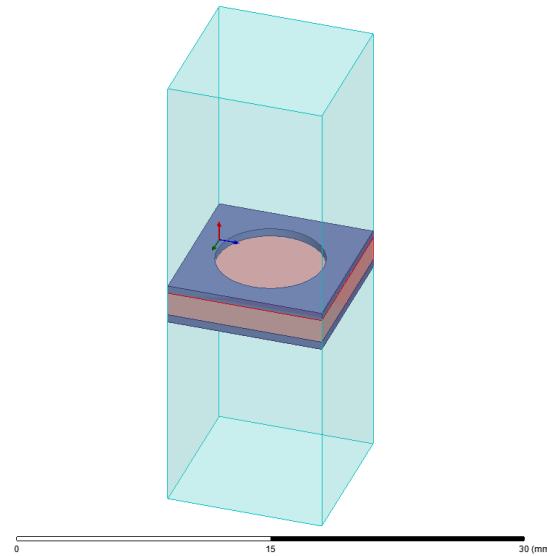


Figure 3.6. Trimetric view of the final model for the sensor's unit cell

This unit cell simulation yielded a resonance frequency for the fundamental mode of 10.065 GHz and an intensity of -16.8 dB. This frequency value is detectable in the X-band region, and provides flexibility for the resonance frequency to increase or decrease as a function of temperature. The simulation results for the optimized unit cell are presented in Figure 3.7.

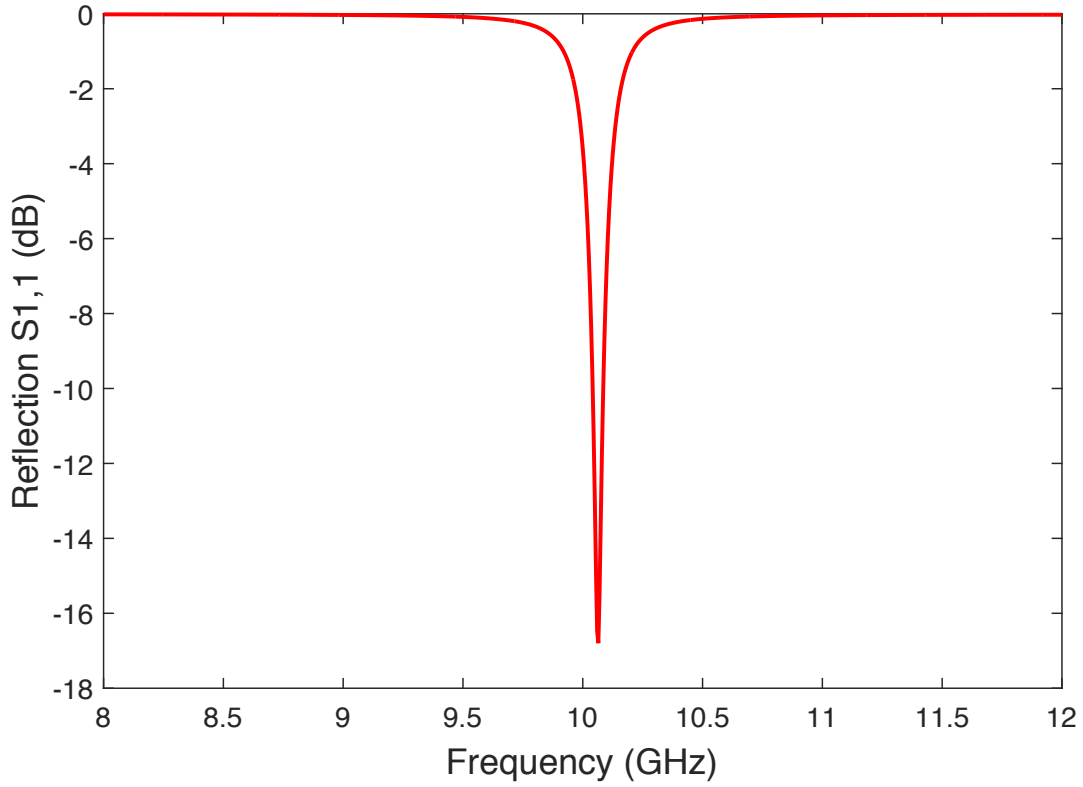


Figure 3.7. Reflection results for optimized unit cell simulation

After constraining the unit cell side length and the thicknesses of the materials, the effect of the circular aperture size was also studied. Aside from that, the effect of temperature was studied at the unit cell level for time optimization. These studies will be discussed in the upcoming sections.

3.2.3 Effect of the radius of the circular aperture

The circular apertures represent the first interacting elements of the incident wave and the designed sensor; therefore, their dimensions also have an effect on the overall performance of the device. To study the variation of the response of the sensor with the modifications of the circular apertures, an infinitely periodic simulation using the optimized dimensions was performed. A model was created following the boundary conditions and excitation stated before. For the varying circular aperture radius, a parametric variable was created and was assigned a range

from 0.5 to 4.5 mm increasing at a step of 0.5 mm. The original value of the radius was also considered for comparison. The results are observed in Figure 3.8.

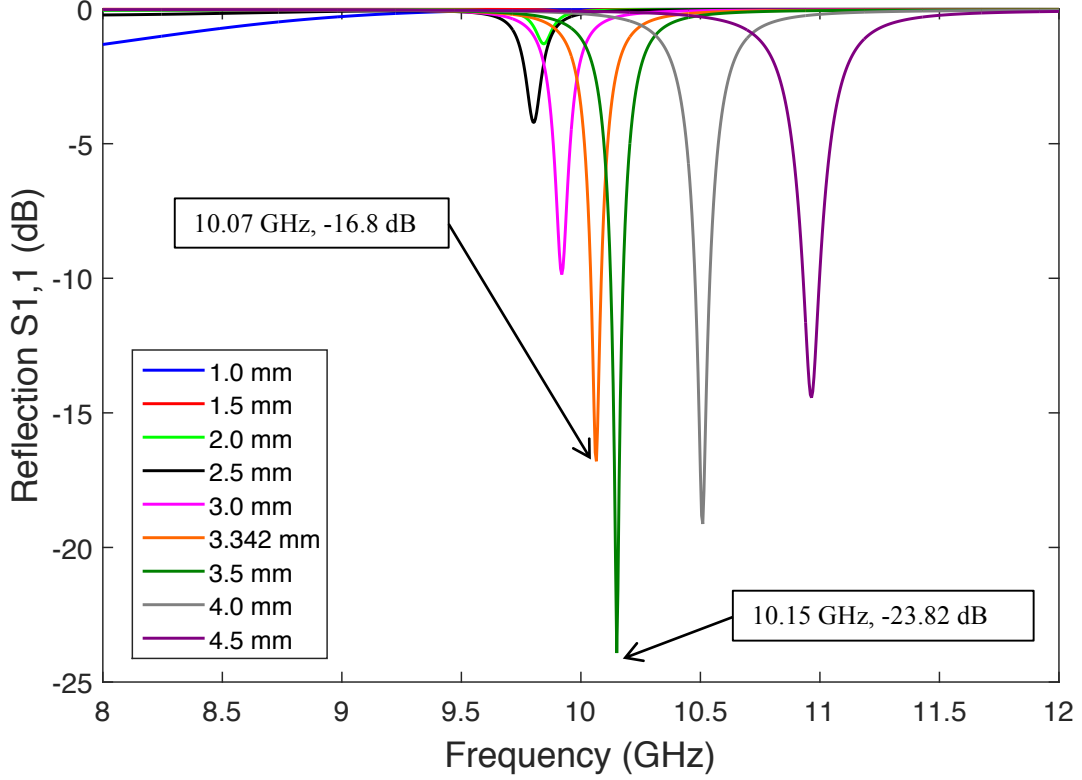


Figure 3.8. Reflection results for a varying circular aperture radius

It can be observed from Figure 3.8 that the resonance frequency of the sensor shifts with the variation of the radius of the circular aperture. Furthermore, it can also be concluded that an optimized value rather than a linear relation exists between the value of the radius and the location of the resonance frequency. For example, for the 1 and 1.5 mm radius, the resonance frequency is virtually non-existent. This behavior is due to the presence of mostly metallic surface on the top screen, inhibiting the interaction and energy coupling of the wave to the slab waveguide and instead resulting in mostly reflected waves, as observed in the results, comparable to a stop-band filter. The first visible resonance appears at 2 mm and the peak begins increasing in depth as the radius increases. Additionally, the optimal value for this dimension is between 3.342 and 3.5 mm, which yield resonant frequencies of 10.08 GHz and

10.15 GHz, respectively. However, the latter option results in an enhanced intensity with a value of -23.82 dB, compared to the -16.8 dB given by the 3.342 mm radius. As the circle increases in size, the resonance frequency drifts away from the designed value and becomes shallower. Therefore, it can be concluded that the radius of the circular aperture influences the behavior of the response and for the particular design frequency and in order to maintain the design goal between reasonable margins, a radius between 3.342 and 3.5 mm should be implemented.

3.2.4 Temperature influence on the response of the sensor

In order to prove the temperature sensitivity of the sensor and characterize the frequency shift with the variation in temperature, a simulation with different values of the dielectric constant of the alumina slab was performed. The model with the optimized dimensions was employed for this simulation. As for the dielectric constant range, values found in literature were employed [99]. The dielectric constant measurements performed by the authors can be observed in Figure 3.9.

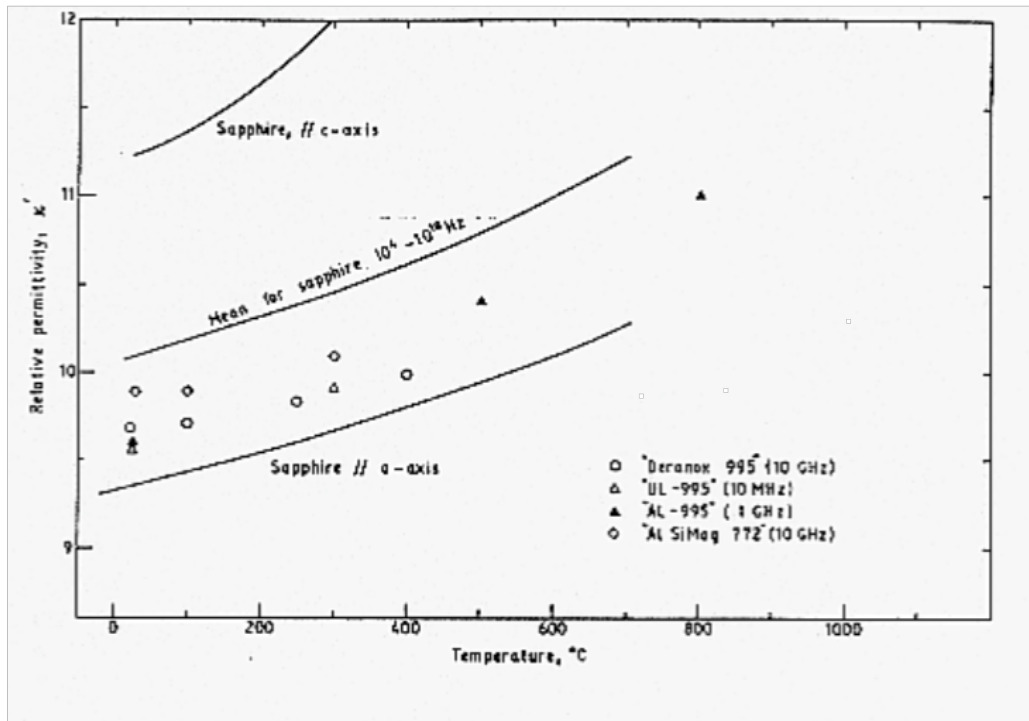


Figure 3.9. Relative permittivity values for 99.5% alumina at different frequencies [99]

The temperature range considered was from around 23°C to 401°C. The values for 99.5% pure alumina ceramic at 10 GHz were considered and were extracted utilizing Web Plot Digitizer. The exact values can be observed in Table 3.1. It is important to note that there exists a slight variation between the relative permittivity value offered by the software package and the one employed by this simulation. This is due to the different purities in the considered variation of alumina. However, for the demonstration of temperature sensitivity, the values provided in this section are appropriate. A parametric variable encompassing these individual relative permittivity values was created in HFSS and the simulation was run using a discrete solution method in a frequency range from 8 to 12 GHz.

Table 3.1. Temperature dependent dielectric constant of 99.5% alumina at 10 GHz [99]

Temperature (°C)	Dielectric constant
22.74	9.68
101.3	9.70
250.13	9.82
401.03	9.98

The simulation results yielded a variation of the resonant frequency with the change in dielectric constant, effectively demonstrating the sensor's sensitivity to temperature change. This is attributed to the dielectric properties of the ceramic and, as a consequence, its role in the waveguide sub-system of the device. As the dielectric constant changes, the supported guided modes will vary, modifying the response seen by the receiving antenna and effectively shifting the resonant frequency as a function of temperature. The resonant frequency decreased as the temperature increased, from a value of 9.92 GHz to 9.77 GHz at 23°C and 401.03°C, respectively. The sensor displays an average temperature sensitivity of 0.397 MHz/°C. The results for the temperature dependent simulation of the unit cell can be observed in Figure 3.10.

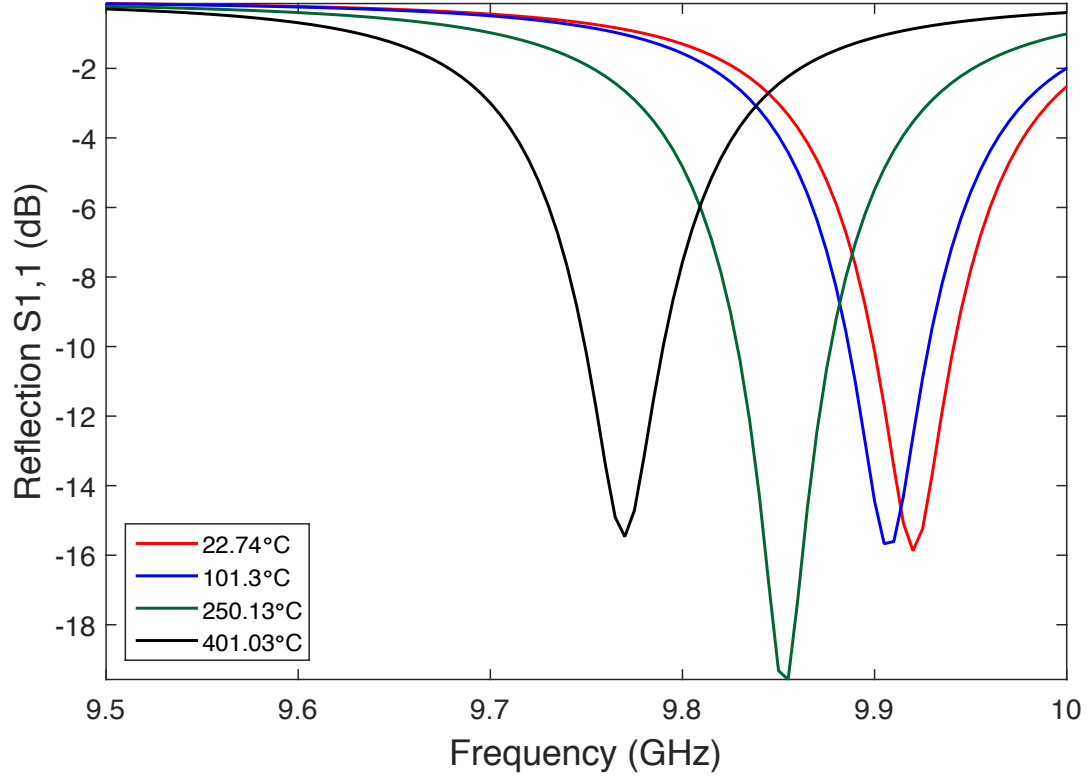


Figure 3.10. Temperature variation results for GMRF sensor

3.2.5 1-D periodicity simulations

After the unit cell was optimized, the number of periods had to be determined in order to assess the minimum size required for the sensor. As stated in the introduction, FSS and GMR filters achieve responses closer to the theoretical/simulated result as the periodicity tends to infinity. However, increasing the number periods in the grating to achieve an ideal response would result in unreasonable and impractical sizes for the sensor. Therefore, a reasonable size and response need to be achieved in order to maintain the performance of the sensor distinguishable and the size within adequate margins. In order to achieve this, simulations were performed focusing on varying the repetition of the unit cell. In order to achieve this, a model was created with the optimized dimensions and an initial number of 5 periods. To reduce the needed computing power and make the simulation more efficient, the model was constrained to be finite in the y-direction, while instructing HFSS to repeat the model in the x-direction. This

created a simulation where the modeled sensing device has a defined a number of periods along the y-direction, while repeating infinitely along the x-direction.

Due to the incompatibility of the Floquet port excitation with finite boundary conditions, a different model had to be developed for these simulations. A 3-D model using the same materials and the commercial dimensions was developed. For the initial study, a 5 period array was considered. The developed models consisted of an air box for the traveling wave, which is in contact with the infinitely periodic side of the sensing device. The model had a side length of 48.252 mm along the finite side. Additionally, on the finite side, a spacing of $\lambda/4$ was left between the limits of the air box and the sensor. For the boundary conditions, Master/Slave PBCs were selected for the infinitely periodic side, while Perfectly Matched Layers (PMLs), which are absorbing layers, were used on the finite sides, located on the outer sides of the air box. The PMLs were employed to absorb the wave reflections on the edge of the air box region and truncate the computations. For the excitation, an incident plane wave was selected and its vector components (**k**, **E** and **H**) were placed on the middle of the sensor with a propagation component (**k**) traveling along the z-axis in the negative direction. Additionally, in order for HFSS to calculate the S-parameters from the simulation, two PMLs were added on the top and bottom sides of the air box. The PMLs capture the reflected waves and calculate both the reflection and transmission spectra from the sensor interaction. Aside from the 5 period model, 10 and 15 period models were developed for comparison. These models had a finite side length of 97.05 mm and 145.575 mm, respectively. These models can be observed in Figure 3.11.

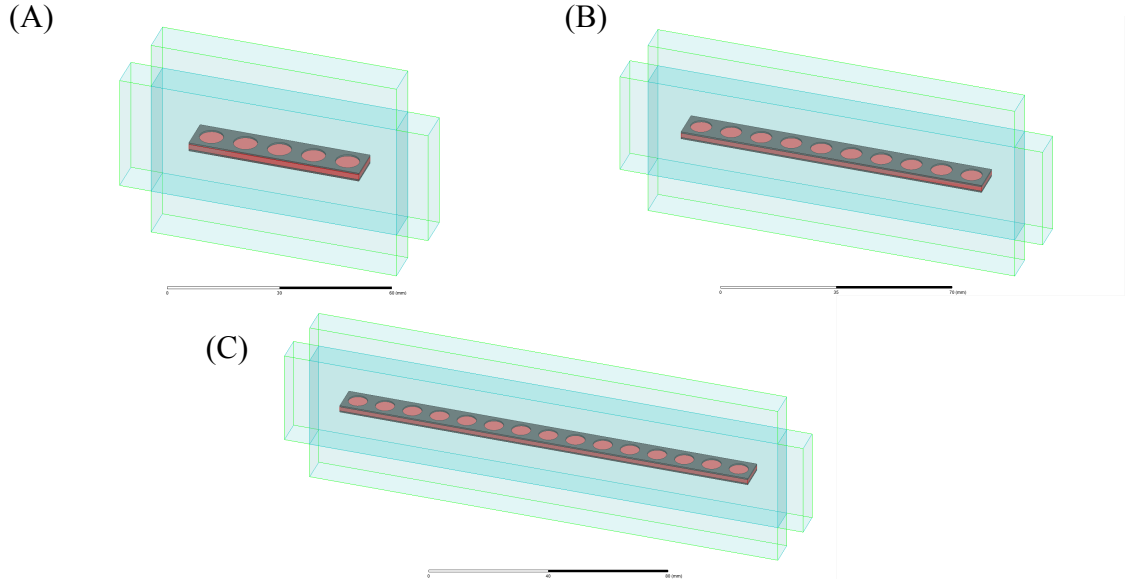


Figure 3.11. Developed models for (A) 5, (B) 10 and (C) 15 periods.

The development of these models required the addition of 2D material sheets covering the air box and the added PMLs in their entirety in order to achieve an integral model and, hence, an infinitely repeated structure along the x-axis. The addition of these sheets allowed for the application of the PBCs in the required planes. A discrete simulation within the X-band region was performed for each of these models with a step size of 0.005. A comparison was drawn between the results of the different variations of the sensor design. These results can be observed in Figure 3.12.

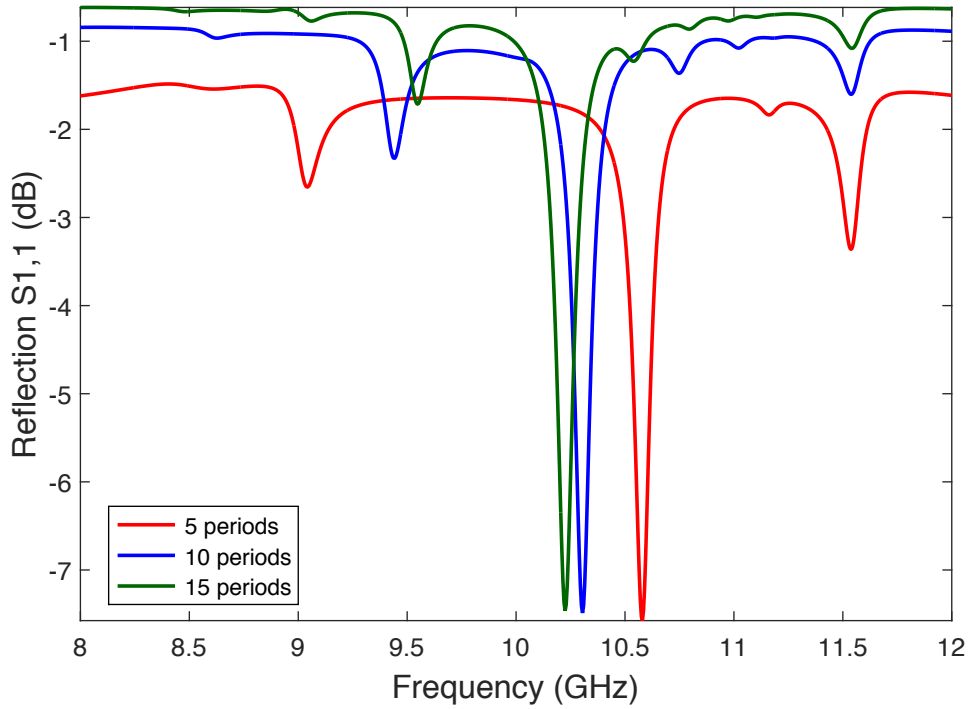


Figure 3.12. Reflection spectra comparison between the 5, 10 and 15 period models

From these results, it can be observed that the response of the sensor approximates the ideal value obtained by the infinitely periodic structure, indicating that the number of periods is of utter importance to the performance of the sensor, as previously stated. Additionally, it can be observed that secondary peaks are created on the response of the sensor, which tend to disappear as the periodicity increases. Moreover, it can be observed that for the structure with minimum number of periods, the sensor did not achieve pure reflection on the stop-band regions. Finally, the depth of the peaks decreased from -16.8 dB displayed by the infinitely periodic optimized unit cell to around -7.5 dB for all of the three different cases. Overall, the 3 different models showed a significant degradation of performance, which is associated with the finite dimensions and the assigned number of periods. As the electromagnetic radiation enters the waveguide structure after the interaction with the diffraction grating, the available length for the wave to travel inside of the waveguide is limited. This limited space results in a decay in the sensor

performance since the wave can escape from the finite sides of the sensor before it is completely leaked through the grating's apertures.

In order to mitigate this problem, a modification to the sensor design was made by adding 0.508 mm thick titanium plates to the finite ends the model, covering the potential escaping paths for the wave. These modifications are based on the work previously developed by Barton et al. [31]. The addition of the reflectors results in the creation of an artificial infinite medium, allowing the wave to travel inside of the sensor and preventing energy leakage from the open sides. This emulates the first model created. The upgraded model can be observed below.

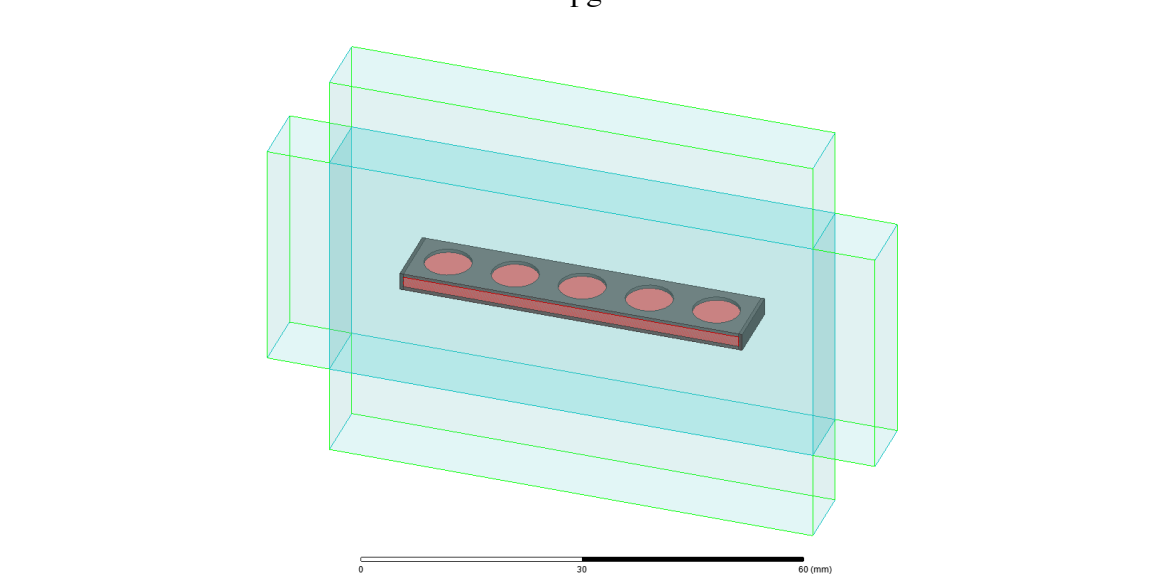


Figure 3.13. 1-D periodicity simulation with reflectors on finite ends

After the simulation was performed, an improvement on the performance of the sensor was observed in the reflection spectra. Due to the restriction in the exit paths of the wave through the addition of reflective surfaces, the wave is allowed to travel inside of the waveguide and prevented from escaping, allowing for the energy leakage to occur through the apertures. The addition of the reflectors results in a resonance frequency of 10.15 GHz and an intensity of -17.29 dB. This confirms the creation of the artificially infinite medium inside of the sensor, as the results are comparable to those obtained for the infinitely periodic simulations. The results can be observed in Figure 3.14.

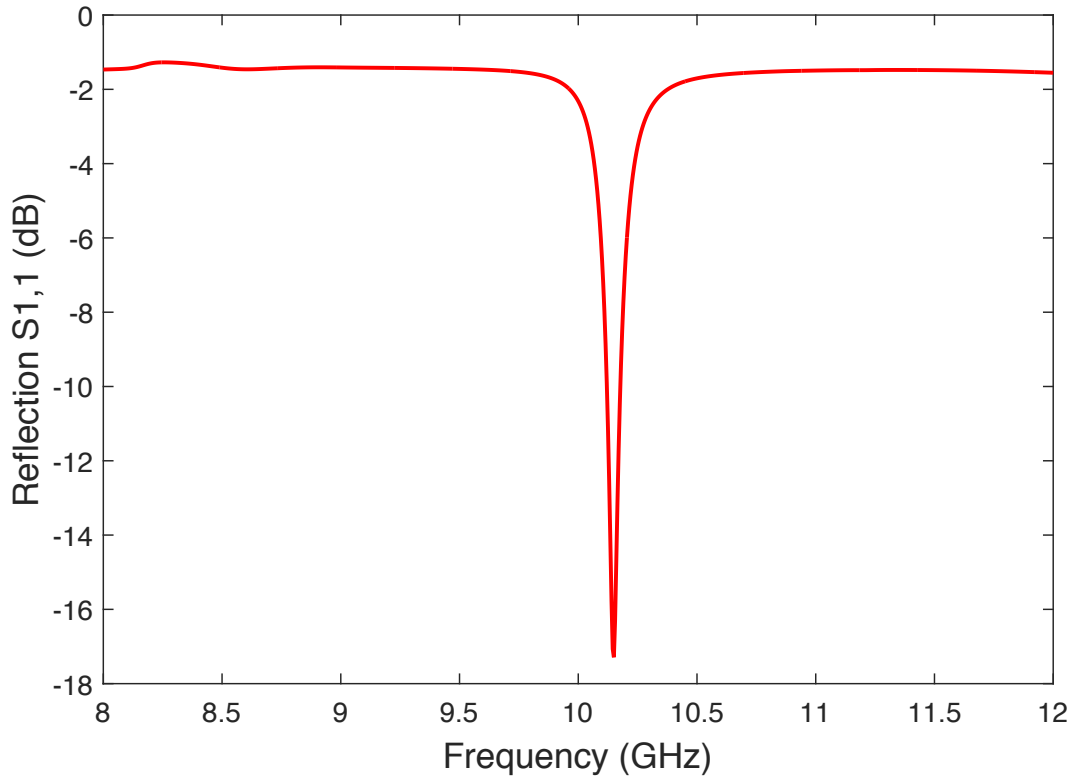


Figure 3.14. Reflection spectra for 1-D periodicity with reflectors

The addition of the reflecting walls can result in the use of fewer periods for the temperature sensor. This allows for the use of constrained dimensions for different sensing applications. For this research project, the number of periods was limited to a square array of 5x5 in order to achieve dimensions of 48.525 mm per side for the top plate and an overall thickness of 2.54 mm. With the added reflectors, the final side length of the sensor was of 49.541 mm. For the next stage, a full-sensor simulation was performed to evaluate the response of the device as the idealized conditions are removed from the model. These simulations are discussed in the following section.

3.2.6 Full sensor simulation

The final simulation for the GMRF sensor consisted on the assessment of the performance of the full sensor for the reflection spectrum. To confirm the response of the sensor with previous simulations, a model was developed following the design of the tri-layer structure with the implementation of the reflective surfaces. The developed model featured a 5x5 array of circular apertures on the grating layer. With this design, the sensor had side length dimensions of 49.541 mm and a total thickness of 2.54 mm. For the simulation, the air-box was extended on all side-length dimensions to leave a $\lambda/4$ spacing between the edge of the air-box and the sensor sides. Additionally, as with all previous simulations, a separation between the sensor and the top and bottom edge of the air-box of close to $\lambda/2$ was left for the wave travel. For the model, PMLs were added on the boundaries of the air-box in the x-z and y-z planes to limit the simulation space to the interactions inside the air box. Waveports were added as the excitation on top and bottom of the air-box on the z-directions, since Floquet ports were not compatible with the boundary conditions and incident plane wave resulted in no reference to extract the results. The model is shown in Figure 3.15.

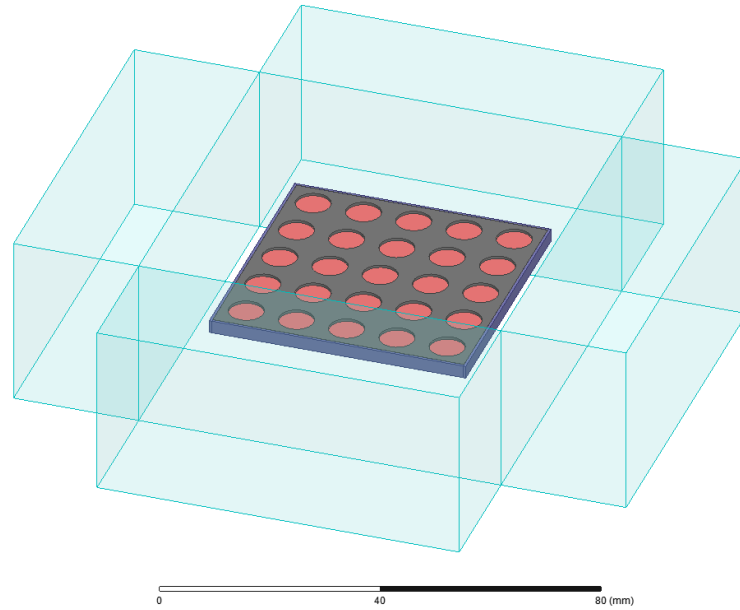


Figure 3.15. GMRF sensor model for finite simulation, additional boxes around main air-box represent the PML boundary conditions

In Figure 3.15, the final design of the sensor can be observed with the grating layer displayed in gray, the alumina underneath is observed through the circular apertures in a pink color and the reflective walls are shown in dark blue. Although the number of periods has been limited, the sensor still interacts with the incoming wave, and the reflective walls aid in improving the performance of the response. A discrete simulation was performed from 8 GHz to 12 GHz, using a step size of 0.005. The sensor shows a response in the reflection spectrum consistent to the results observed across the previously discussed simulations. A resonance peak was observed in the 10.19 GHz mark with an intensity of -15.89 dB. Overall, the response of the sensor had a minimal shift towards the upper limit of the frequency window. Additionally, the strength of the response reduced as the intensity increased from previous simulation. Besides the main resonance peak, a secondary peak appeared on the lower end of the frequency window, around the 8.2 GHz mark that wasn't observed in previous simulations. Finally, the general trend of the plot is shifted downwards from the 0 dB mark, meaning that the reflections have become weaker in this configuration. These changes are attributed to the removal of ideal conditions on the simulation parameters by defining the number of periods and, hence, the dimension of the sensor. Moreover, the additional distance between the edge of the air-box and the sensor contributed to the reduction in performance, particularly for the downward shift of the peak. This was due to the available space between the sensor and the air-box, allowing the wave to travel or diffract around the sensor, preventing it from returning to the source and, thus, not being captured by the receiver. The results can be observed in Figure 3.16.

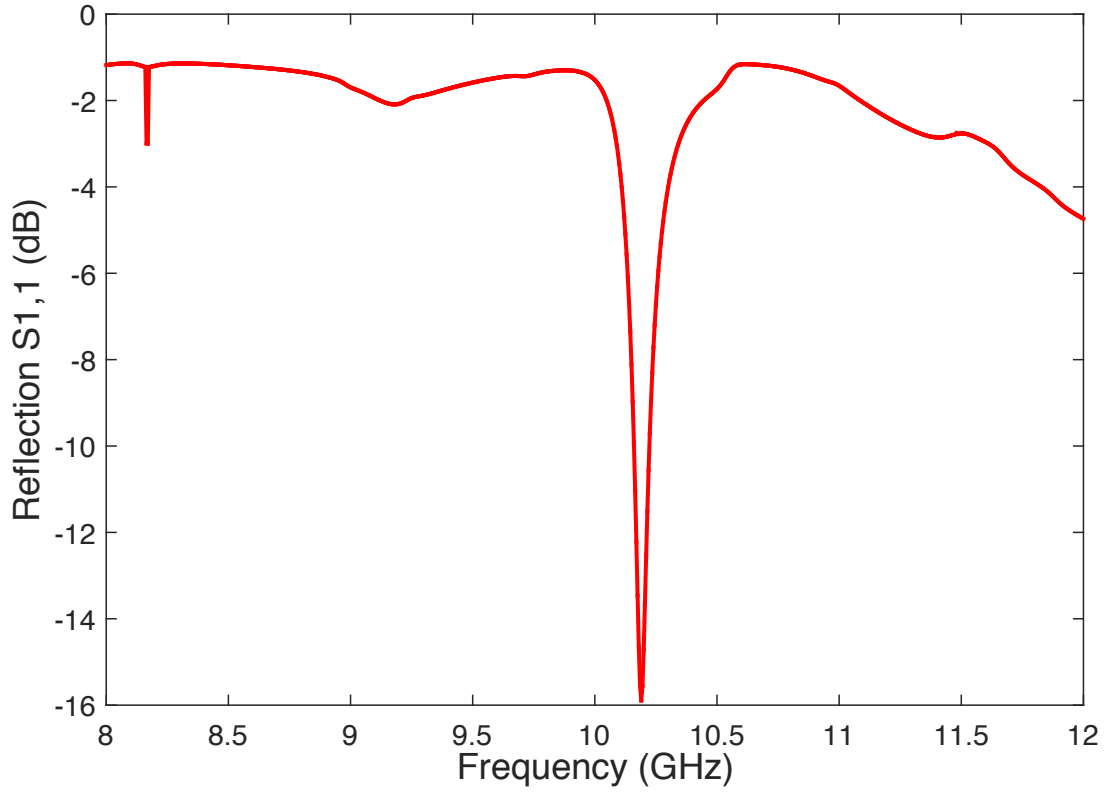


Figure 3.16. Reflection response of finite GMRF sensor, showing the traceable resonance peak around the 10.2 GHz mark

3.3 Metamaterial-based sensor

3.3.1 Concept and design

The developed metamaterial-based sensor is a continuation of Karim et al. research efforts [86]. After an extensive geometry optimization study, it was found that the closed-ring resonator (CRR) structure had the best transmission response and temperature sensitivity when compared to other common SRR structures found in nature. The unit cell of the proposed sensor is composed of a dielectric matrix with a pair of embedded CRRs. For the matrix, a dielectric ceramic was considered due to their resistance to high temperature conditions and as protection to the embedded rings. The unit cell can be modeled as an LC circuit, where the dielectric

ceramic acts a capacitor and the metallic rings provide an inductance. The design of the unit cell and the equivalent circuit model can be observed in Figure 3.17.

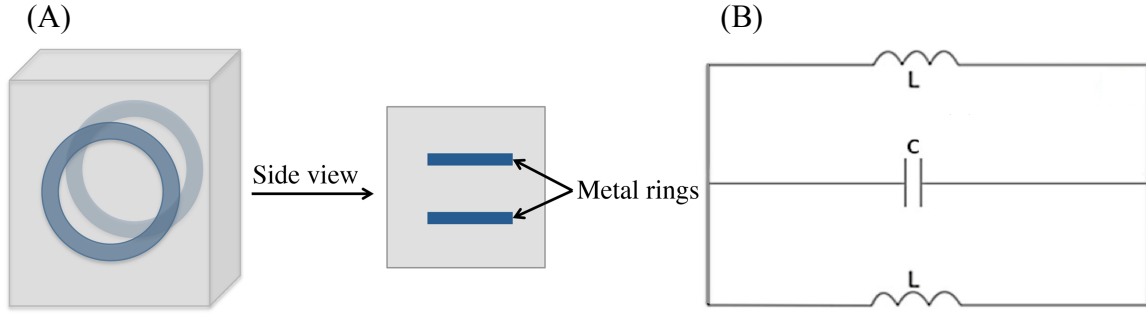


Figure 3.17. (A) Model of proposed sensor and (B) equivalent circuit model

The coupling of the capacitors and inductors in the system will result in a resonant behavior as denoted by Equation 3.3.

$$f_0 = \frac{1}{2\pi\sqrt{LC}} \quad (3.3)$$

Where f_0 represents the resonant frequency of the device, L is the inductance and C is the capacitance of the system. In Equation 3.4, the capacitance of the sensor can be determined by the parallel plate capacitor equation as shown below

$$C = \epsilon_o \epsilon_r \frac{A}{d} \quad (3.4)$$

Where ϵ_o is the relative permittivity of vacuum, ϵ_r is the relative permittivity of the dielectric material, A represents the area of the capacitors and d is the distance separating their plates. The temperature sensitivity of the device can be attributed to the behavior of the dielectric ceramic and represented in the capacitance equation. When the dielectric matrix undergoes a temperature change, its dielectric constant will change. This will affect the overall capacitance, and as a consequence, the resonant frequency of the system as observed in Equation 3.5

$$C(T) = \epsilon_o \epsilon_r(T) \frac{A}{d} \xrightarrow{\text{hence}} f_0(T) = \frac{1}{2\pi\sqrt{LC(T)}} \quad (3.5)$$

Prior to developing the simulation models and performing the necessary studies to evaluate the sensor's performance, the materials had to be selected for the sensor components. For the metallic rings, copper washers were selected for the simulations. For the dielectric substrate, previous studies were based on the use of barium titanate (BaTiO_3) [86]. However, barium titanate poses several challenges for this type of applications due to its properties; therefore, an alternative was found to serve as the dielectric ceramic component of the sensor. This process is explained in the following section.

3.3.2 Dielectric material evaluation and selection

Barium titanate can be employed in temperature sensing applications due to its dielectric constant being highly dependent on temperature changes. Moreover, its Curie temperature lies around 120°C , playing an important role in the relative permittivity value as more abrupt changes can be observed near this temperature and its dielectric constant achieves higher or lower values as it approaches or diverges from this temperature point, respectively [100]. The dielectric constant of barium titanate is also dependent on the frequency showing a decreasing trend with increasing frequency. Particularly, a significant drop is observed around the 2 GHz mark due to dielectric relaxation [101]. Nonetheless, BaTiO_3 still displays high values of dielectric constant for both the real and imaginary components, resulting in high values of the loss tangent as the field interacts with the material [102]. This can hinder the performance of the sensor by directly affecting the reflection and transmission spectra, as the energy exchange from the interrogation and the device is limited by the dissipation of the energy input into heat.

A second ceramic material was incorporated to the dielectric matrix in order to find a combination where the attractive properties of BaTiO_3 could be employed, while compensating for its deficiencies. The chosen ceramic was boron nitride (BN), which possesses a high melting point, a relatively constant dielectric permittivity as a function of temperature and most importantly a significantly low loss of 0.005 when measured at 17 GHz in a temperature range from 23°C to 600°C [103]. In order to achieve optimal properties, a combination of 70% BN

with 30% BaTiO₃ in weight was employed. In order to quantify the contribution of each ceramic to the effective dielectric constant, the Bruggerman method was employed [104]. This method assumes that for any block of material, the dielectric constant will be of the main material. The Bruggerman method is described as follows [105]:

$$f \frac{\varepsilon_{r1} - \varepsilon_B}{\varepsilon_{r1} + 2\varepsilon_B} + (1 - f) \frac{\varepsilon_{r2} - \varepsilon_B}{\varepsilon_{r2} + 2\varepsilon_B} \quad (3.6)$$

Where ε_{r1} represents the dielectric constant of the main material, in this case BN; ε_{r2} is the dielectric constant of the secondary material (BaTiO₃), ε_B is the effective dielectric constant of the mixture and f is for the fill fraction of the host material. The Bruggerman method can be solved by employing Equations 3.7 – 3.9 [105].

$$\varepsilon_B = \frac{-B + \sqrt{B^2 - 4AC}}{2A} \quad (3.7)$$

$$B = (\varepsilon_{r1} - 2\varepsilon_{r2}) + 3f(\varepsilon_{r2} - \varepsilon_{r1}) \quad (3.8)$$

$$C = -\varepsilon_{r1}\varepsilon_{r2} \text{ and } A = 2 \quad (3.9)$$

The dielectric constant of the host (BN) and infiltrated (BaTiO₃) materials were considered to be 4 and 124.71, respectively. Additionally, the fill fraction was considered to be 0.7. The effective dielectric constant of the mixture was found to be 13.9 and was employed in the developed models.

3.3.3 Unit cell simulation

A similar approach to the GMRF sensor was taken for the design and performance evaluation. A 3-D model of the unit cell was developed in HFSS replicating the intended design for the metamaterial sensor. Copper washers were employed as the metallic rings due their commercial availability; for this material, the properties presented in the software's database were employed. As for the dielectric ceramic, a custom material emulating the ceramic mixture

was employed with the effective dielectric constant calculated. The modeled unit cell has a side length of 10.16 mm, a thickness of 3.175 mm. Additionally, the inner and outer radii of the CRR are 1.6 mm and 3.5 mm, respectively as obtained from commercially available washers. After the model was developed, an air box with a height of around $\lambda/2$ was added for the traveling wave. The unit cell simulation aimed to replicate an ideal case of an infinitely periodic structure; therefore master/slave PBCs were implemented on the sides of the unit cell, located on the x-z and y-z planes and covering the whole air box. For the excitation, Floquet ports were employed due to the use of the PBCs on all vertical planes. The model of the unit cell can be observed in Figure 3.18.

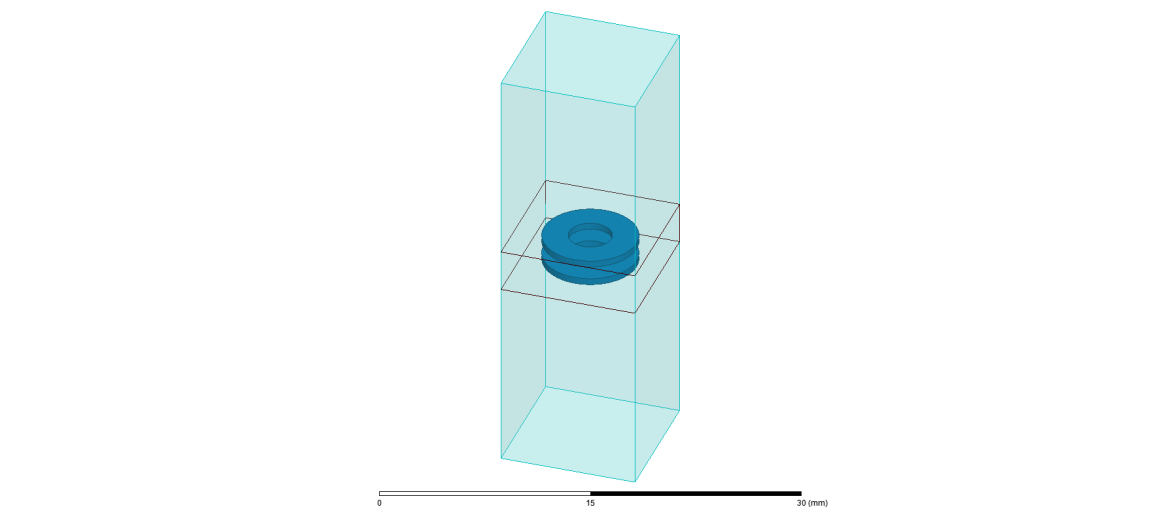


Figure 3.18. Unit cell of metamaterial sensor

The simulation was performed for a frequency range from 6 to 18 GHz in order to characterize the performance of the sensor in a wide frequency window. A discrete simulation with a step size of 0.01 GHz was performed. For this sensor design, both the reflection ($S_{1,1}$) and transmission ($S_{2,1}$) were recorded. The latter was not possible for the guided mode resonance filter sensor design proposed due to the presence of the solid metal plate on the bottom of the design. The results of the unit cell simulation for the reflection and transmission spectra can be observed in Figure 3.19 (A) and (B), respectively.

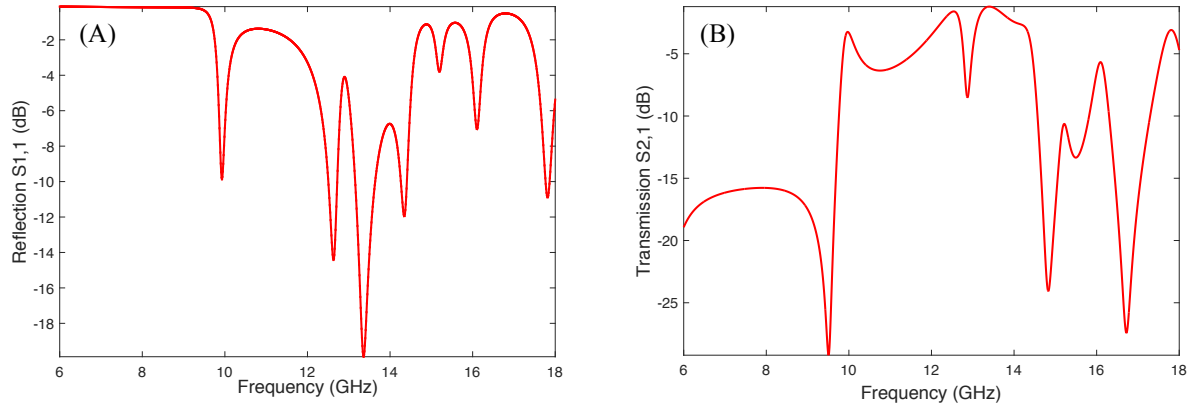


Figure 3.19. (A) Reflection and (B) transmission results for the evaluated metamaterial sensor

The metamaterial sensor shows interaction with the incoming wave in both the reflected and transmitted spectra. For the reflection spectrum, a stop-band can be observed in the lower end of the frequency window. After this, several peaks can be observed with the first one being close to the 10 GHz mark, with an intensity of -9.741 dB. Additionally, the deepest peak at can be observed at the 13.35 GHz mark with an intensity of -19.82 dB. Any of these peaks can be traced for temperature monitoring, as the response would shift with the variation of temperature. As for the transmission spectra, a similar behavior is shown in the S-parameters. The response for the transmission is stronger overall. Three main peaks can be observed in the 9.5 GHz, 14.84 GHz and 16.72 GHz marks. The intensity values of these peaks are -29.12 dB, -24 dB and -27.43 dB, respectively. Again, any of these three peaks can be translated to a temperature reading due to the variation of the response with the change of temperature. Due to the use of the dielectric substrate and as observed by unit cell results, this type of sensor can be employed for both reflection and transmission interrogations. However, these results are for idealized conditions and the response of the sensor can change as dimensional constraints are applied to the model.

3.3.4 1-D periodicity simulations

In order to achieve a practical design, dimensional constrains had to be applied to the sensor model. The first step was to limit the amount of periods employed for the sensor.

However, the reduction of periods can result in a degradation of performance. This step took into consideration the limitations of the fabrication equipment available for the development of the sensor. Therefore, the amount of rings in the model was limited to 5 in the y-direction for the initial simulation. The extension of the sensor in the x-direction was still left infinite to evaluate the effect of the constraints applied. For this model, the same steps as for the 1-D GMR sensor simulations were followed. The air-box was extended $\lambda/4$ on the finite sides of the model. A plane wave excitation running in the negative z-direction was employed. PMLs were employed on the finite sides to truncate the simulation space to the air-box. Additionally, 2-D sheets were added outside the PMLs and were assigned as master/slave boundary conditions to repeat the sensor design along the y-z plane. In order, to capture the response from the sensor, an extra set of PMLs were added on the top and bottom boundaries of the air-box. The model is presented in Figure 3.20.

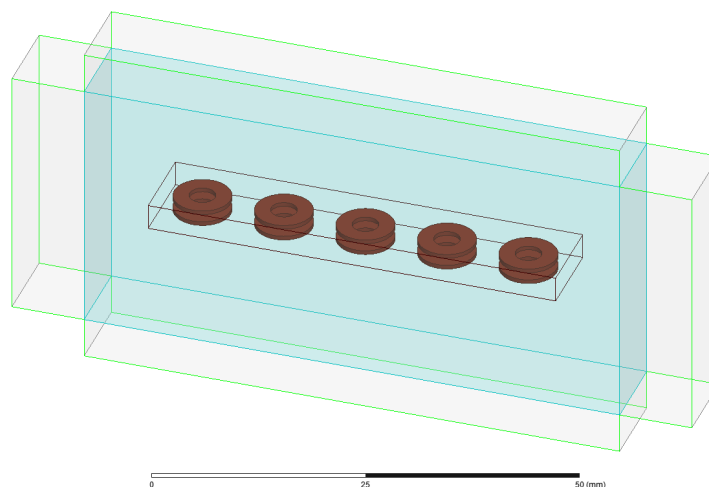


Figure 3.20. 1-D model of the metamaterial temperature sensor

The developed model displayed a side length of 50.85 mm and was simulated for a frequency range from 6 to 18 GHz to maintain consistency with previous simulations and also to see the variation of the whole spectra. The results are shown below.

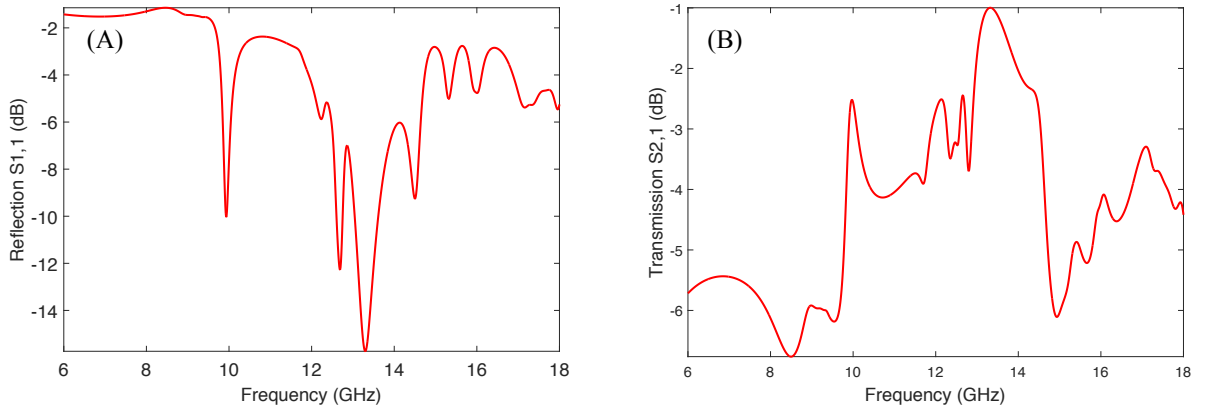


Figure 3.21. (A) Reflection and (B) transmission results for 1-D periodicity model of metamaterial sensor

From these results, it can be observed that the behavior is similar to that of the infinite unit cell for the reflection spectra. However, the intensity decreased overall for the response. The first peak observed is at the 9.92 GHz with an intensity value of -9.875 dB, while the most prominent is at 13.3 GHz with intensity of -15.73 dB. The transmission spectrum was severely affected by the limitation of the periods. The intensity values shifted from around -28 dB to -6.5 dB and the peaks lost definition. It can be assumed that limiting the periodicity of the sensor can be detrimental to the performance, particularly to the transmission spectra. A simulation of the “block” of material, which replicates a possible fabricated sample is explained below.

3.3.5 Finite block simulation

The performance evaluation of a 50.8 x 50.8 mm array of the periodic unit cell was evaluated. This simulation is derived from the samples that can be fabricated with the equipment available. For this simulation, the periodicity was also limited along the x-direction. This resulted in a finite array of CRRs inside of the ceramic mixture with tuned properties. For this simulation, the air-box was expanded to cover the new model. The CRRs were evenly spaced inside of the dielectric ceramic resulting in 50 resonators employed for the structure. Additionally, a spacing of $\lambda/4$ was included between the edge of the model and the air box as

PMLs were added to truncate the computations on the outer boundary of the air-box. For this simulation, a waveport excitation was employed, located on the outside boundaries of the x-y planes of the air-box. The developed model for this simulation is presented in Figure 3.22.

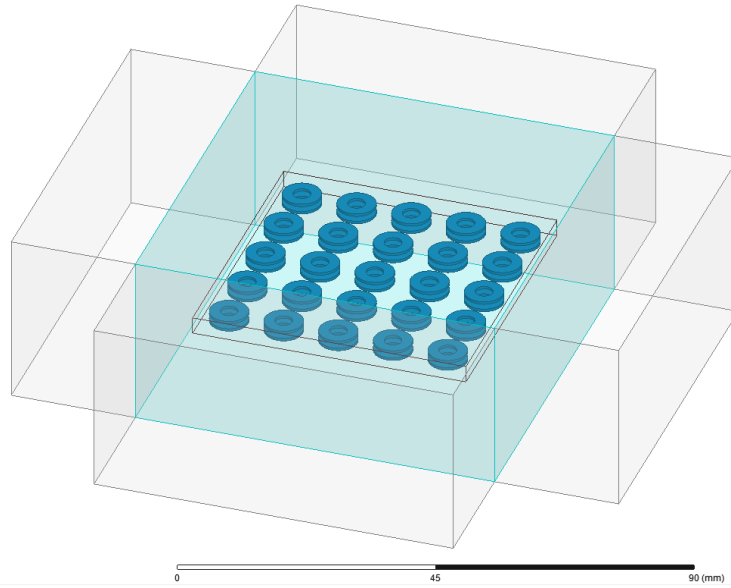


Figure 3.22. Model for sensor block employing 25 pairs of CRRs

These simulations were performed for a frequency range of 6 to 18 GHz in order to track the changes on the performance across this frequency window. Significant changes were observed for the reflection response. Better-defined peaks were found around the 10 GHz and 13 GHz marks, which were present in previous results but had less definition. However, for the transmission spectrum, the results continued previous trends, as the transmitted response for all of the wavelengths is virtually non-existent. These results can be observed Figure 3.23 (A) and (B) for the reflection and transmission results, respectively.

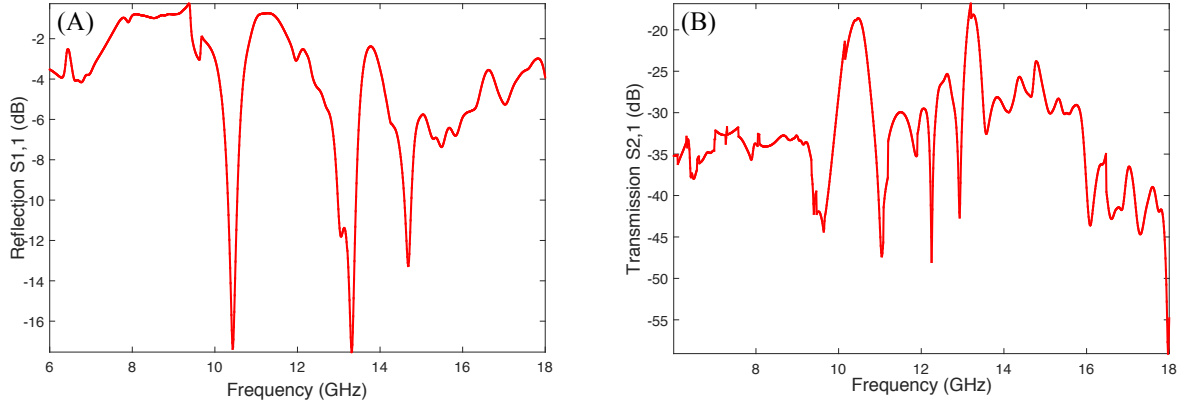


Figure 3.23. (A) Reflection and (B) transmission response of finite block sensor

In these results, the transmission response has disappeared as the trend consistently lies around the -35 to -45 dB range. This can be interpreted as the majority of the wave being reflected or dissipated instead of transmitted. Therefore, the resonance peaks previously found in the infinitely periodic structure for the transmission spectra have disappeared. However, the reflection response has become more defined and at this point, it can be traced for temperature readings. The first peak observed shifted from 9.95 GHz in the unit cell simulation to 10.42 GHz; the new intensity value observed is of -17.07 dB. The second visible peak was found at 13.31 GHz with an intensity of -17.53 dB. Finally, a simulation encompassing 4, electromagnetically coupled, blocks of the developed sensor were simulated to explore the possibility of covering a larger area by combining multiple samples.

3.3.6 4-block simulation

For this simulation, the same boundary conditions as for the previous section were employed. A model was developed for the 4 blocks arranged in a square array resulting in sensor that expands with the double the size of the previously discussed finite sensor, while maintaining its thickness constant. This model resulted in the use of 200 CRRs for the structure. The boundary conditions, excitations and simulation settings were left consistent as the previous simulation. The model can be observed in Figure 3.24.

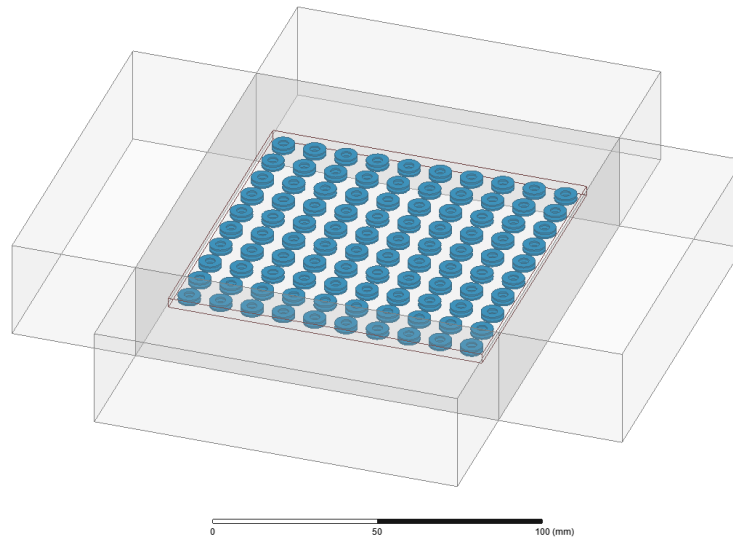


Figure 3.24. Model of 4-block metamaterial sensor showing the PML boundary conditions

With this configuration, the response of the sensor achieved good reflection response with several peaks, with the main peak showing an intensity of -12.2 dB. Using this type of interrogation, any of the peaks could be used for temperature monitoring as they depend on the dielectric constant shift of the ceramic. Ultimately, the best peak to use for sensing is the one located in the 13.23 GHz mark as it is the best defined and deepest one when compared to the rest of the trace. For transmission, the response has improved due to the increase on the period number. The trend has shifted upward with the maximum value being -3 dB. This suggests that the resonance peaks are present in the response of the sensor and can be used for temperature monitoring. At this point, the transmission spectrum has shown deeper peaks than the reflection trend. The transmission response has a prominent peak in the 16.08 GHz mark with a depth of -28.89 dB. However, it is not certain if these constitute resonance peaks as the transmission spectra vary rapidly with the change of frequency. Moreover, these changes are not well defined when compared to literature. However, the reflection response has shown promising response in a wide frequency window including the X and Ku bands, which are commonly used for testing. These results can be observed in Figure 3.25.

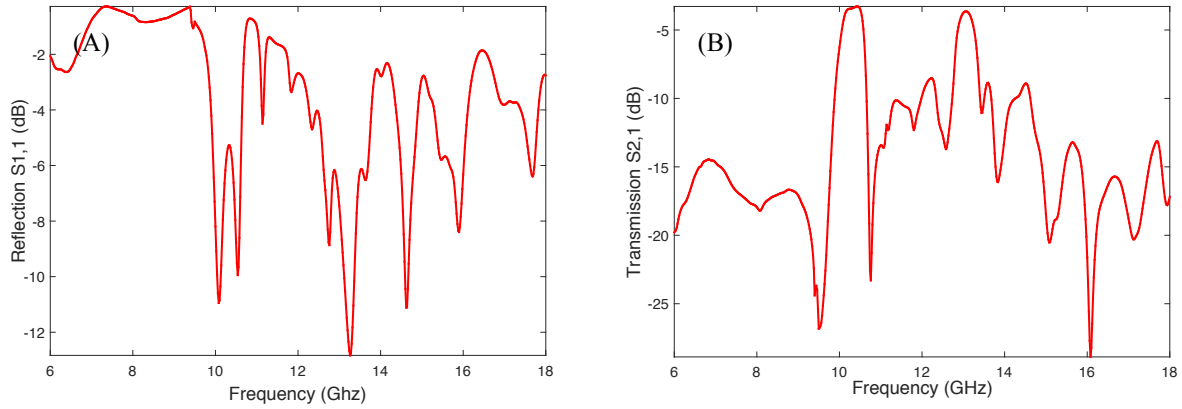


Figure 3.25. (A) Reflection and (B) transmission spectra of the designed 4-block metamaterial sensor

3.4 Conclusion

The design, modeling and optimization processes of two wireless temperature-sensing devices were discussed in this chapter. For the first one, a tri-layer guided mode resonance filter sensor with metallic cladding and a dielectric ceramic was proposed. The justification of the use of metallic screens is for better confinement of the fields and a more robust performance, as the sensor is potentially less sensitive to outside combustion byproducts. A design frequency of 10 GHz was selected in order to be compatible with the X-band frequency window. The modeling stages were detailed, which encompassed the simulation of the unit cell and dimension optimization, limiting the period number, use of reflectors and the finite sensor simulations. Ultimately, a design with a side length of 49.575 mm and a thickness of 2.54 mm was developed; it achieved a reflection response of 10.19 GHz and an intensity of -15.89 dB. For the metamaterial sensor, the sensor design is based on previously developed work. A similar approach was employed by starting the design with the unit cell, moving on the number of periods and the finite sensor simulation. The unit cell showed promising results for the reflection and transmission spectra. However, the periodicity had an effect on the results, particularly for the transmission spectra. As the periods were limited, the trace of both responses lost definition and the peaks were reduced. The final sensor design consists of a mixture of two different

ceramics and 200 CRRs composed of copper were employed. The design consisted of a side length of 101.6 mm and a thickness of 3.175 mm. The results for the metamaterial sensor simulation show several peaks for both the reflection and transmission spectra. The main peaks are located in the 13.23 GHz mark with an intensity of 12.2 dB for the former, while a prominent peak was found in the 16.08 GHz with an intensity of -28.29 dB for the latter. Next, the fabrication of both of the sensor designs using traditional fabrication and powder compression methods for the GMRF and metamaterial sensors is discussed.

Chapter 4: Fabrication

4.1 Introduction

Sensor fabrication was performed with the goal of achieving affordable and robust sensor units. For the GMR sensor, commercially available materials and different fabrication techniques such as water jet cutting and traditional machining were employed. Sensors were designed using SolidWorks software package and then the appropriate technique for the material was utilized. For the metamaterial sensor, traditional powder compression methods and commercially available metallic washers were employed. Additionally, a binder was synthesized in order to ensure the structural rigidity of the samples. The fabrication process is discussed in the following sections.

4.2 Guided mode resonance sensor

4.2.1 Water jet cutting based samples

The first approach to the fabrication of GMR sensor units was to follow the materials employed for the simulation and develop a physical sample based on them. For the simulation, 0.508 mm thick titanium plates were used for the metallic screens while 99.6% pure alumina was employed for the dielectric ceramic. Since the materials were kept constant, commercially available titanium plates (Online Metals) with a thickness of 0.508 mm were used. Additionally, nonporous high-purity alumina slabs (McMaster-Carr) with a thickness of 1.524 mm were employed. The sensor was fabricated following the 5x5 period array simulated. Since both the commercially available alumina and titanium sheets were bigger in size, the appropriate tools needed to be used to cut them to match the simulation design. For the alumina ceramic, a diamond cut-off wheel was employed due to its brittleness to achieve 50.8 x 50.8 mm square samples. The titanium sheet's properties represented a challenge for the machining of the sample. Therefore, traditional machining could not be employed. As an alternative, water-jet cutting was performed for the dimensioning and cutting of the periodic pattern on the titanium sheets. A CAD was developed and the water jet cutting was outsourced to Aarmor Metals (El

Paso, TX.). The titanium sheets were cut into 50.8 x 50.8 mm squares for the top and bottom plates. Additionally, sidewall reflectors were also cut for each sample with the dimensions of 50.8 mm in width with and 2.54 mm in height. The parts were assembled and bonded with high temperature alumina paste (Cotronics) for high temperature testing. Additional samples were glued together with super glue for room temperature testing. Examples of these fabricated samples can be observed in Figure 4.1.

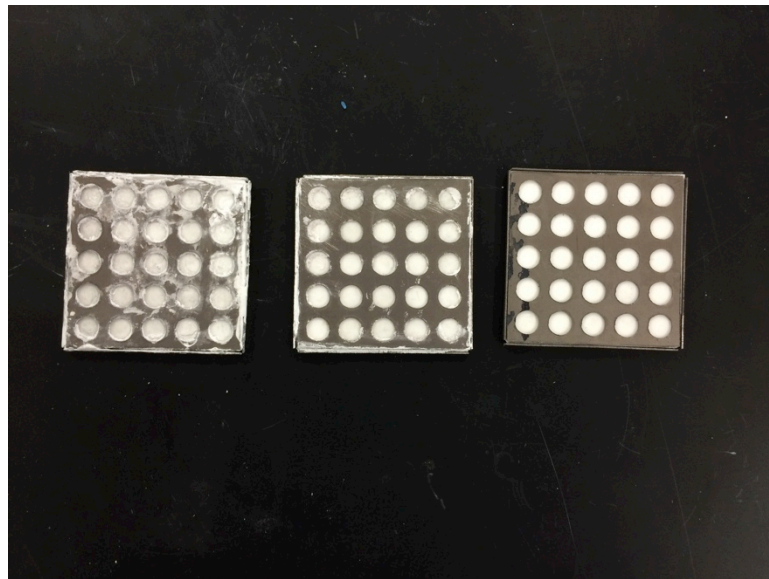


Figure 4.1. Fabricated samples, from left to right: first and second ones are bonded with alumina paste and third one is bonded using Superglue

After visual examination, it was observed that the cutting was not precise. The top and bottom layers had slight variations in dimensions per sample. Additionally, the circular apertures were found to be irregular in their circumference, varying with each hole and ultimately with each sample. The bonding employed was also found to have its drawbacks. On one hand, Superglue can only be employed for low temperature applications and will result in layer separation if heated above its melting point. On the other hand, the high temperature alumina paste resulted in complications with bonding due to fast drying of the paste; moreover, the alumina paste was found to leave varying amounts of residue depending on the way it was

applied. For comparison, a close-up of a sensor bonded with alumina paste is shown in Figure 4.2 (A) and one with Superglue is shown in Figure 4.2 (B).

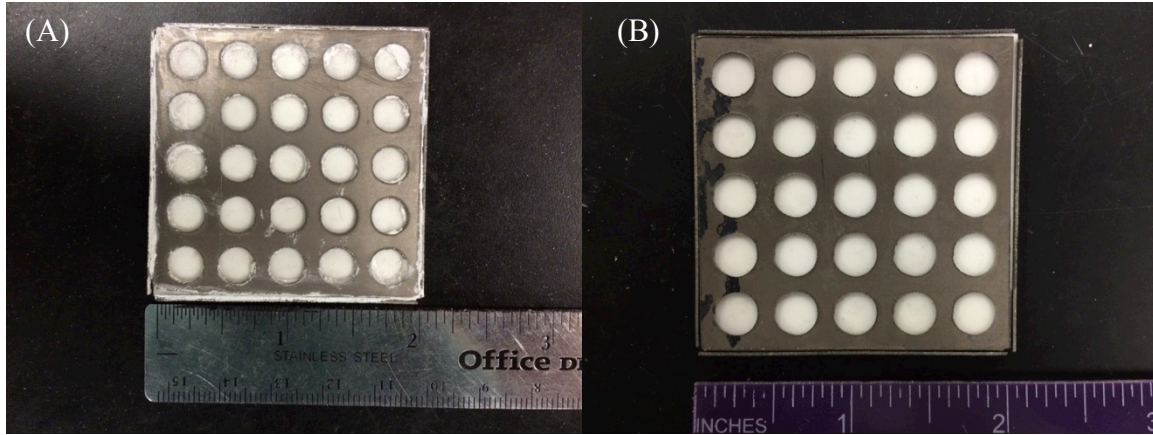


Figure 4.2. Water jet cutting based samples bonded with (A) alumina paste and (B) Superglue

Initially, these samples were developed to be tested within a free space measurement facility with a set of Gaussian beam antennas, which can detect such sample size. However, the available antennas were not optimized for reflection measurements, thus alternative fabrication and testing methods were explored. X-band horn antennas were considered for the testing. However, the sample size is insufficient for these measurements. These challenges and the hardness of the metal resulted in the use of alternative materials and fabrication methods to achieve robust and usable GMRF sensors.

4.2.2 Traditional machining based samples

An alternative fabrication method employing different materials was used to achieve samples which were larger in size and thus, detectable at the X-band frequency range. For this fabrication, aluminum and steel plates were considered to fabricate the bottom encasing with implemented reflectors. Additionally, the top plate was fabricated using thin aluminum and steel plates. Commercially available alumina slabs were employed for the dielectric ceramic with dimensions of 114 by 114 mm. These dimensions dictated the size of the cavity machined on the bottom plate. The bottom plate was initially cut into a 127x127 mm square for the fabrication.

The thickness of the bottom plate was of 7 mm. After that, it was mounted into the vice of the milling machine and a drill bit with a diameter of 1/2-inch was employed to make several center holes with a depth of 0.06 inches to machine the cavity. A 1/2-inch cutter was employed to gradually remove material in order to achieve the housing of the sensor. For the top plate, thin aluminum or steel plates were used, depending on the fabricated sample. Due to the thinness of the plates, a machining challenge was encountered when securing them in the grip and drilling the holes through them. Therefore, a supporting plate was employed. A 1-inch thick Plexiglas plate was employed to provide structural support to the metallic thin plate for machining. To mount it, the plates were bonded using bolts and nuts through previously drilled holes. The Plexiglas plate was gripped to the milling machine to achieve the metallic grating needed. A drill bit of 17/64 inches was employed to fabricate the grating on the thin metal sheet. This drill bit size was employed as it represented the closest size available to the circle diameter used in the simulation. After the periodic pattern was machined into the grating layer, it was cut to match the dimensions of the sensor housing. The sensor was bonded together with Superglue for room temperature testing.

This fabrication method resulted in bigger and thicker samples than those achieved by water jet cutting. The bigger sample size is considered an advantage and a desired outcome for testing. Moreover, samples fabricated through this technique presented deformations on both the top and bottom plates due to the stress caused by the vice on the former and the force applied by the drill bit/cutter on both the samples. For the bottom plate, an inward bent was observed in the aluminum sample. This bending was minimal on the steel sensor housing. Due to the thinness of steel and aluminum top plates, warping was observed in both samples. This was a consequence of the sample only being attached to the Plexiglas on the edges and the force applied when the drill bit cut through the material. Another important thing to consider was the difference between simulated and fabricated hole sizes. Additionally, other fabrication errors to consider are the human error introduced in machining and the warping of the top plates. The first one was observed on the 2-D grating; some of the circular apertures deviated from a straight

line in both the x and y axes. This is due to small divergence from the set values on the mill machine during fabrication. The second one was observed after assembling the sensor. Due to the warping, an air gap was observed between the dielectric layer and the metallic grating. Samples fabricated through this method can be observed in Figure 4.3.

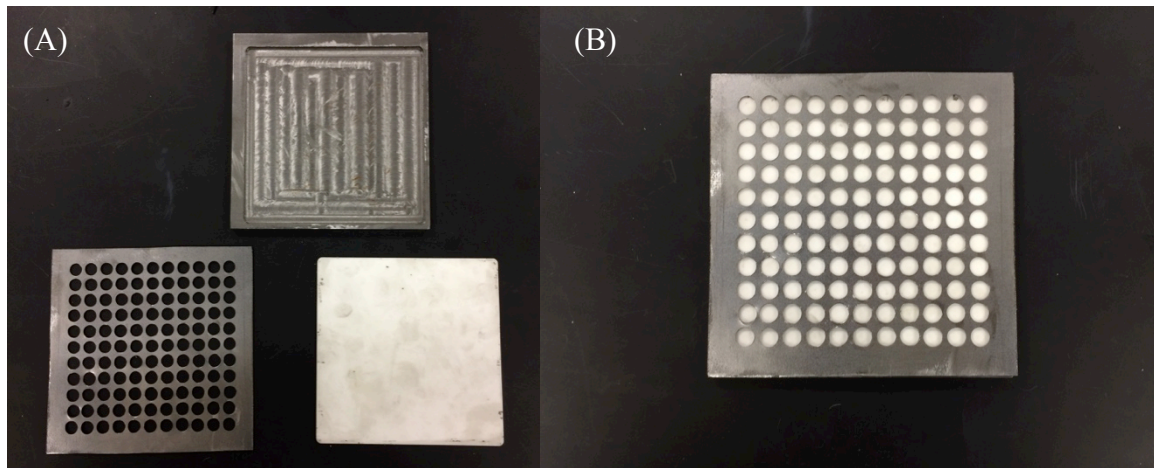


Figure 4.3. Sample fabricated through traditional machining methods displaying (A) different components and (B) assembled sensor

4.3 Metamaterial sensor fabrication

4.3.1 Binder synthesis

Polyvinyl alcohol (PVA, Sigma Aldrich, 99.6% hydrolyzed) was gradually mixed with DI water in a 1:10 ratio in a 250 mL beaker while mixing under heavy stirring (600 rpm). After the addition of PVA was complete, the mixture was left under heavy stirring for 20 minutes. The sample was then heated to 90°C until all of the powders were completely dissolved in the water, yielding a transparent, viscous liquid with a yellowish tint. This experimental procedure is depicted in Figure 4.4.

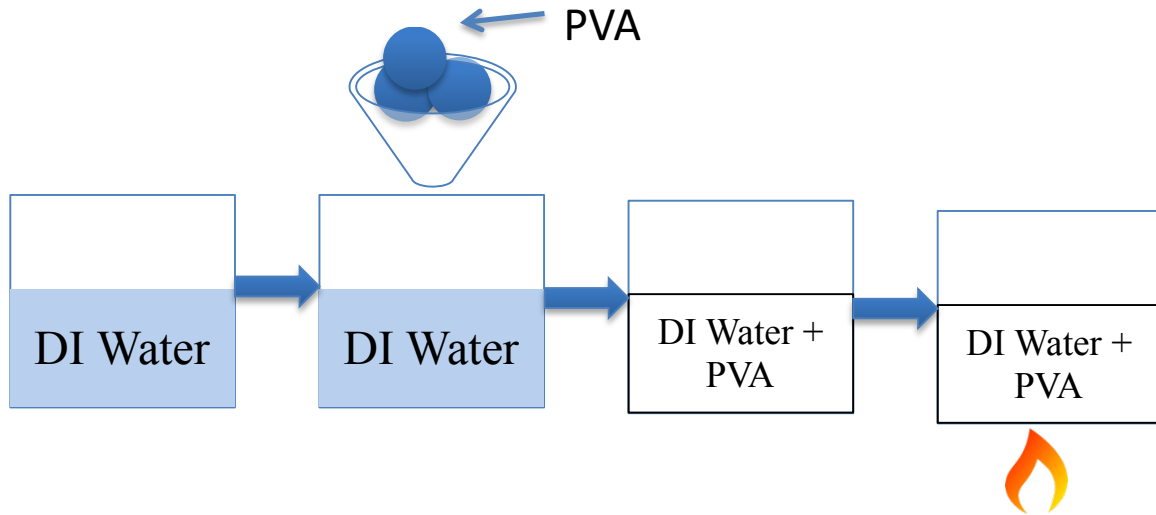


Figure 4.4. Experimental procedure for PVA binder synthesis

4.3.2 Traditional powder compression method

Metamaterial sensors were fabricated using traditional powder compression methodology. In order to follow the sensor design developed in the simulation section, commercially available materials were employed for the simulation. For the dielectric ceramic, barium titanate (BaTiO_3 , BTO – Advanced Materials) with an average particle size of 700 nm and boron nitride (BN – US Research Nanomaterials, Inc.) with an average particle size of 800 nm were employed. For the CRR structures, copper washers (McMaster-Carr) with 3.5 mm in outer diameter, 1.6 mm in inner diameter, 0.005 mm in thickness were used. For the fabrication, 8.161 grams of BTO nanopowders were mixed with 1.597 grams (7.5% wt. of the total mass) of PVA and ground in a mortar until a uniform mixture was achieved. After this, 13.135 grams of BN powder were added to the mortar and ground until an even distribution of the ceramics was attained. A 50.8x50.8 mm square die was used to fabricate the samples. A layer of the mixture, composed of one third of the mass, was added to the die and distributed uniformly by hand, using the piston of the die assembly. On top of this layer, 25 copper washers were evenly arranged to form the CRR array. A second ceramic layer, employing one third of the total mass, was added and 25 copper washers were placed on top of them. A final layer of dielectric ceramic was added inside of the die. This process is depicted in Figure 4.5.



Figure 4.5. Schematic for metamaterial sensor fabrication

Then, the powder/washer structure was compressed using 3 metric tons using a CARVER hydraulic press for five minutes. The pellet was then retrieved. No post processing was performed. The fabricated samples had a side length of 50.8 mm and a thickness of 3.17 mm. The attained samples showed good structural rigidity through the fabrication process aforementioned. Additionally, good finishing was observed and the samples showed no significant amount of loose powders. Four samples were fabricated following this fabrication method with the intention of assembling them together and covering more area for sensor interrogation. These samples can be observed in Figure 4.6 (A) and (B).

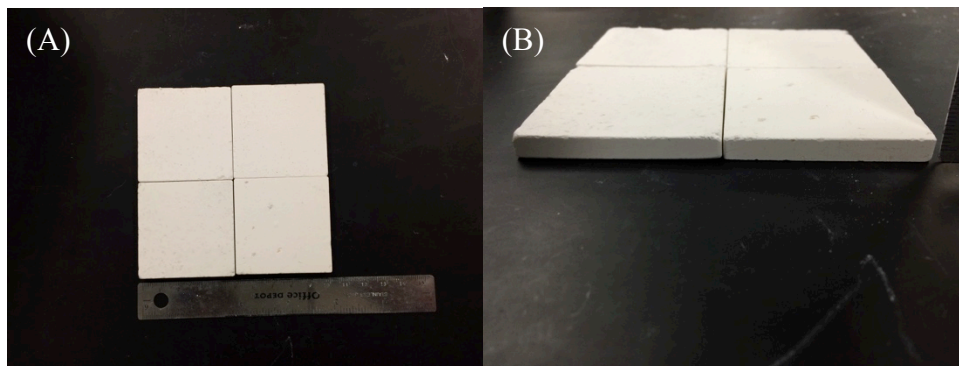


Figure 4.6. (A) Top view and (B) side view of an array of 2x2 metamaterial samples

4.4 Conclusion

The fabrication methods for the GMRF and metamaterial sensors were detailed in this chapter. For the guided mode resonance filter, two different fabrication methods were employed. The first one employed titanium screens and water jet cutting technology due to the metal's properties and was outsourced. This fabrication method resulted in 50.8 x 50.8 mm screens with a thickness of 0.508 mm. Alumina ceramic was sandwiched between the grating and bottom plates and sensors with a width of 50.8 mm and a thickness of 2.54 mm were achieved. After fabrication, it was observed that the titanium screens were not evenly cut and the circular aperture's circumference was not even. Due to complications with the testing setup, alternative fabrication methods had to be explored. Traditional machining methods employing steel and aluminum for the sensor encasing were used. Sensors fabricated with this methodology had a side length of 127 mm and a thickness of 7 mm. Samples fabricated through traditional machining methods showed visible misalignment in the grating pattern and warping of the metallic plates. After assembly, an air gap between the dielectric and the top plate was present due to the plate's warping. These can be detrimental to the performance of the sensor due to the presence of rapid change in refractive index as well as the misalignment affecting the periodicity. For the metamaterial fabrication, powder compression methodologies were employed. BTO and BN nanopowders were mixed with previously synthesized PVA binder. Then, the mixture was placed in a die in 3 separate layers with copper washers in between them. After compression, the samples showed good rigidity and structural integrity. No post-processing was performed on these samples.

Chapter 5: Testing and Results

5.1 Introduction

Room temperature free space measurements were done in order to characterize the performance of the sensor in the reflection or transmission spectra. The testing setups consisted on a programmable network analyzer (PNA – Agilent technologies), a pair of co-axial cables and a set of antennas. For the antennas, different alternatives such as X-band horn antennas and Gaussian beam antennas were employed for the FSS and metamaterial samples, respectively. Tests were conducted in an anechoic chamber in the EM Laboratory facilities for the former and at the Center for Space Exploration Technology Research (cSETR) - Challenger-Columbia Structures and Materials Research facility for the latter. Both facilities are located at The University of Texas at El Paso (UTEP). The anechoic chamber was used as the noise generated from diffractions and unwanted reflections is absorbed by the chamber. The results obtained for these sensors are discussed in the following sections.

5.2 Free space measurements of guided mode resonance filter sensor

The modeled GMRF sensors have shown a resonance peak around the 10 GHz mark in the reflection spectra ($S_{1,1}$). Therefore, horn antennas (Pasternack) with a working frequency of 8.2 to 12.4 GHz were employed for this free space measurement. For this testing, E-calibration was performed on the ports of the PNA to account for correctable measurement errors. After that, the antennas were connected to the PNA through flexible co-axial cables and were placed by facing each other inside of the anechoic chamber for calibration purposes. A sample with a known response was placed between the antennas to test the performed calibration. To account for the gain of the antenna, additional correction methods were performed on the PNA. The GMRF sensor was then placed in front of the interrogating antenna and the response was measured. Figure 5.1 (A) – (D) portrays the testing methods and placement for the aluminum and steel samples, respectively.

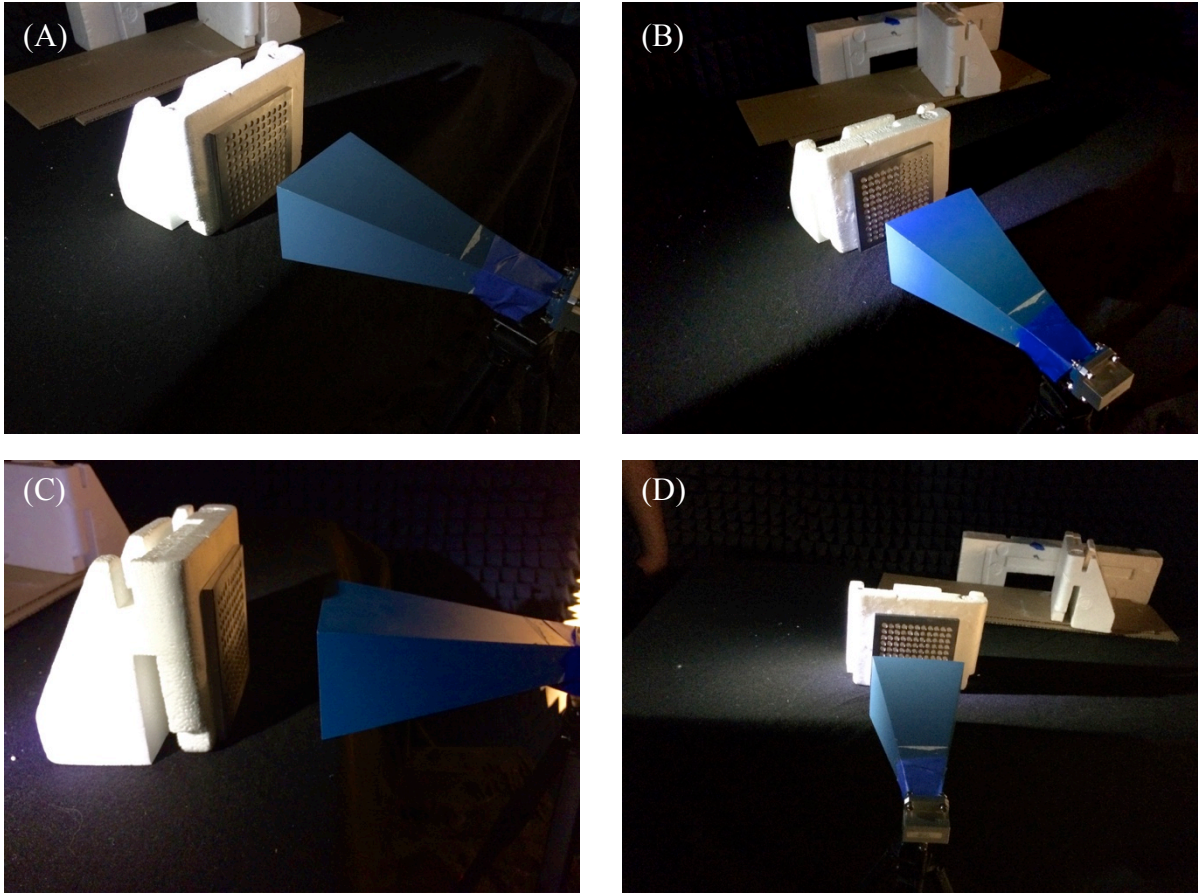


Figure 5.1. Close-up of free space measurements for (A) aluminum and (B) steel samples; additionally the (C) and (D) images represent the side view and front view of the testing setup

Due to the properties of the GMRF and the nature of the testing mechanism, antenna-sensor alignment is very important to ensure reliable results. Samples were empirically aligned to the antenna in order to dismiss possible performance errors due to this factor. The sample was supported by a Styrofoam structure, which is transparent to the electromagnetic waves and placed about 5 inches away from the interrogating antenna. Two rounds of testing were performed on different dates in order to observe variations in the results. The results for the measurements of the GMRF sensors can be observed in Figure 5.2 (A) and (B) for the first tests and (C) and (D) for the second test.

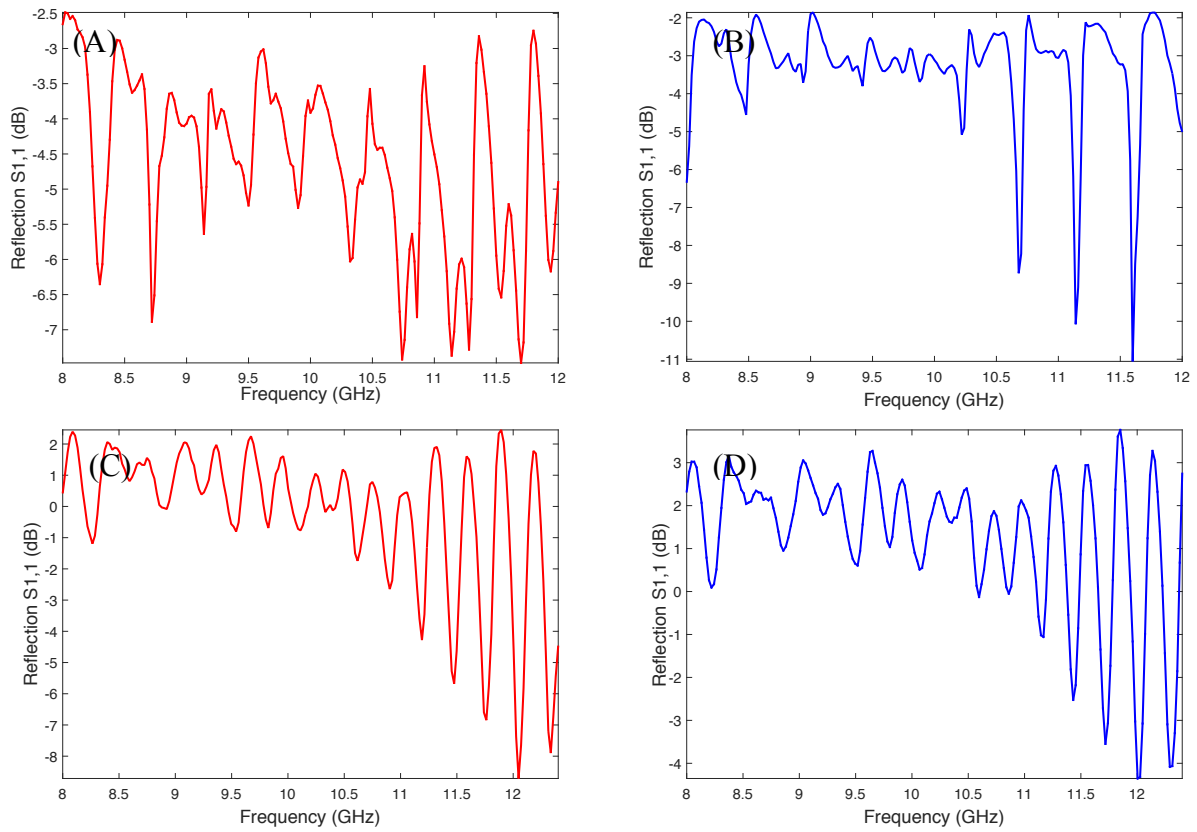


Figure 5.2. Reflection results for the aluminum (red) and steel (blue) GMRF sensors; (A) and (B) represent test 1 and (C) and (D) display test 2

No resonance peak was observed in any of the samples for any of the tests performed as observed from the results above. For the results portrayed in Figure 5.2 (A) and (B) a rapid variation on the intensity of the reflection spectrum is depicted by the results, which could be confused with a resonance peak; however, due to the rapid intensity variation and the repeated pattern of the trend, this was discarded as a measurement error. On the steel sample results, three prominent peaks are observed on the higher end of the frequency window. However, these were also discarded as measurement errors due to their close proximity to each other and their absence on the second test performed. For the second set of results, which are shown in (C) and (D), a similar behavior was observed with rapid variation of the energy suggesting that no interaction existed between the GRMF and the incoming wave for both the aluminum and steel samples.

Although the exact same dimensions could not be achieved, a sensor response was expected due to the similarities between the model and the fabricated samples. The combined effects of the small variations from the model, which were discussed in the fabrication chapter, could lead to a significant shifting from the design response. Upon further examination, the most prominent fabrication flaw is the warping of the plates after the mill-machining step. This warping resulted in sections of the sensor where the grating and the dielectric slab were not in close proximity. This separation introduces an extra “layer” of air between the diffraction grating and the slab waveguide. This translates directly into a disturbance of the phase due to the variation of the refractive index inside of the encasing since air and alumina are at close proximity. Moreover, this small but significant air gap, could result in a decoupling of the elements and total internal reflections not being achieved inside of the waveguide structure for the diffracted modes resulting in evanescent fields. The presence of this air gap at random positions in the structure causes a detrimental effect on the periodicity of the sensor and potentially contributes to the absence of a resonance peak in the reflection spectrum. A close-up of the mentioned air-gap aforementioned is shown in Figure 5.3. A model exploring the effect of the air gap for the 3-D sensor is discussed in Appendix A.

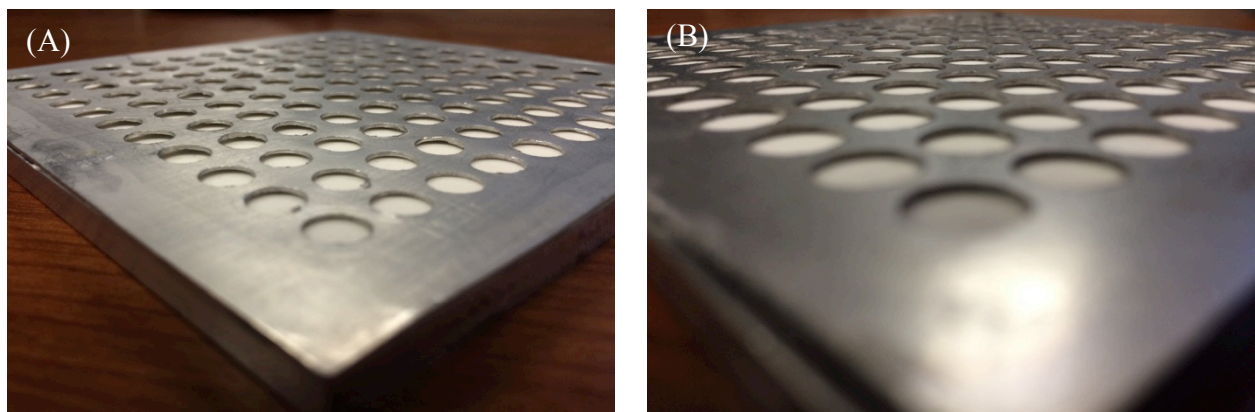


Figure 5.3. Close-up view on the top layer separation of the (A) aluminum and (B) steel samples

5.3 Free space measurements of metamaterial sensor

The testing of the metamaterial sensor was performed in the cSETR - Challenger-Columbia Structures and Materials Research Facility.. The setup consisted on a pair of Gaussian beam antennas (MWI Laboratories) were connected to the VNA through a pair of co-axial cables. This setup is capable of performing free space measurements for a frequency range of 7 – 16 GHz. For these measurements, an unguided calibration was performed to correct potential measurement errors. The calibration consisted on performing an “open” sweep to account for the testing setup without adding any additional interfering elements between the antennas. For these tests, the transmission spectrum was of interest as the peaks were present on the 4 block simulation results. The four fabricated samples were placed inside of a Styrofoam container for support in an array consisting of two samples on the bottom and two on the top, reminiscent of the 4-block simulation model. The Styrofoam container was located between the interrogating and receiving antennas with their surface perpendicular to the propagation direction of the incident wave. The arrangement for the testing can be observed in Figure 5.4.

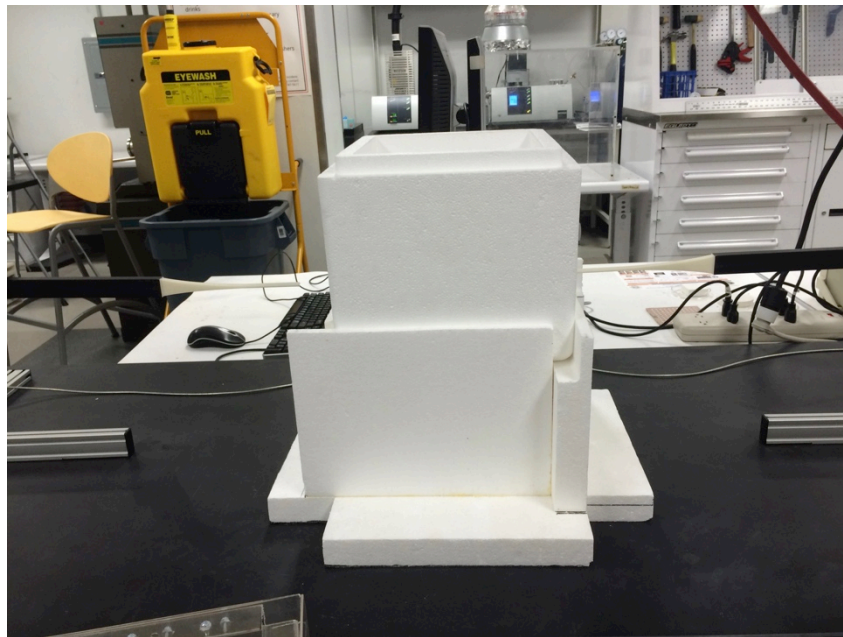


Figure 5.4. Free space testing setup consisting of Gaussian beam antennas and Styrofoam container for transmission measurements of metamaterial sensors.

The interrogation was performed for the $S_{2,1}$ parameter and the results were captured by the PNA. A single, prominent peak was observed in the transmission spectrum for the 14.47 GHz mark with an intensity of -33.05 dB. This could constitute resonance peak as a rapid change in trend is observed across the frequency domain. These results show some inconsistencies with the developed model in terms of the available peaks and overall trend. The differences in the results can be attributed to several factors. Among the most important ones is the inclusion of the polymeric material, which was not considered in the bulk dielectric constant calculations. This material has different properties when compared to ceramic materials and affects the effective bulk properties in the employed dielectric substrate. Additionally, fabrication errors such as CRR alignment both in the x and y directions as well as deviations in the horizontal placement of the washers on the dielectric, matrix which could result in a variation of the response and even decoupling between the CRRs. Moreover, the distribution of the BTO and BN could be uneven, resulting in variations of the dielectric constant when being encountered by the wave. Although several differences from the designed sensor were observed, a strong response was still found which could be associated with a resonance frequency. Similar peaks were observed in the simulation response around the 16 GHz in the simulation results, which could be associated with the response found experimentally. These peaks, if consistent, could be employed for temperature measurements. The transmission results for the metamaterial arrangement can be found in Figure 5.5.

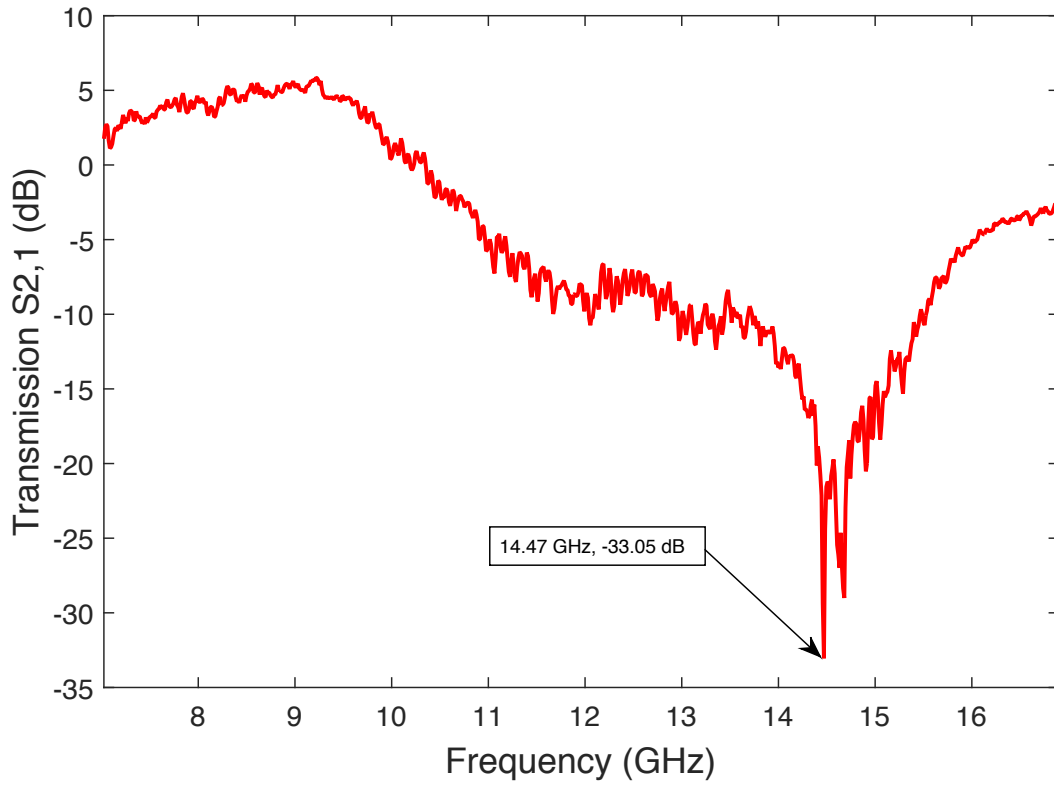


Figure 5.5. Transmission response for 4-block arrangement in the using Gaussian beam antennas

5.4 Conclusion

Free space measurements were performed for the guided mode resonance filter sensor and the metamaterial sensor. These measurements were carried out at the EM Laboratory and the cSETR - Challenger-Columbia Structures and Materials Research facility located at The University of Texas at El Paso. For the GMRF sensor, the tests were performed inside of an anechoic chamber in order to obtain better results. E-calibration was performed for these measurements. X-band horn antennas and reflection measurements were performed. The GMRF sensor displays no apparent resonance peak in the 8.2 – 12.4 GHz region. After further examination, a hypothesis was drawn regarding the errors from the fabrication adding up to a detrimental sensor performance. Warping was found to be significant on both the aluminum and steel samples. The warping of the top plate resulted in an air gap that prevents contact from the diffraction grating and the dielectric ceramic at random zones of the sensor. It was hypothesized

that this air gap was preventing the guided modes from interacting with the waveguide structure and, thus, traveling inside of it due to the possible lack of total guided modes, internal reflections and also a change of phase of the diffracted modes. For the metamaterial sensor, a similar a set of Gaussian beam antennas was employed. These samples were arranged on a 2x2 matrix and were tested for transmission spectrum. Although the results deviate from the ones found in the simulation section, a resonance peak was observed for the transmission spectrum in the 14.47 GHz mark with an intensity of -33.05 dB. The variation of these results can be attributed to several factors such as the inclusion of the polyvinyl alcohol binder, misalignment of the CRRs and uneven distribution of the mixed ceramics. If this peak is present in further testing, it could be used for temperature sensing applications in the future.

Chapter 6: Conclusions and Future Work

6.1 Conclusions

There has been an increasing need in recent years to develop next generation wireless, passive temperature sensors for harsh environment applications. Accurate, real time temperature monitoring can translate into better thermal efficiencies, less ambient pollution and better structural integrity. However, current sensor solutions are hindered by the harsh environment present in the different components of energy conversion systems. This research project provides the initial steps into the development of next generation passive, wireless temperature sensors using the principles of guided mode resonance filters and metamaterials.

For the proposed sensors a structured approach consisting on modeling and simulation, fabrication and free space measurement characterization was followed. For the modeling and simulation, a systematic approach was employed where the sensor was designed through a set of subsequent simulations dealing with unit cell dimensions, number of periods employed and full sensor performance. For the GMRF sensor, a tri-layered structure composed of two metallic screens with a sandwiched dielectric ceramic was proposed. Titanium was proposed for the simulation metal, however, titanium, steel and aluminum were explored in the fabrication steps for the metallic elements; alumina was employed as the dielectric ceramic. A design frequency of 10 GHz was assigned to the GMRF sensor for reflection. A unit cell with a side length of 9.705 mm, a total thickness of 2.54 mm and a circular aperture of 3.34 mm were achieved. This resulted in a resonance frequency of 10.065 GHz and an intensity of -16.8 dB. Further simulations explored the effect of the circular aperture and the dielectric constant of the ceramic were performed resulting in a frequency shift for both variables. A simulation studying the effect of the number of periods was also performed confirming that the response of the device improves as the number of periods approached infinity; however, this would lead to extremely large devices, therefore the addition of reflectors was studied. The addition of reflectors shifted the response of the frequency to closer values in intensity and frequency when compared to the

ideal value. Based on these simulations, a 5x5 period array sensor was designed with reflective walls on all sides. The sensor had final a side length of 49.525 mm and a thickness of 2.54 mm. The response of the finite sensor obtained from the simulation was of 10.19 GHz mark with an intensity of -15.89 dB. Sensor samples were fabricated using water jet cutting technologies for titanium screens and commercial alumina ceramic following the developed design. To resolve the size drawbacks of this fabrication, traditional machining methods using steel and aluminum plates were employed to create bigger samples. A sensor encasing and a diffraction grating were machined out of steel and aluminum plates and thin plates, respectively. These samples had a side length of 127 mm and a thickness of 7 mm. Samples were tested in an anechoic chamber and X-band horn antennas. Results were inconclusive as no peak was found in the sample. It is suspected that it was mainly due to an air gap resulting from the top plate warping as a result of the fabrication methods. A refinement of the fabrication methods should be explored in order to ensure the success of the sensor.

As for the metamaterial, a similar approach on the modeling and simulation was employed. A unit cell with a side length of 10.17 mm and a thickness of 3.175 mm was developed employing a combination of BTO and BN dielectric ceramics to achieve improved properties. Commercially available copper washers with an outer radius of 3.5 mm, an inner radius of 1.6 mm and a thickness of 0.05 mm served as the model for the CRRs. The model consisted of a dielectric block with embedded CRR structures. Simulations were performed for reflection and transmission spectra and several peaks were encountered. A 5 period simulation was performed and the results suffered in quality from the limited number of periods. However, the peaks on the reflection spectra were still present. The degradation of the response was attributed to the reduction of the number of periods from an infinitely periodic structure. Finite simulations were performed replicating possible fabrication samples and for an arrangement of four of such samples. Signal improvement was gradually attained through the addition of more CRRs into the periodic structure, resulting in visible peaks for the 4-block simulations. The most prominent peaks were of 13.23 GHz with an intensity of -12.2 dB for reflection and 16.08 GHz

mark with a depth of -28.89 dB for transmission. This metamaterial sensor model had a side length of 101.16 mm and a thickness of 3.175 mm. Fabrication for the metamaterial sample was performed using traditional powder compression methods. A mixture of 70% BN/30% BTO was used as the dielectric ceramic with the addition of 7.5% wt. of PVA to the mixture for enhanced rigidity. Commercially available copper washers were employed as CRR structures. 8.161 grams of BTO and 13.135 grams of BN were employed. The samples were fabricated using a square die with 50.8 mm in side length by compressing the powder/CRR structure with 3 metric tons of pressure for 5 minutes. The final dimensions of the metamaterial sensor units were of 50.8 mm for the side length and 3.175 mm for the thickness. Free space measurements for these samples were performed using a set of Gaussian beam antennas and a VNA. The samples were arranged in a 2x2 square matrix for the testing and transmission measurements were performed. This sample arrangement results in a resonance peak appearing in the spectra around the 14.47 GHz mark with an intensity of -33.05 dB. The difference in the simulation and experimental results can be attributed to several factors such as the effects of binder on the properties, misalignment of CRRs and uneven distribution of the components of the mixture. The demonstration of this resonant behavior of the metamaterial sensor could result in further testing to ensure repeatability and characterize the temperature sensitivity of the sensor.

Recommendations for future work are presented in the next section to address some of the challenges observed in the development of both of sensors as well as a discussion of what the next steps could be for the successful development of this project.

6.2 Recommendations for future work

6.2.1 Guided mode resonance filter sensor

The following recommendations are given for the guided mode resonance filter sensor:

- Characterization of the dielectric constant of the high purity alumina ceramic using waveguide methods in order to see the discrepancies between the simulated and the

experimental values. If variations exist, adjust the simulation to mirror the fabricated sample and simulate to locate the new resonance peak.

- Upgrade the fabrication methods to ensure the plates remain straight after machining. 3-D printing with Ti-64 could also be employed for the fabrication resulting in virtually perfect encasings for the alumina slab.
- Samples with bigger dimensions should also be explored if the testing method will continue to be based on X-band horn antennas. This is due to the diverging nature of the wave when exiting the antenna, which could result in diffracted waves on the edges of the sample.
- Study the angle sensitivity of the GMR sensor to characterize its field of view, which could affect the overall performance of the sensor and result in more robust sensing solutions.
- After the room temperature characterization is successful, employ a transparent high temperature furnace to heat the ambient around the device evenly and capture the temperature dependent response of the sensor.

6.2.2 Metamaterial sensor

Similarly, the following recommendations are given for metamaterial-based sensor:

- Characterization of the dielectric constant of the ceramic substrate can result in better agreement between the simulation results and the experimental data obtained.
- Due to the possible dependence of the response on the angle of incidence, the field of view of the sensor should be studied to assess its sensitivity to the direction of the incoming electromagnetic wave.
- After the performance of the sensor in room temperature has been fully characterized, high temperature free space measurements should be performed using a transparent temperature furnace to demonstrate the temperature sensitivity of the sensor.

References

- [1] Wang, Y., Yi, J., Quiushi, C., and Yang, Y. *A Passive Wireless Temperature Sensor for Harsh Environment Applications* Sensors, Vol. 8, 7982 – 7995, 2008.
- [2] Zhang, .Y., Pickrell, G. R., Qi, B., Saafi-Jazi, A., Wang, A. “Single-Crystal Sapphire-Based Optical High Temperature Sensor for Harsh Environment Applications” *Opt. Eng.*, no. 43(1). 2004: 157-164.
- [3] Zhao, R., Shao, G., Cao, Y., An, L., Xu, C. “Temperature Sensor Made of Polymer Derived Ceramics for High-Temperature Applications” *Sensors and Actuators: A Physical*, no. 219. 2014: 58-64.
- [4] Goetz, J., *Sensors That Can Take the Heat, Part 1: Opening the High-Temperature Toolbox*. Sensors, 2000. **17**(6): p. 20-39.
- [5] Gregory, O.J. and T. You, *Ceramic temperature sensors for harsh environments*. Sensors Journal, IEEE, 2005. **5**(5): p. 833-838.
- [6] Thai, T.T., et al. *A novel passive wireless ultrasensitive RF temperature transducer for remote sensing*. in *Microwave Symposium Digest (MTT), 2010 IEEE MTT-S International*. 2010. IEEE.
- [7] Munk, B. A., “Frequency Selective Surfaces Theory and Design”, Wiley, 2000
- [8] Bayatpur, F. “Metamateria-Inspired Frequency Selective Surfaces”. Ph.D. Thesis,
- [9] Barton, J. H. “Frequency Selective Surfaces for Extreme Applications”, Ph.D. thesis, 2014.
- [10] Costa, F., Monorchio, A. “A Frequency Selective Radome With Wideband Absorbing Properties”, *IEEE Transactions in Antennas and Propagation*, 2012, 60(60), 2740 – 2747
- [11] Nie, X. C., Gan, Y. B., Yuan, N., Wang, C. F., Li, L. W. “An Efficient Hybrid Method for Analysis of Slot Arrays Enclosed by a Large Radome” *Journal of Electromagnetic Waves and Applications*, 2012, 20(2), 249 – 264
- [12] Lin, B. Q., Li, F., Zheng, R. Q., Zen, Y. S. “Design and Simulation of a Miniature Thick-Screen Frequency Selective Surface Radome” *IEEE Antennas and Propagation Letters*, Vol 8, 2009, pp. 1065 – 1068
- [13] Tennant, A., Chambers, B. “Adaptive radar absorbing structure with PIN diode controlled active frequency selective surface” *Smart Mater. Struct.* 2004, 13, 122-125
- [14] Palmer, C., Loewen, E. “The Diffraction Grating Handbook” The Newport Corporation, 6th Edition, 2005
- [15] Gaylord, T. K., Moharam, G. “Analysis and applications of optical diffraction gratings” *Proceedings of IEEE*, 1985, 73(5): p. 894 – 937
- [16] Gregory, J. “Correspondence of Scientific Men of the Seventeenth Century” Oxford University Press, 1674(2), p. 251–555

- [17] Hopkinson, F., Rittenhouse, D. “An Optical Problem, Proposed by Mr. Hopkinson, and Solved by Mr. Rittenhouse” *Transactions of the American Philosophical Society*, Vol. 2, (1786), p. 201-206
- [18] Loewen E. G. “Diffraction Gratings for Spectroscopy” *Journal of Physics E: Scientific Instruments*, 12(3), 1970, p. 953-961
- [19] Rowland H. A. “Preliminary Notice of the Results Accomplished in the Manufacture and Theory of Gratings for Optical Purposes” *Manufacture of Gratings*, 64, 1882, p. 224-228
- [20] Shyam Singh “Diffraction Gratings: Aberrations and Applications” *Optics & Laser Technology*, 31, 1999, p. 195-218
- [21] Vengsarkar, A. M., Lemaire, P. J., Judkins, J. B., Bhatia, V., Erdogan, T., Sipe, J. E. “Long Period Fiber Gratings as Band Rejection Filters” *Applied Optics*, 14(1), 1996, p. 58 – 65
- [22] Veldkamp W. B. “Laser Beam Profile Shaping With Interlaced Binary Diffraction Gratings” *Journal of Lightwave Technology*, 21(17), 1982, p. 3209 – 3212
- [23] Pollack, G. L., Stump, D. R., “Electromagnetism” *Addison Wesley*, 2002
- [24] Ibanescu, M., Fink, Y., Fan, S., Thomas, E. L., Joannopoulos, J. D. “An All-Dielectric Coaxial Waveguide” *Science Reports*, Vol. 289, 2000
- [25] Lord, R. “On the Passage of Electric Waves Through Tubes”, *Philosophical Magazine*, Vol. 43, 1897, p. 125 – 132. Reprinted in *Collected Papers*, Cambridge University Press, Cambridge University, 1903
- [26] Packard, K. S., “The Origin of Waveguides*: A Case of Multiple Rediscovery”, *IEEE Transactions in Microwave Theory and Techniques*, Vol. MTT-32(9), 1984, p. 961 – 969
- [27] Pozar, D. M. “Microwave Engineering”, John Wiley and Sons Inc., 4th Edition, 2011, p. 96
- [28] Barret, R. M., “Microwave Printed Circuits – An Historical Perspective”, *IEEE Transactions in Microwave Theory and Techniques*, Vol MTT-32(9), 1894, pp. 983 – 990
- [28] Englemann, H. F., Grieg D. D. “Microstrip – A New Transmission Technique for the Kilomegacycle Range” *Proceedings of the IRE*, Vol. 40, 1952, pp. 1644 – 1650
- [29] Stern A. R., Babbitt, W. R. “Integrated Dielectric Waveguide Radar Front End Device” *U.S. Patent*, 4,424,517, 1984
- [30] Degnan, J. J. “The Waveguide Laser: A Review” *Appl. Phys.* Vol. 11, pp. 1 – 33, 1976
- [31] Barton, J. H., Rumpf, R. C., Smith, R. W., Kozikowski, C., Zellner, P. “All-Dielectric Frequency Selective Surfaces With Few Number of Periods”, *Progress in Electromagnetic Research B*, Vol. 41, p. 269 – 283, 2012
- [32] Magnusson, R., Wang, S.S. “New Principle for Optical Filters” *Applied Physics Letters*, Vol. 61, 1992, pp. 1022 – 1024
- [33] Lin, S. F., Wang, C.M., Tsai, Y. L., Ding, T. J., Yang, H. T., Chen, W. Y., Yeh, S. F., Chang, J. Y. “A Model for Fast Predicting and Optimizing the Sensitivity of Surface-Relief Guided Mode Resonance Sensors” *Sensors and Actuators B: Chemical*, Vol. 176, 2013, pp. 1197 – 1203

- [34] Thurman, S. T., Morris, G. M. “Controlling the Spectral Response in Guided-Mode Resonance Filter Design” *Applied Optics*, Vol. 42(16), 2003, pp. 3225 – 3233
- [35] Rosenblatt, D., Sharon A., Friesem, A. A. “Resonant Grating Waveguide Structures” *IEEE Journal of Quantum Electronics*, Vol. 33(11), 1997, pp. 2038 - 2059
- [37] Rayleigh, L. “On the Dynamical Theory of Gratings” *Proceedings of the Royal Society of London*, Vol. 79(532), 1907, pp. 399 – 416
- [38] Sentenac, A., Fehrembach, A.-L. “Angular Tolerant Resonant Gratings Filters Under Oblique Incidence” *J. Opt. Soc. Am.*, Vol. 22(3), 2005, pp. 475 – 480
- [39] Valentine, J., Zhang, S., Zentgraf, T., Ulin-Avila, E., Genov, D., Bartal, G., Zhang, X. “Three-Dimensional Optical Metamaterial with a Negative Refractive Index”, *Nature Letters*, Vol. 455(18), 2008, pp. 376 – 380
- [40] Grimberg, R. “Electromagnetic Metamaterials” *Material Science and Engineering B*, Vol. 178, 2013, pp. 1285 – 1295
- [41] Katsarakis, N., Koschny, T., Kafesaki, M., Economou, N., Soukoulis, C. M. “Electric Coupling to the Magnetic Resonance of Split Ring Resonators” *Applied Physics Letters*, Vol. 84(15), 2004, pp. 2943 – 2945
- [42] Landy, S. I., Sajuyibe, S., Mock, J. J., Smith, D. R., Padilla W. J. “Perfect Metamaterial Absorber”, *Physical Review Letters*, Vol. 100, 2008,
- [43] Freire, M. J., Marques, R., Jelinek, L. “Experimental demonstration of a $\epsilon = 1$ metamaterial lens for magnetic resonance imaging” *Applied Physics Letters*, Vol. 93, 2008
- [44] Smith, D. R., Pendry, J. B., Wiltshire, M. C. K. “Metamaterials and Negative Refractive Index” *Science*, Vol. 305, 2004, pp.
- [45] Veselago, V. “The Electrodynamics of Substances with Simultaneously Negative Values of ϵ and μ ” *Soviet Physics*, Vol. 10(4), 1968, pp. 509 – 514
- [46] Pendry, J. B., Holden, A. J., Stewart, W. J., Youngs, I. “Extremely Low Frequency Plasmons in Metallic Meso Structures” *Physics Review Letters*, Vol. 76, 1996, pp. 4773 – 4776
- [47] Pendry, J. B., Holden, Robbins, D. J., Stewart, W. J. “Magnetism from Conductors and Enhanced Nonlinear Phenomena” *IEEE Transactions on Microwave Theory and Techniques*, Vol. 47(11), 1999, pp. 2075 – 2084
- [49] Smith, D. R., Padilla, W. J., Vier, D. C., Nemat-Nasser, S. C., Schultz, S. “Composite Medium with Simultaneous Negative Permeability and Permittivity” *Physical Review Letters*, Vol. 84(18), 2000, pp.
- [49] Shelby, R. A., Smith, D. R., Schultz, S. “Experimental Verification of a Negative Index of Refraction” *Science*, Vol. 292, 2001, pp. 77 – 79
- [50] Pendry, J. B., Smith, D. R. “Reversing Light: Negative Refraction” *Physics Today*, Vol. 57, 2004, pp. 47 – 43
- [51] Pendry, J. B. “Negative Refraction Makes a Perfect Lens” *Physical Review Letters*, Vol. 85(18) 2000, pp. 3966 – 3969

- [52] Pendry, J. B., Schurig, D., Smith D. R. “Controlling Electromagnetic Fields” *Science*, Vol. 312, 2006, pp. 1780 – 1782
- [53] Cai, W., Chettar, U. K., Kildishev A. V., Shalaev, V. M. “Optical Cloaking with Metamaterials” *Nature Photonics*, Vol. 1, 2007, pp. 224 – 227
- [54] Schurig D., Mock, J. J., Justice, B. J., Cummer, S. A., Pendry, J. B., Starr, F. A., Smith D. R., “Metamaterial Electromagnetic Cloak at Microwave Frequencies” *Science*, Vol. 314, 2006, pp. 977 – 979
- [55] Hawkes, A. M., Katko, A. R., Cummer, S. A. “A Microwave Metamaterial with Integrated Power Harvesting Functionality” *Applied Physics Letters*, Vol. 103, 2013
- [56] Ekmekci, E., Sayan-Turan, G. “Metamaterial Sensor Application Based on Broadside-Coupled SRR and V-Shaped Resonator Structures” *Applied Physics Letters*, Vol. 103, 2013
- [57] Moharam, M. G., Gaylord, T. K. “Rigorous Coupled-Wave Analysis of Planar-Grating Diffraction” *J. Opt. Soc. Am.*, Vol. 71(7), 1981, pp. 811 – 818
- [58] Wang, S. S., Magnusson, R., Bagby, J. S. “Guided-mode Resonance in Planar Dielectric-Layer Diffraction Gratings” *J. Opt. Soc. Am. A*, Vol. 7(8), 1990, pp. 1470 – 1474
- [59] Wang, S. S., Magnusson, R. “Theory and Applications of Guided-mode Resonance Filters” *Applied Optics*, Vol. 32(14), 1993, pp. 2606 – 2613
- [60] Harms, P., Mittra, R., Ko, W. “Implementation of the Periodic Boundary Condition in the Finite-Difference Time-Domain for FSS Structures” *IEEE Transactions on Antennas and Propagation*, Vol. 42(9), 1994, pp. 1317 – 1324
- [61] Mizutani A., Kikuta, H., Iwata, K. “Wave Localization of Doubly Periodic Guided-mode Resonance Gratings” *Optical Review*, Vol. 10(1), 2003, pp. 13 – 18
- [62] Wang, S. S., Magnussonm R. “Multilayer Waveguide-Grating Filters” *Applied Optics*, Vol. 34(14), 1995, pp. 2414 – 2420
- [63] Tibuleac, S., Magnusson, R. “Reflection and Transmission Guided Mode Resonance Filters” *J. Opt. Soc. Am. A*, Vol. 14(7), 1997, pp. 1617 – 1626
- [64] Rosenblantt, D., Sharon, A., Friesem, A. “Resonant Grating Waveguide Structures” *IEEE Journal of Quantum Electronics*, Vol. 33(11), 1997, pp. 2038 – 2059
- [65] Wang, Q., Zhang, D., Huang, Y., Ni, Z., Zhuang, S. “Tunable Intensity of the Spectral Reflectance of a Guided Mode Resonance Filter with Dual Channels” *Optics & Laser Technologies*, Vol. 43, 2011, pp. 1091 – 1095
- [66] Sang, T., Zhao, H., Cai, S., Wang, Z. “Design of Guided-Mode Resonance Filters with an Antireflective Surface at Oblique Incidence” *Optics Communications*, Vol. 285, 2012, pp. 258 – 263
- [67] Barton, J. H., Garcia, C. R., Berry, E. A., May, G. R., Gray, D. T., Rumpf, R. C. “All-Dielectric Frequency Selective Surface for High Power Microwaves” *Progress in Electromagnetic Research B*, Vol. 41, 2012, pp. 269 – 283

- [68] Barton, J. H., Garcia, C. R., Berry, E. A., May, G. R., Gray, D. T., Rumpf, R. C. “All-Dielectric Frequency Selective Surface for High Power Microwaves” *IEEE Transactions on Antennas and Propagation*, Vol. 62(7), 2014, pp. 3652 – 3656
- [69] Van Labeke, D., Gerard, D., Guizal, B., Baida, F. I., Lifeng, L. “An Angle-Independent Frequency Selective Surface in the Optical Range ” *Optics Express*, Vol. 14(25), 2006, pp. 11945 – 11951
- [70] Kaja, S., Hilgenberg, J. D., Collins, J. L., Shaha, A. A., Wawro, D., Zimmerman, S., Magnusson, R., Koulou, P. “Detection of Novel Biomarkers for Ovarian Cancer with an Optical Nanotechnology Detection System Enabling Label-Free Diagnostics” *Journal of Biomedical Optics*, Vol. 17(8), 2006
- [71] Jia, K., Zhang D., Ma, J. “Sensitivity of Guided Mode Resonance Filter-Based Biosensor in Visible and Near Infrared Ranges” *Sensors and Actuators B*, Vol. 156, 2011, pp. 194 – 197
- [72] Smith, D. R., Schultz, S., Markos, P., Soukoulis, C. M. “Determination of Effective Permittivity and Permeability of Metamaterials from Reflection and Transmission Coefficients” *Physical Review B*, Vol. 65, 2002
- [73] Smith, D. R., Vier, D. C., Kroll, N., Schultz, S. “Direct Calculation of Permeability and Permittivity for a Left-Handed Metamaterials” *Applied Physics Letters*, Vol. 77, 2000
- [74] Simovksy, C. R. “Material Parameters of Metamaterials” *Optics and Spectroscopy*, Vol. 107(5), 2009, pp. 763 – 799
- [75] Bilotti, F., Toscano, A., Vegni, L., Aydin, K., Boratay, A., Ozbay, E. “Material Parameters of Metamaterials” *Optics and Spectroscopy*, Vol. 107(5), 2009, pp. 763 – 799
- [76] Baena, J. D., Bonache, J., Martin, F., Sillero, R. M., Falcone, F., Lopetegui, T., Laso, M. G. M., Garcia-Garcia, J., Gil, I., Flores Portillo, M., Sorolla, M. “Equivalent-Circuit Models for Split Ring Resonators and Complementary Split Ring Resonators Coupled to Planar Transmission Lines” *IEEE Transactions on Microwave Theory and Techniques*, Vol. 53(4), 2005, pp. 1451 – 1461
- [77] Page, J. E., Esteban, J., Camacho-Peñalosa, C. “Microwave Circuit Theory-based Model to Predict the Resonant Frequencies of a Wide Range of Ring Resonators” *Int. J. Electron. Commun.*, Vol. 63, 2009, pp. 327 – 337
- [78] Wood, B. “Metamaterials and Invisibility” *C. R. Physique*, Vol. 10, 2009, pp. 379 – 390
- [79] Lippens, D. “Metamaterials and Infra-red Applications” *C. R. Physique*, Vol. 9, 2009, pp. 184 – 196
- [80] Marquez, R., Mesa, F., Martel, J., Medina, F. “Comparative Analysis of Edge- and Broadside- Coupled Split Ring Resonators for Metamaterial Design – Theory and Experiments” *IEEE Transactions on Antennas and Propagation*, Vol. 51(10), 2003, pp. 2572 – 2581
- [81] Chen, J.-Y., Chen, W.-L., Yeh, J.-Y., Chen L.-W., Wang, C.-C. “Comparative Analysis of Split Ring Resonators for Tunable Negative Permeability Metamaterials Based on Anisotropic Dielectric Substrates” *Progress in Electromagnetic Research M*, Vol. 10, 2009, pp. 25 – 38

- [82] Karim, H., Delfin, D., Shuvo, M. A. I., Chavez, L. A., Garcia, C. R., Barton, J. H., Gaytan, S. M., Cadena, M. A., Rumpf, R.C., Wicker, R. B., Lin, Y., Choudhuri, A. “Concept and Model of a Metmaterial-Based Passive Wireless Temperature Sensors for Harsh Environment Applications” *IEEE Sensors Journal*, Vol. 15(3), 2015, pp. 1445 – 1452
- [83] Silva, A., Francesco, M., Castaldi, G., Galdi, V., Alu, A., Engheta, N. “Performing Mathematical Operations with Metamaterials” *IEEE Sensors Journal*, Vol. 15(3), 2015, pp. 1445 – 1452
- [84] Kundtz, N., Smith, D. R. “Extreme-Angle Broadband Metamaterials Lens”, *Nature Materials*, Vol. 9, 2010, pp. 129 – 132
- [85] Ekmekci, E. “Design, Fabrication and Characterization of Novel Metamaterials in Microwave and Terahertz Regions: Multi-band Frequency Selective and Miniaturized Structures”, *Ph.D. thesis*, 2010
- [86] Karim, H. “Development of ‘Lick and Stick’ Passive, Wireless Temperature Sensors for Harsh Environment”, *Master’s thesis*, 2014
- [87] Kabashin, A. V., Evans P., Pastkovsky, S., Hendren, W., Wurtz, G. A., Atkinson, R., Pollard, R., Podolsky, V. A., Zayats, A. V. “Plasmonic Nanorod Metamaterials for Biosensing”, *Nature Materials*, 2009, pp. 867 – 871
- [88] Schimetta, G., Dollinger, F., Scholl, G., Weigel, R. “Wireless Pressure and Temperature Measurement Using a SAW Hybrid Sensor”, *IEEE Ultrasonic Symposium*, 2000, pp. 445 – 448
- [89] Ballandras, S., Daniau, W., Berthelot, M. P. “Wireless Temperature Sensor Using SAW Resonators for Immersed and Biological Applications”, *IEEE Ultrasonic Symposium*, 2002, pp. 445 – 448
- [90] Hornsteiner, J., Born, E., Fischerauer, G., Riha, E. “Surface Acoustic Wave Sensors for High-Temperature Applications”, *IEEE International Frequency Control Symposium*, 1998, pp. 615 – 620
- [91] Opasjumruskit, K., Thantipwan, T., Sathusen, G., Pootarapan E., Wongkomet, N., Tanachayanont, A., Thamsirianunt, M. “Self-Powered Wireless Temperature Sensors Exploit RFID Technology”, *RFID Technology (Published by IEEE C and IEEE ComSoc)*, 2006
- [92] Girbau, D., Ramos, A., Lazaro, A., Rima, S., Villarino, R. “Passive Wireless Temperature Sensor Based on Time-Coded UWB Chipless RFID Tags”, *IEEE Transactions on Microwave Theory and Techniques*, Vol. 60(12), 2012, pp. 3623 – 3632
- [93] Ong, K. G., Grimes, C. A., Robbins, C. L., Singh, R. S. “Design and Applications of a Wireless, Passive, Resonant Circuit Environmental Monitoring Sensor”, *Sensors and Actuators A*, Vol. 93, 2001, pp. 33 – 43
- [94] Thai, T. T., Mehdi, J. M., Aubert, H., Pons, P., DeJean, G. R., Tentzeris, M. M., Plana, R. “A Novel Passive Wireless Ultrasensitive RF Temperature Transducer for Remote Sensing”, *IEE IMS*, 2010, pp. 473 – 476

- [95] Zhang, Y., Pickrell, G. R., Qi, B., Safaai-Jazi, A., Wang, A. "Single-Crystal Sapphire-Based Optical High-Temperature Sensor for Harsh Environments", *Optical Engineering*, Vol. 43(1), 2004, pp. 157 – 164
- [96] Cheng, H., Ebadi, S., Ren, X., Gong, X. "Wireless Passive High-Temperature Sensor Based on Multifunctional Reflective Patch Antenna up to 1050 Degrees Centigrade ", *Sensors and Actuators A*, Vol. 222, 2015, pp. 204 – 211
- [97] Ekmkeci, E., Turhan-Sayan, "Multi-Functional Metamaterial Sensor on a Broad-Side Coupled SRR Topology with a Multi-Layer Structure", *Applied Physics A*, Vol. 110, 2013, pp. 187 – 197
- [98] Wilson, W. C., Atksinon, G. M. "Wireless Sensor Applications for NASA's Extreme Aeronautical Environments ", *IEEE Sensors*, Vol. 14(11), 2014, pp. 3745 – 3753
- [99] Auerkari, P. "Mechanical and Physical Properties of Engineering Alumina Ceramics", *VTT Manufacturing Technology*, 1996
- [100] Kinoshita, K., Yamaji, A. "Grain-Size Effects on Dielectric Properties in Barium Titanate Ceramics" *Journal of Applied Physics*, Vol. 47(1), 1976, p. 371-373.
- [101] McNeal, M.P., S.-J. Jang, Newnham, R.E. "The Effect of Grain and Particle Size on the Microwave Properties of Barium Titanate (BaTiO₃)" *Journal of Applied Physics*, Vol. 83(6), 1998, pp. 3288-3297.
- [102] Pant, H. C., Patra, M. K., Verma, A., Vadera, S. R., Kumar, N. "Study of the Dielectric Properties of Barium Titanate–Polymer Composites" *Acta materialia*, Vol. 54(12), 2006, pp. 3163-3169.
- [103] Varadan, V. V., Hollinger, R. D., Ghodgaonkar, D. K., Varadan, V. K. "Free-Space, Broadband Measurements of High-Temperature, Complex Dielectric Properties at Microwave Frequencies" *IEEE Transactions on Instrumentation and Measurements*, Vol. 40(5), 1991 pp. 842-846.
- [104] Bruggeman, D. "Dielectric Constant and Conductivity of Mixtures of Isotropic Materials" *Ann Phys (Leipzig)*, 24,1935, pp. 636-679.
- [105] Niklasson, G.A., Granqvist, C., Hunderi, O. "Effective Medium Models for the Optical Properties of Inhomogeneous Materials" *Applied Optics*, Vol. 20(1), 1981, pp. 26-30.

Appendix A: GMRF finite sensor simulation with cladding layer separation

After the preliminary tests for the GMRF sensors were performed with in the X-band region with no visible resonant peak for either of the samples, it was hypothesized that the fabrications errors had an important detrimental effect on the performance of the sensor. Poor contact between the metallic grating and the dielectric ceramic was considered to be among the most prominent contributors to the poor performance of the sensor. To confirm this, a finite sensor simulation with an air gap was performed using HFSS. The finite sensor model was taken and the top plate was moved upward to leave a distance of 0.18 mm between the layers. The sidewall reflectors were also modified to account for this change in height. The same excitation (wave ports) and boundary conditions (PMLs) as for the finite sensor model were employed for the simulations. A discrete simulation was run with a step size of 0.005 for a frequency range of 8 to 12 GHz. The model is portrayed in the Figure below.

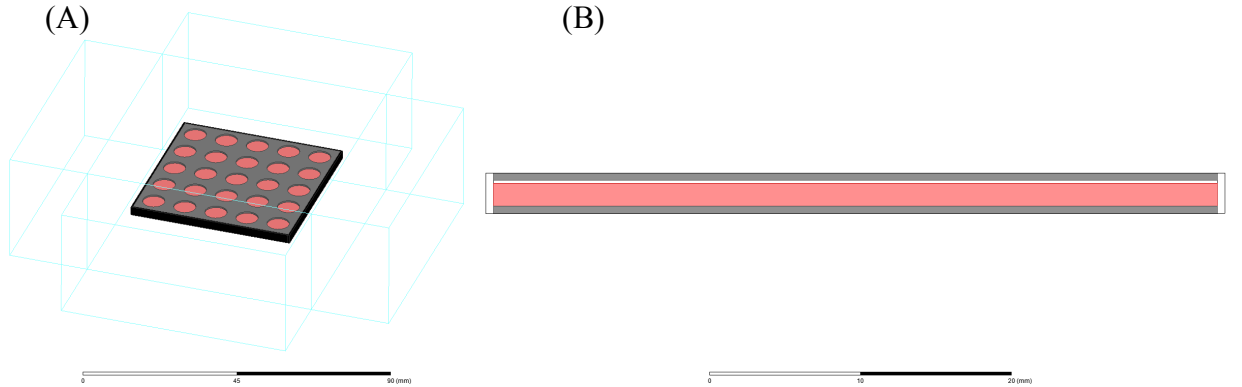


Figure A.1. (A) Trimetric view of finite sensor model with air-gap, (B) side view portraying the air-gap

After the simulation was performed, the results suggested a decay in the interaction of the sensor with the incident wave. The results can be observed in Figure A.2.

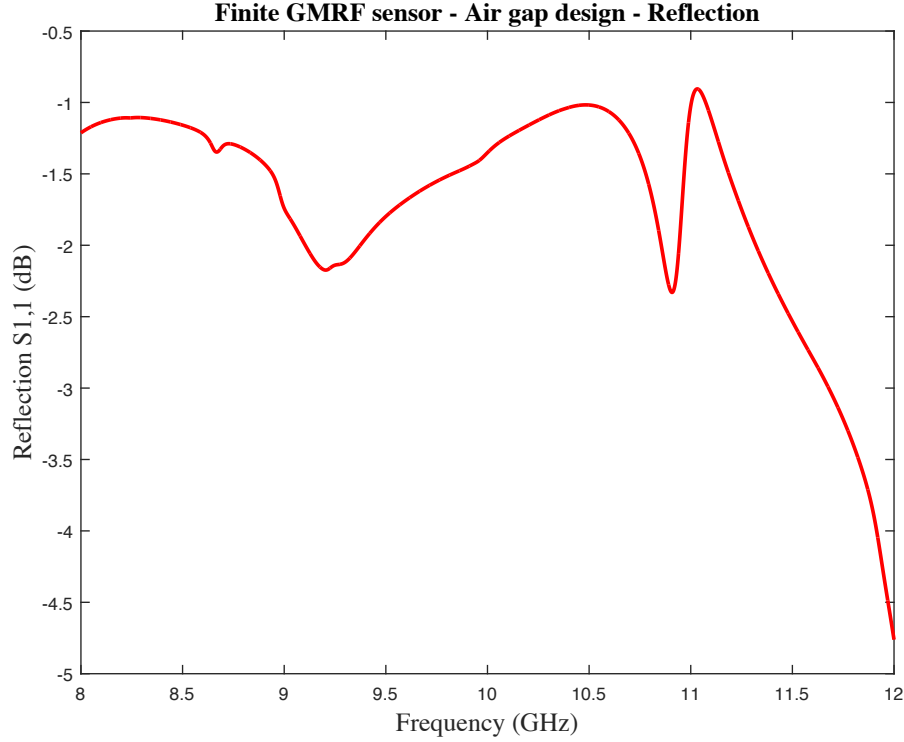


Figure A.2. Reflection spectra of finite model with the included air gap

As observed in the results, the peak that was previously present around the 10 GHz mark has disappeared. The air gap present between the dielectric layer and the metallic grating can be considered to be the sole contributor to this change in behavior. The disappearance of the peak due to the air gap present between the layers could be due to the a rapid change in the refractive index coefficient after the discretization of the wave, which could alter the entering phase of the spatial harmonics to the waveguide structure as well as the conditions for total internal reflections. This results in no guided mode inside of the device and the existence of only evanescent fields. Thus, no resonant behavior is present in the device. The insights provided by this simulation can result in better sensor design to ensure that the response will be present when performing the free space measurements.

Vita

Diego I. Delfin Manriquez was born on June 17th, 1991 in Ciudad Juarez, Chihuahua, Mexico. Mr. Delfin completed a Bachelor's of Science in Mechanical Engineering in December 2013 from The University of Texas at El Paso. During his undergraduate years, Mr. Delfin worked in the Functional Energy Materials Systems (FEMS) Laboratory under Dr. Yirong's Lin supervision in projects related to lead free energy storage nanocomposites and wireless sensors. Mr. Delfin continued his graduate studies at The University of Texas at El Paso by pursuing a Master's Degree in Mechanical Engineering. He continued to work in FEMS Laboratory focusing his efforts on the development of wireless temperature sensors using guided mode resonance filters and metamaterials. His research endeavors have resulted in Mr. Delfin co-authoring 6 journal papers and 8 conference papers to date.

Permanent address: Avandaro 6632, Colonia Santa Teresa
Ciudad Juarez, Chihuahua, Mexico, 32605

This thesis was typed by Diego I. Delfin Manriquez